ABSTRACT

CHARLES W. KINSEY. Dosimetry of Custom Inserts for Electron Beams Produced by a Varian Clinac 1800: Effect on Dose Output and Mean Incident Energy.

Customizing of electron beam treatment dimensions is a common clinical technique. The degree in which the measured energy and dose output for a particular beam varies depends on the degree of blocking and the nominal energy of that beam. Published measurements for the Varian Clinac 1800 are sparse and measurements for each custom insert manufactured are time consuming.

Relative output and mean incident energy measurements were performed for 180 nominal beam energy / cone / insert combinations on a Varian 1800 at the Rock Hill Radiation Therapy Center in Rock Hill, South Carolina.

Relative output measurements of the manufacturer supplied cones indicated no consistency in the data for all nominal beam energies. For example, the variation in relative output for increasing treatment field dimensions for the 6 MeV beam is different than for the 20 MeV beam. For custom square inserts within each cone, however, the data presented consistent behavior for all beams. The "square root" model for approximating relative output worked well with the custom square inserts and rectangular inserts with a relatively low length to width ratio. For rectangular

inserts with a high length to width ratio, the model exhibited a positive bias for all nominal beam energies and cones. It is theorized this bias may be due to the need to extrapolate the measured data for very small dimensions. By using some alternative measurement technique for these smaller dimensions, the bias may be reduced to an acceptable level.

The resulting energy measurements using the manufacturer supplied cones and inserts were mimicked by the use of custom inserts defining the same square dimensions for each cone. These data showed no effect of the inserts / cones on mean incident energy for the 6 MeV, 9 MeV, and 12 MeV nominal beam energies. An effect on mean incident energy for the 16 MeV and 20 MeV beams was noted only for the cases of the 4x4 and 6x6 inserts and for cases of rectangular inserts with a high length to width ratio. The "square root" model for approximating mean incident energy appeared to be a valid predictive tool for these measurements.

CONTENTS

LIST OF TABLES

LIST OF FIGURES

Figure

1.0 INTRODUCTION

1.1 Clinical Use of Electron Beams

Microwave-powered electron linear accelerators have become a popular tool for the treatment of cancer in the practice of radiation therapy. One class of these accelerators, known as high energy medical linacs, can deliver x-ray beam(s) of either single or dual energy and electron beams of multiple energies over a relatively broad surface area.

Electron beams with their high surface dose delivery and characteristically sharp dose fall-off with depth are ideal for the treatment of relatively superficial tumors such as skin lesions, cancers of the head and neck area, and postoperative breasts and chestwalls.(10) It has been estimated that electron beam therapy is indicated as either the primary mode or as an adjunct to x-ray treatment for approximately 10% of the patients treated in a radiation therapy clinic.(10)

1.2 Varian Clinac 1800 Electron Beam Production

One model of linear accelerator that generates dual x-ray energies and five electron energies and is the subject of this study is a Clinac 1800 manufactured by Varian Asso-

ciates. Briefly, this accelerator produces a clinically acceptable electron beam by the following (see Figure 1):

First, a stream of electrons is introduced by an "electron gun" into a klystron powered accelerator guide which will generate a current of an average specified energy.

Second, this current enters a bending magnet which produces a coarse steering of the electron current and behaves as a discreet energy window for the electrons.

Third, the steering of the electron current exiting the bending magnet is more finely adjusted by electromagnetic steering coils so the electrons will impinge onto a scattering foil. The interaction of the electron current with the scattering foil generates a broad electron beam.

Fourth, this broad beam is first collimated or shaped by interleaved x-ray collimators. Secondary collimation is then performed by an attachment made of a fiberglass frame with aluminum baffles at varying distances from the source and a steel insert located at the exit end of the attachment. This insert defines the actual dimensions of the electron beam produced for clinical use.

The manufacturer supplies a group of these attachments, called applicators or cones. Each cone in combination with its insert defines a predetermined square field dimension.

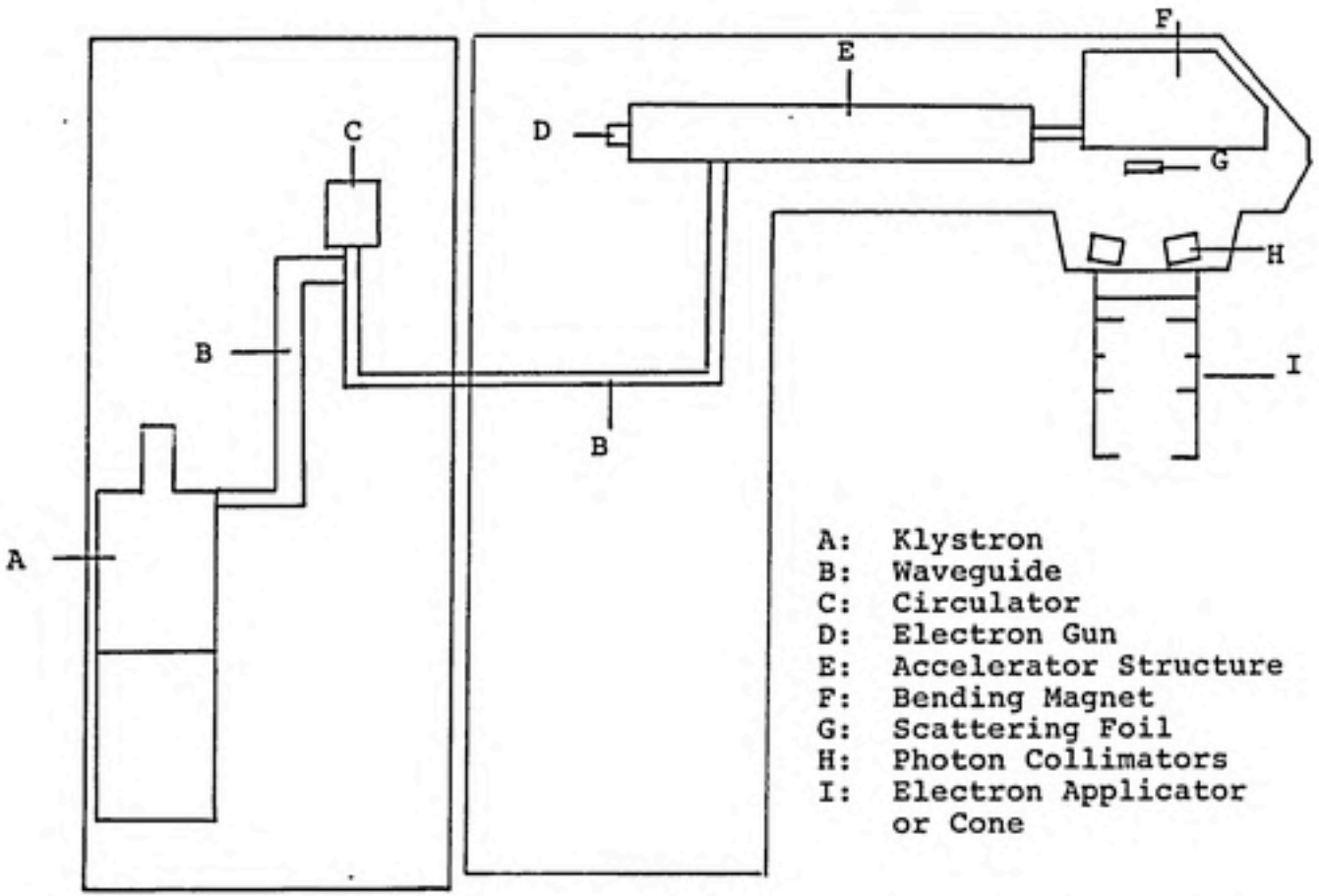

Figure 1. Varian Clinac 1800: A simplified schematic diagram indicating the major components discussed in the text.

1.3 Custom Shaping of the Electron Beam

One difficulty with attempting clinical use with only these square dimension inserts is that cancerous tumors very rarely are shaped as squares. A mechanism is available for the user to manufacture custom shaped inserts using a high-Z metal alloy and attach them to the supplied cones to customize the treatment field to the individual's case. This allows the clinician greater flexibility in sparing non-cancerous regions on / in the patient.

A possible uncertainty in treatment is introduced by using these custom inserts. The placing of a custom shaped slab of high-Z material into the electron beam's path to modify the treatment field dimensions may measurably affect, within the effective treatment field, the characteristics used as criteria for clinically acceptable use. The possible modification of beam characteristics by the use of custom inserts is the subject of this study.

1.4 Beam Characterictics Definitions

Two of the characteristics used to indicate the acceptable clinical use of an electron beam are a measured absorbed dose delivered or dose output and a measured mean incident energy.

1.4.1 Dose Output and Relative Output

Dose output is defined as the absorbed dose (usually in units of gray (Gy) or centigray (cGy)) delivered at a depth of maximum dose build-up (D_{max}) within a measurement phantom. In practice, this measurement is taken at the central axis of the beam with a National Bureau of Standards (NBS) traceable calibrated ionization chamber and electrometer combination. The collected ionization data is then converted to absorbed dose by the application of an accepted calibration protocol. For this study, the AAPM TG-21 (American Association of Physicist in Medicine Task Group 21) calibration protocol is used.(11) With this protocol the ionization readings, corrected for atmospheric conditions, are converted to absorbed dose in the phantom material or medium by the expression

$$D_{med} = M \times N_{gas} \times (\overline{L}/\rho)^{med}_{air} \times P_{ion} \times P_{repl} \qquad (1)$$

where D_{med} = the absorbed dose at D_{max} in the phantom medium,
M = the ionization reading,
N_{gas} = the ion chamber's calibration factor,
$(\overline{L}/\rho)_{air}^{med}$ = the restricted stopping power ratio,
P_{ion} = the chamber ionization recombination correction factor,
and P_{repl} = the chamber replacement (electron fluence) correction factor.(11)

If the phantom material is water, as is true in the present study, $D_{med} = D_{water}$. If the phantom is not water, then the expression

$$D_{water} = D_{med} \times (\overline{S}/\rho)^{water}_{med} \times \phi^{water}_{med} \qquad (2)$$

where D_{water} = the absorbed dose at D_{max} in water,
D_{med} = equation 1,
$(\bar{S}/p)_{med}^{water}$ = the unrestricted stopping power ratio,
and O_{med}^{water} = the electron fluence phantom correction factor

is needed.(11)

Parallel plate ionization chambers in the accelerator are used to continuously monitor the generated radiation. The units of measurement for these chambers are designated monitor units (MU). During accelerator calibration, the electronics for these chambers are adjusted such that for a designated defined field size (in this case 10 cm x 10 cm dimensions) a dose output of 1.00 cGy/MU is measured in a phantom at D_{max}. For other field sizes or cones, the dose output must be measured and is reported relative to the designated field size. These dose outputs are called relative outputs. TG-21 protocol does not specifically address how these relative outputs should be measured which has resulted in two basic techniques as to how these measurements are performed. One technique is that for each field size the ionization measurements are performed at the depth of maximum dose (i.e. D_{max}) and the dose outputs are calculated using equations 1 and 2. The other is to take ionization measurements at the depth of maximum ionization for each field size and calculate ratios to the ionization measurements obtained at the depth of maximum ionization for the 1.00 cGy/MU designated field size discussed previously. For this study, the measurement at maximum ionization depth and the calculation of ratios technique is used.

1.4.2 Mean Incident Energy

We have been using terms such as D_{max} without precisely defining how it is found. D_{max} is found by initially acquiring an ionization intensity versus depth below surface data set. This involves placing the probe at various depths along the central axis of the beam and collecting ionization data at each depth. These ionization data are then converted to absorbed dose by the use of equations 1 and 2. The resulting data set is called a percent depth dose (%DD) curve. The depth at which the maximum absorbed dose occurs is designated D_{max}. There is also a depth at which maximum ionization is measured. This depth is labeled R_{100}. It should be noted by the reader that R_{100} may or may not be equal to D_{max}.

The depth at which the ionization intensity is reduced to one-half of the maximum value is labeled R_{50}. The TG-21 protocol uses this value, when expressed in centimeters, to calculate the mean incident energy ($\bar{E}_o$) by the expression. (11)

$$\bar{E}_o = 2.33 \frac{MeV}{cm} \times R_{50}. \qquad (3)$$

This mean incident energy value is used to acquire from tables supplied with the protocol the restricted stopping power ratios used in equation 1 and the unrestricted stopping ratios and the electron fluence correction values used in equation 2.

The constant 2.33 MeV/cm for equation 3 was obtained by assumming plane-parallel, infinitely wide monoenergetic electrons incident upon a semi-infinite water phantom.(11) Some commercial software packages include table look-up values for this "constant" that is dependent upon the field size of the beam. Using this table look-up method, two electron beams of different field sizes with the exact same R_{50} value could have different $\bar{E}_o$ values. Since both calculation techniques (i.e. 2.33 MeV/cm for all beams vs. a seperate constant for each field size) are currently being used by the medical physics community, it is felt that reporting $\bar{E}_o$ values for each beam / insert combination in this study could be a source of confusion that could either mask or accentuate the effect of the insert. Therefore, the R_{50} value in units of centimeters for a specified nominal beam energy with its selected insert will be used as the energy measurement criteria for this study.

The term nominal beam energy will be used to identify each beam by the labeled beam energy specified by the manufacturer. An example of this would be that for the beam with a nominal beam energy of 6 MeV (i.e. labeled by the manufacturer) the mean incident energy is 4.9 MeV (i.e. calculated by equation 3).

1.5 Study Criteria Limits

One way of assuring clinically acceptable treatment

with a custom insert is to measure the mean incident energy and relative output of the specified beam in a phantom with the custom insert in place. This is a time consuming process and is difficult to schedule in a busy clinic before patient treatment is started. The ability to predict both when and by how much a custom insert affects a beam's relative output and mean incident energy prospectively would be of use clinically in the realm of increased quality of patient care and increased task scheduling efficiency of dosimetry personnel.

1.5.1 Relative Output

It has been estimated that the uncertainty inherent in measuring electron beam dose output is approximately one percent.(6) A criterion previously used as to a clinically acceptable predictive model for dose output relative to actual measurements is that predicted value should be within one percent of actual measured value.(7) This amount of accepted uncertainty falls well within the recommended upper limit of uncertainty for total dose delivery to a target volume, which is usually taken at five percent.(4) For acceptable model prediction of relative outputs compared to measured data, we will use a criterion of one percent variation.

1.5.2 Mean Incident Energy (R_{so})

The uncertainty in energy measurements by using the R_{so} value is dependent on the type and dimensions of the measurement probe and the precision of measurement probe placement within the phantom. This will be discussed in section 3.0.

For this study, the variation limit for acceptable model prediction will be set by one of two options. One, the limit will be set to equal the estimated uncertainty of R_{so} measurement. Two, the limit will be set to equal the difference in depth between the measured R_{so} value and either the measured R_{50} (i.e. 55% of maximum ionization depth) or the measured R_{45} (i.e. 45% of maximum ionization depth) values for that specific nominal beam energy. The choice of which variation limit is applicable will be based upon which criterion is the least restrictive.

1.6 Study Objectives

The purpose of this paper is two-fold. First, measurements of relative output and mean incident energy (R_{so}) for custom inserts that define varying treatment field dimensions will be presented to add to the relatively sparse database for this type of information pertaining to high energy Varian accelerators. Second, the possible application and testing of a previously developed predictive model (8)

that estimates both the effect on dose output and mean incident energy for non-standard rectangular fields will also be presented.

2.0 MODEL DEVELOPMENT

2.1 AECL Therac 20 Electron Beam Production

A model was presented by Mills, et al. (8) to predict the dose output for rectangular shaped electron beam fields for a Therac 20 Saturne accelerator manufactured by Atomic Energy of Canada Limited (AECL). For this accelerator, the beam of electrons exiting the accelerator structure is spread into a broad beam with a scanning quadrapole magnet. The collimation system is composed of primary interleaved photon collimators and secondary collimators, called trimmers. These trimmers are physically attached to the primary collimators, therefore both sets open and close in synchronization. The primary collimators define a field dimension 5 cm greater than the trimmers at 100 cm from the source.(8)

2.2 Relative Output Model

For model development, the electron beam is assumed to be made up of a collection of pencil beams. By using the theory of multiple coulomb scattering for electrons, an expression was developed (8) that describes the spreading of these pencil beams from the scattering in air which begins at the location of primary collimators. Assuming no energy shift in the electron beam and ignoring the scatter off the

secondary collimators, the following expression was developed that predicts the dose output for a rectangular shaped field. This expression which came to be called the "square-root model" is

$$O^{X,Y} = \sqrt{O^{X,X} \times O^{Y,Y}} \quad (4)$$

where $O^{X,Y}$ = the dose output of a rectangular field of X,Y dimensions,
$O^{X,X}$ = the dose output of a square field with side dimension X,
and $O^{Y,Y}$ = the dose output of a square field with side dimension Y.(8)

Appendix A is a reproduction of the original article which contains this equation's derivation (equation number 15). This expression will be used as the predictive model to estimate relative outputs for non-standard rectangular inserts.

2.3 Mean Incident Energy (R_{50}) Model

The same group of researchers presented an expression to predict the beam energy in the form of percent depth dose (%DD) for rectangular shaped fields.(3) This expression has the same mathematical form as equation 4 and is given by

$$DD^{X,Y} = \sqrt{DD^{X,X} \times DD^{Y,Y}} \quad (5)$$

where $DD^{X,Y}$ = the %DD of a rectangular field of X,Y dimensions,
$DD^{X,X}$ = the %DD of a square field with side dimension X,
and $DD^{Y,Y}$ = the %DD of a square field with side dimension Y.(3)

Appendix B is a reproduction of the original article which

contains this equation's derivation (equation number 17). This expression will be used as the predictive model to estimate R_{so} for non-standard rectangular inserts.

2.3 AECL Therac 20 and Varian Clinac 1800 Comparison

A possible difficulty with applying the previously presented expressions to a Varian Clinac 1800 electron beam is that its mechanism for the production of a broad electron beam is different from the AECL Therac-20 Saturne for which the model was developed. Table 1 compares some of differences between the two accelerators. Even with these differences noted, the present report focuses on the application of these models to our data.

FUNCTION	THERAC 20	CLINAC 1800
Initial Beam Broadening	Scanning quadra-pole magnet spreads the beam along the treatment field.	Thin sheet of tungsten used as a scattering foil.
Variation of Treatment Field Dimensions		
a) Primary Collimators	Varies with the actual treatment field.	Preprogrammed setting dependent upon cone/energy combination. Independent of field defining insert.
b) Secondary Collimators	Defines actual treatment field dimensions 5.0 cm less than the primary collimator setting.	Custom manufactured by user to needed field dimensions.

TABLE 1. Comparison of mechanisms for generation of broad electron beams between the AECL Therac 20 and the Varian Clinac 1800.

3.0 MEASUREMENT METHODS

3.1 Study and Measurement Equipment

The accelerator to which these measurements apply is a Varian Associates' Clinac 1800 located at the Rock Hill Radiation Therapy Center located in Rock Hill, South Carolina. This accelerator produces five electron beams with nominal beam energies of 6, 9, 12, 16, and 20 MeV. Table 2 summarizes the field defining applicators or cones supplied by the manufacturer with the nominal primary collimator opening dimensions for each cone / energy combination.

A family of field shaping metal alloy inserts of square and rectangular shape were made for each cone. The dimensions of the square inserts were chosen so that some would mimic the defined field made by a smaller cone dimension. One rectangular (i.e. length to width ratio greater than one) insert with a small length to width ratio has side dimensions that are bounded by the dimensions of the group of custom square inserts for each specified cone. Another rectangular insert with a large length to width ratio has side dimensions that are larger and smaller respectively than the dimensions of the group of custom square inserts for each specified cone. Table 3 summarizes the actual field defining inserts made for each cone.

For data acquisition, a beam scanner system manufac-

APPLICATOR SIZE	COLLIMATOR SETTING	
	6 AND 9 MeV	12, 16, and 20 MeV
4x4"	20x20	11x11
6x6"	20x20	11x11
10x10	20x20	14x14
15x15	20x20	19x19
20x20	25x25	25x25
25x25	30x30	30x30

" Both inserts used with 6x6 cone.

TABLE 2. Applicator / cone sizes with inserts supplied by Varian. All values are in units of centimeters.(12)

CONE	CUSTOM INSERT	CONE	CUSTOM INSERT
6x6	4x4	20x20	4x4
	5x5		6x6
	4x5		8x8
	3x6		10x10
			15x15
10x10	4x4		10x17
	6x6		3x23
	8x8		
	6x8	25x25	4x4
	3x11		6x6
			8x8
15x15	4x4		10x10
	6x6		15x15
	8x8		20x20
	10x10		10x23
	8x11		3x28
	3x17		

TABLE 3. Custom inserts manufactured with a low melting point metal alloy for all cones. All values are in units of centimeters.

tured by MultiData Systems International Corp. was used. This system consist of a 48 x 48 x 40 cm water phantom with automated scanning mechanisms, two PTW model M2332 0.1 cc ion chambers (cavity diameter = 0.35 cm), and a controller which is an IBM AT-compatible desktop computer running proprietary software with accompanying interface equipment.

Data acquisition is performed with this system by first, through software manipulation, developing an "acquisition plan file" which will control the positioning within the water phantom of one probe designated the "measurement probe." The other probe is set in a fixed position in the path of the beam and is designated the "reference probe." All data collected are relative to readings of this reference probe. This guards against dose output rate (i.e. cGy/min.) fluctuations of the accelerator which could compromise the data from measurement techniques involving the continuous repositioning of the measurement probe in the beam's path while radiation is being delivered. Collected data are stored in a separate "study file" for mathematical and / or graphical manipulation.

3.2 Relative Output Measurements

For each cone / insert / nominal beam energy combination, relative output measurements were performed by collecting ionization data at R_{100}. This was accomplished by the following procedure:

First, manually set the center of the measurement probe at both the center of the defined field and at the water surface of the phantom which was previously set at 100 cm from the "target" of the accelerator.

Second, following the recommendation of Attix (1), offset the probe 0.75 times the radius of the probe's active volume (i.e. 0.1 cm) away for the radiation beam "target" for all of the data measurement points. Set this position to be the scanning origin of the water phantom.

Third, by computer keyboard control, move the measurement probe to the previously determined R_{100} depth (see Section 3.3) for a specified cone / insert / nominal beam energy combination.

Fourth, collect the signal from the measurement probe with a PRM model SH-1 electrometer. This will be the ionization data for that specific combination.

Fifth, repeat the third and fouth steps until ionization data for all cone / insert / nominal beam energy combinations are acquired.

All ionization readings with the probe located at R_{100} for each cone / insert / nominal beam energy combination were normalized to the ionization readings with the probe at R_{100} for the 10x10 cone with the manufacturer supplied insert for each nominal beam energy. This yields relative output

values that were calculated by the following expression:

$$RELATIVE\ OUTPUT)_{Mod.} = \frac{IONIZATION\ READINGS)_{Mod.}}{IONIZATION\ READINGS)_{10x10}} \times 1.000\ \frac{cGy}{MU}$$

The 10x10 cone with Varian supplied insert combination for each beam had been previously calibrated to a value of 1.00 cGy/MU at the depth of maximum dose (i.e. D_{max}) with a NBS traceable calibration dosimetry system. This system consisted of the same PRM model SH-1 electrometer and a Capintec model PR-06G Farmer-type probe.

3.3 Mean Incident Energy (R_{50}) Measurements

For R_{50} measurements, relative ionization versus depth curves were acquired. This was performed for each cone / insert / nominal beam energy by the following procedure:

First, manually set the center of the measurement probe at both the center of the defined field and at the water surface of the phantom which was previously set at 100 cm from the "target" of the accelerator.

Second, following the recommendation of Attix (1), offset the probe 0.75 times the radius of the probe's active volume (i.e. 0.1 cm) away for the "target" for all of the data measurement points. Set this position as the scanning orgin of the water phantom.

Third, place the reference probe in the path of

the beam but not at a location that would interfere with the scanning mechanism.

Fourth, develop an acquisition plan that guides the probe into the water phantom along the central axis of the field at depth increments of 0.1 cm and to an absolute depth past the effective range of the electron beam's energy.

Fifth, with the system's electrometer time constant set at 0.2 seconds, have the probe pause 0.4 seconds at each depth increment or sampling point.

Sixth, enter the command to begin the acqusition of the ionization intensity vs depth data.

The scanning system software will automatically display the ionization intensity vs. depth scan normalized to the maximum ionization value. A printout is then acquired which contains depths of maximum ionization (R_{100}), 50% of maximum ionization (R_{50}), 55% of maximum ionization (R_{55}), and 45% of maximum ionization (R_{45}) values.

The combination of uncertainties in the previouly described steps involved in probe positioning results in an estimated uncertainty of 0.1 cm for the measured R_{50} value. Therefore, one pass / fail criterion for R_{50} model prediction will be set at 0.1 cm.

4.0 RESULTS

4.1 Data Combinations

Relative output and ionization intensity versus depth curves were measured for 180 nominal beam energy / cone / insert combinations. Thirty combinations were with Varian supplied inserts, 100 combinations were with custom square inserts and 50 combinations were with custom rectangular inserts.

4.2 Relative Output Measurements

Table 4 presents the relative output measurements for each nominal beam energy with all cone / manufacturer supplied inserts. Figure 2 presents these data graphically. A review of this graph indicates no consistent shape of the curves for all beams. This could be due to the different primary collimators settings for different cone / beam combinations and different construction dimensions for each individual cone as indicated in table 2. Table 5 presents the relative output measurements for all cone / square insert / nominal beam energy combinations. Figures 3 through 7 graphically present these data for each beam. As can be observed for these curves, there appears to be a consistent shape or trend for each nominal beam energy with

CONE	INSERT	6 MeV	9 MeV	12 MeV	16 MeV	20 MeV
6x6	4x4"	0.990	0.981	0.959	1.027	1.094
6x6	6x6	1.015	1.016	0.982	1.064	1.121
10x10	10x10	1.000	1.000	1.000	1.000	1.000
15x15	15x15	0.993	0.920	1.002	0.971	0.943
20x20	20x20	1.068	0.949	1.015	0.944	0.899
25x25	25x25	1.052	0.950	1.020	0.937	0.892

" Varian supplied insert for 6x6 cone.

TABLE 4. Relative output in units of cGy/MU for Varian supplied cones / inserts with all values normalized to the 10x10 cone.

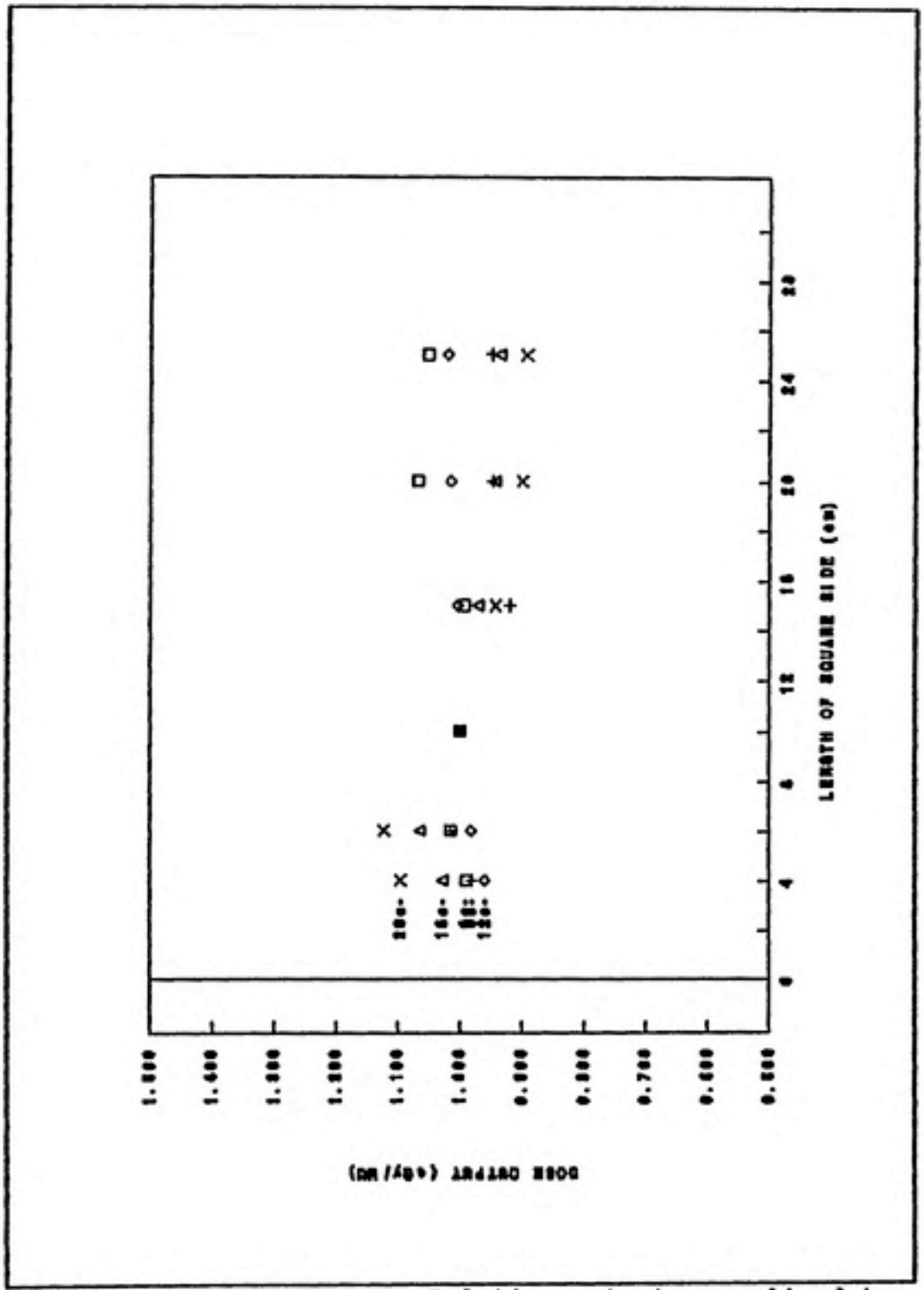

FIGURE 2. Varian Cones. Relative output normalized to the 10x10 cone for all nominal beam energies.

CONE	INSERT	6 MeV	9 MeV	12 MeV	16 MeV	20 MeV
6x6	4x4V	0.990	0.981	0.959	1.027	1.094
	4x4	0.982	0.980	0.948	1.016	1.064
	5x5	1.012	1.013	0.960	1.036	1.082
	6x6V	1.015	1.016	0.982	1.064	1.121
10x10	4x4	0.962	0.924	0.956	0.968	0.966
	6x6	1.001	0.990	0.992	0.992	0.990
	8x8	0.996	0.998	0.995	0.995	0.991
	10x10V	1.000	1.000	1.000	1.000	1.000
15x15	4x4	0.965	0.874	0.956	0.937	0.931
	6x6	0.993	0.920	0.998	0.961	0.941
	8x8	0.996	0.932	1.013	0.972	0.953
	10x10	0.995	0.930	1.012	0.980	0.954
	15x15V	0.993	0.920	1.002	0.971	0.943
20x20	4x4	1.030	0.895	0.965	0.923	0.906
	6x6	1.076	0.955	1.020	0.951	0.915
	8x8	1.078	0.962	1.031	0.957	0.918
	10x10	1.075	0.961	1.035	0.962	0.921
	15x15	1.068	0.956	1.029	0.958	0.919
	20x20V	1.068	0.949	1.020	0.944	0.899
25x25	4x4	1.017	0.904	0.979	0.934	0.913
	6x6	1.067	0.966	1.037	0.966	0.940
	8x8	1.072	0.974	1.047	0.973	0.939
	10x10	1.071	0.974	1.049	0.969	0.932
	15x15	1.064	0.964	1.040	0.966	0.924
	20x20	1.059	0.954	1.028	0.951	0.907
	25x25V	1.052	0.950	1.020	0.937	0.892

TABLE 5. Relative output in units of cGy/MU for custom square inserts and Varian square inserts normalized to the 10x10 cone.

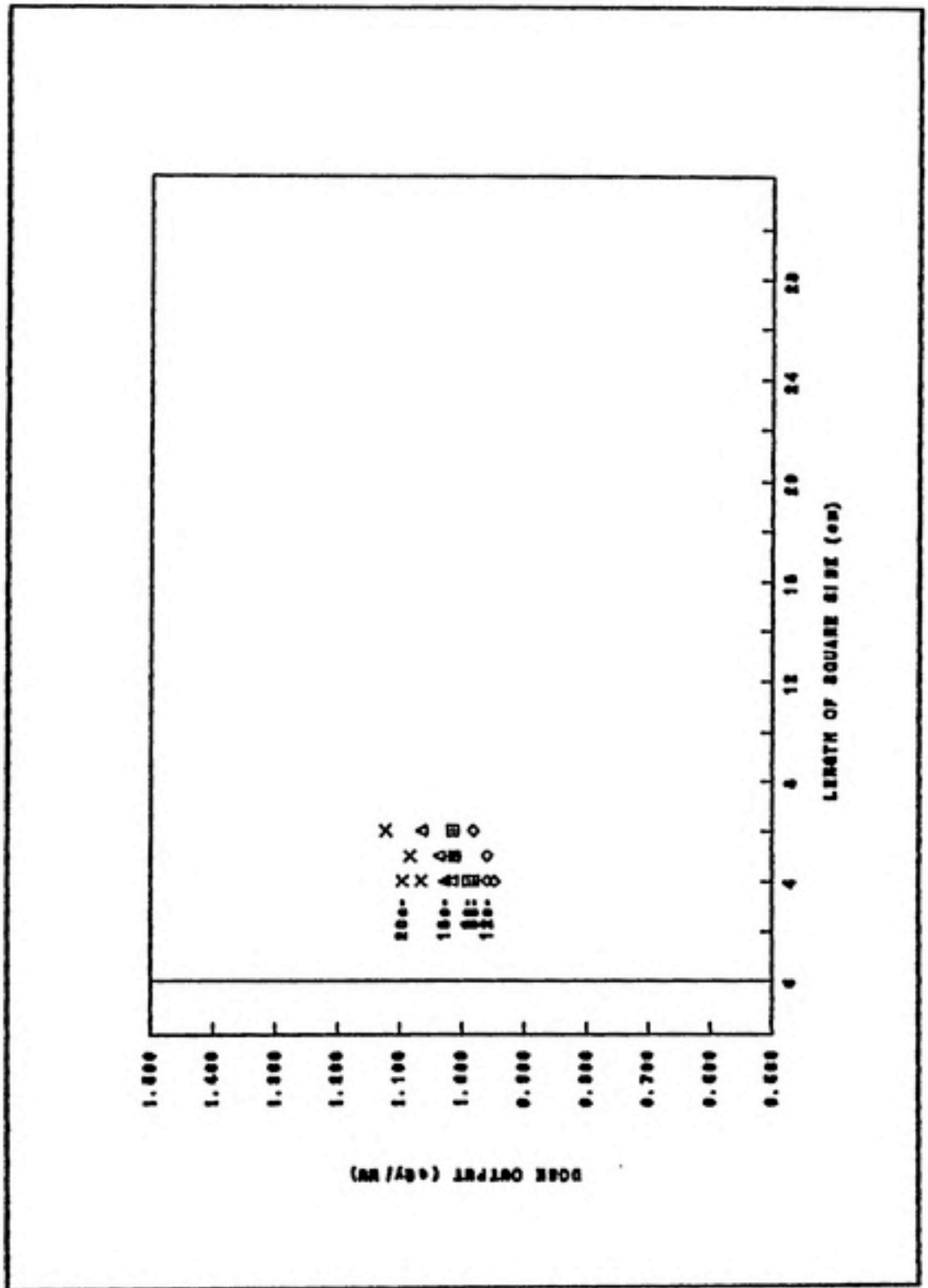

FIGURE 3. 6x6 Cone. Relative output normalized to the 10x10 cone for all nominal beam energies.

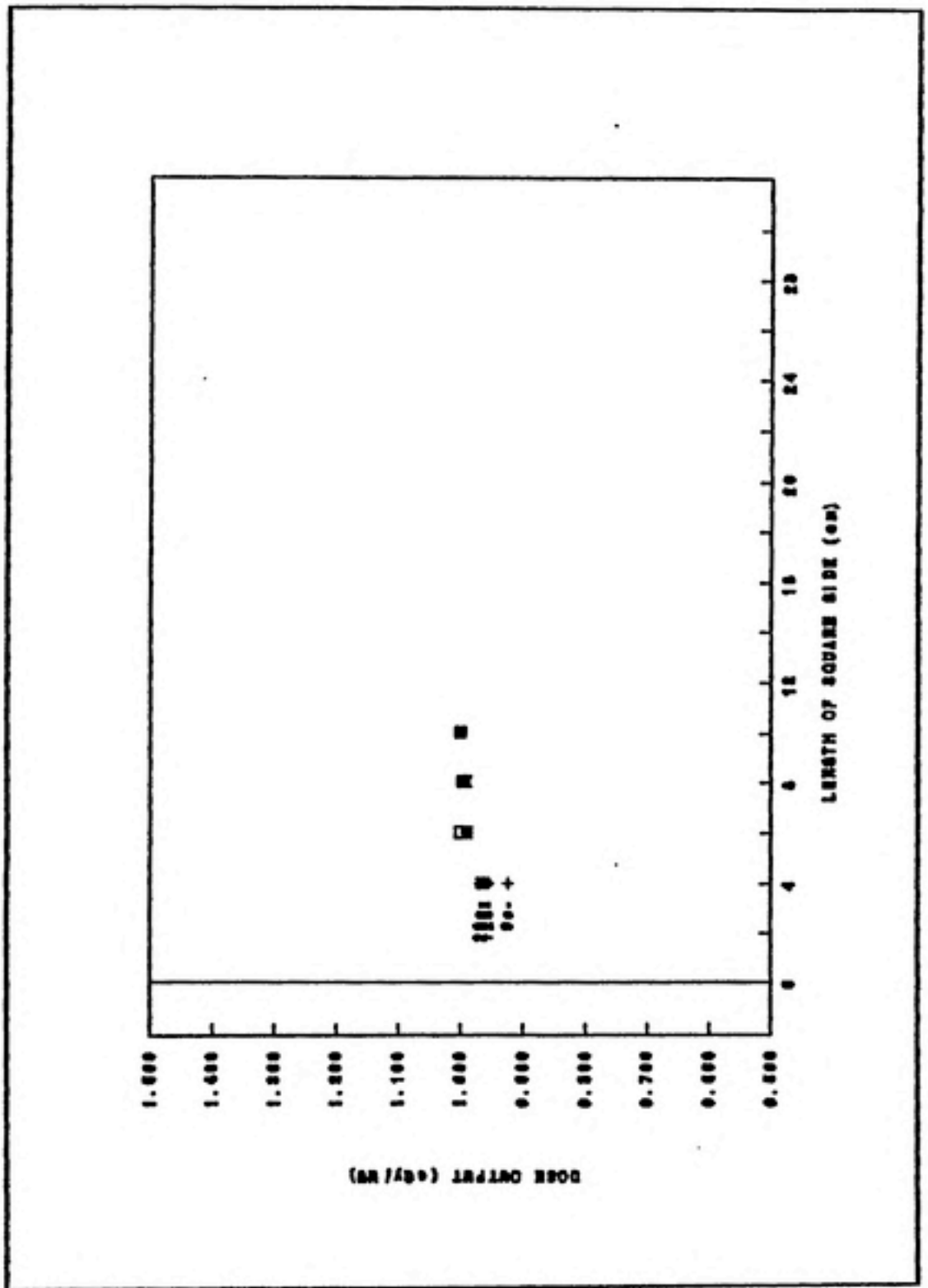

FIGURE 4. 10x10 Cone. Relative output normalized to the 10x10 cone for all nominal beam energies.

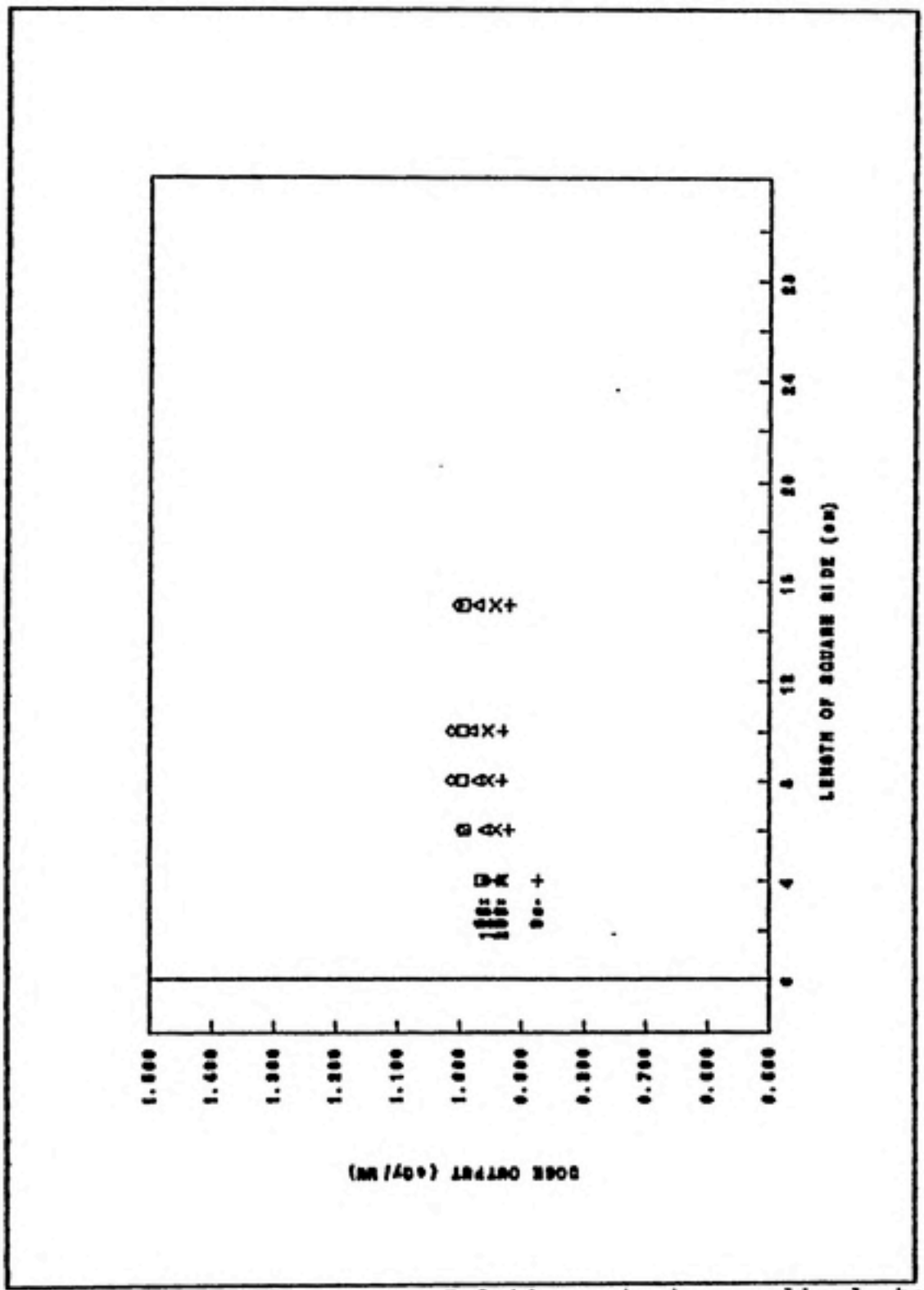

FIGURE 5. 15x15 Cone. Relative output normalized to the 10x10 cone for all nominal beam energies.

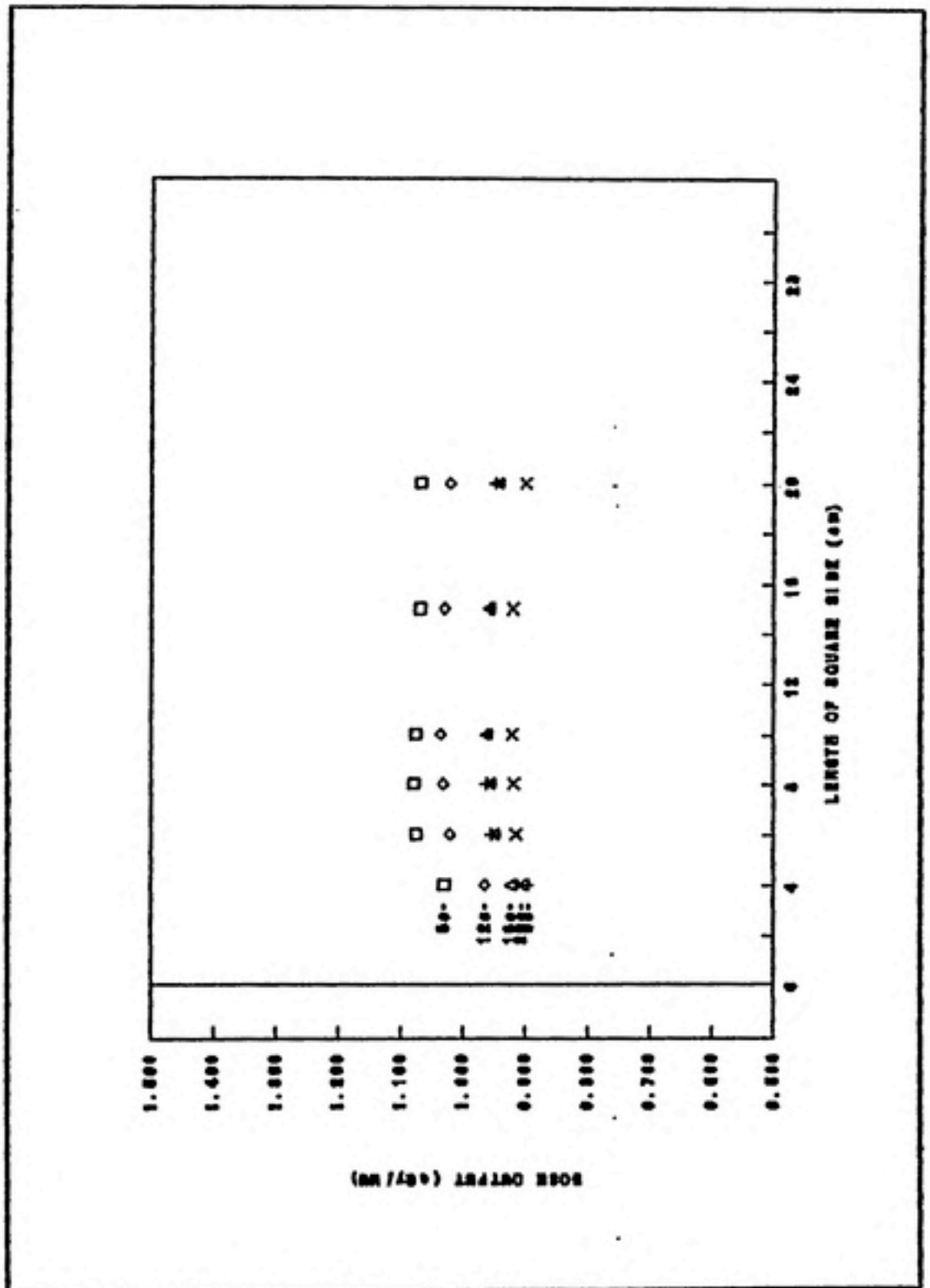

FIGURE 6. 20x20 Cone. Relative output normalized to the 10x10 cone for all nominal beam energies.

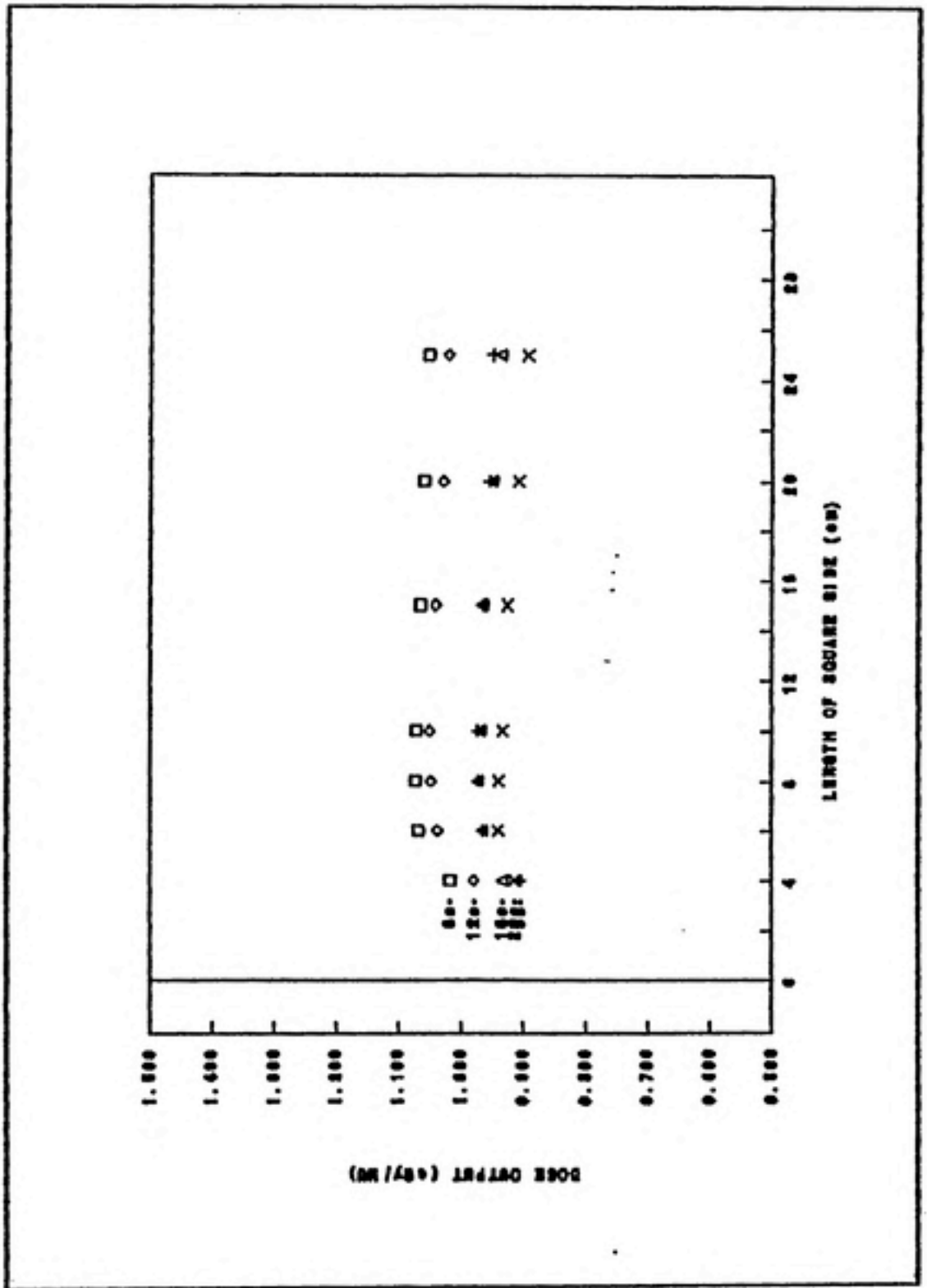

FIGURE 7. 25x25 Cone. Relative output normalized to the 10x10 cone for all nominal beam energies.

each individual cone.

For the 15x15 cone and greater (figures 5 through 7), this trend can be described as follows:

> A maximum output is observed between the 8x8 and 10x10 inserts. With increasing square field dimension, the relative output changes in a linear fashion with a slight negative slope of approximately -0.002 cGy/MU per cm of square side dimension. With decreasing square dimensions, a much sharper (3% to 6%) non-linear drop in output is observed.

The non-linear trend for smaller square dimensions is mimicked to a lesser degree in the 10x10 and 6x6 cone. One abnormality for the 6x6 cone was an apparent difference (especially for the higher energies) in output between the Varian supplied 4x4 insert and a 4x4 custom made insert. The data for the 4x4 and 5x5 custom inserts were used for relative output model prediction with non-standard custom rectangular inserts.

Table 6 presents the relative output measurements for the two rectangular custom inserts used in the present study for each cone / nominal beam energy combination.

4.3 Mean Incident Energy (R_{oo})

Table 7 presents mean incident energy (R_{oo}) measurements for all of the cone / manufacturer supplied insert

CONE	INSERT	6 MeV	9 MeV	12 MeV	16 MeV	20 MeV
6x6	4x5	1.000	0.997	0.963	1.023	1.048
	3x6	0.980	0.966	0.946	1.013	1.049
10x10	6x8	0.993	0.983	0.978	0.978	0.979
	3x11	0.953	0.912	0.937	0.946	0.946
15x15	8x11	1.004	0.930	1.013	0.978	0.950
	3x17	0.951	0.863	0.954	0.933	0.920
20x20	10x17	1.081	0.955	1.025	0.960	0.916
	3x23	1.011	0.884	0.964	0.918	0.890
25x25	10x23	1.063	0.946	1.021	0.948	0.893
	3x28	0.977	0.873	0.950	0.908	0.876

TABLE 6. Relative output in units of cGy/MU for custom rectangular inserts normalized to the 10x10 cone.

CONE	INSERT	6 MeV	9 MeV	12 MeV	16 MeV	20 MeV
6x6	4x4*	2.2	3.4	4.3	5.7	6.6
6x6	6x6	2.2	3.4	4.5	6.1	7.4
10x10	10x10	2.1	3.3	4.5	6.4	7.8
15x15	15x15	2.2	3.4	4.5	6.3	7.8
20x20	20x20	2.2	3.4	4.5	6.4	7.9
25x25	25x25	2.1	3.4	4.5	6.4	7.9

* Varian supplied insert for 6x6 cone.

TABLE 7. 50% of the maximum ionization depth in centimeters for Varian supplied cones and inserts.

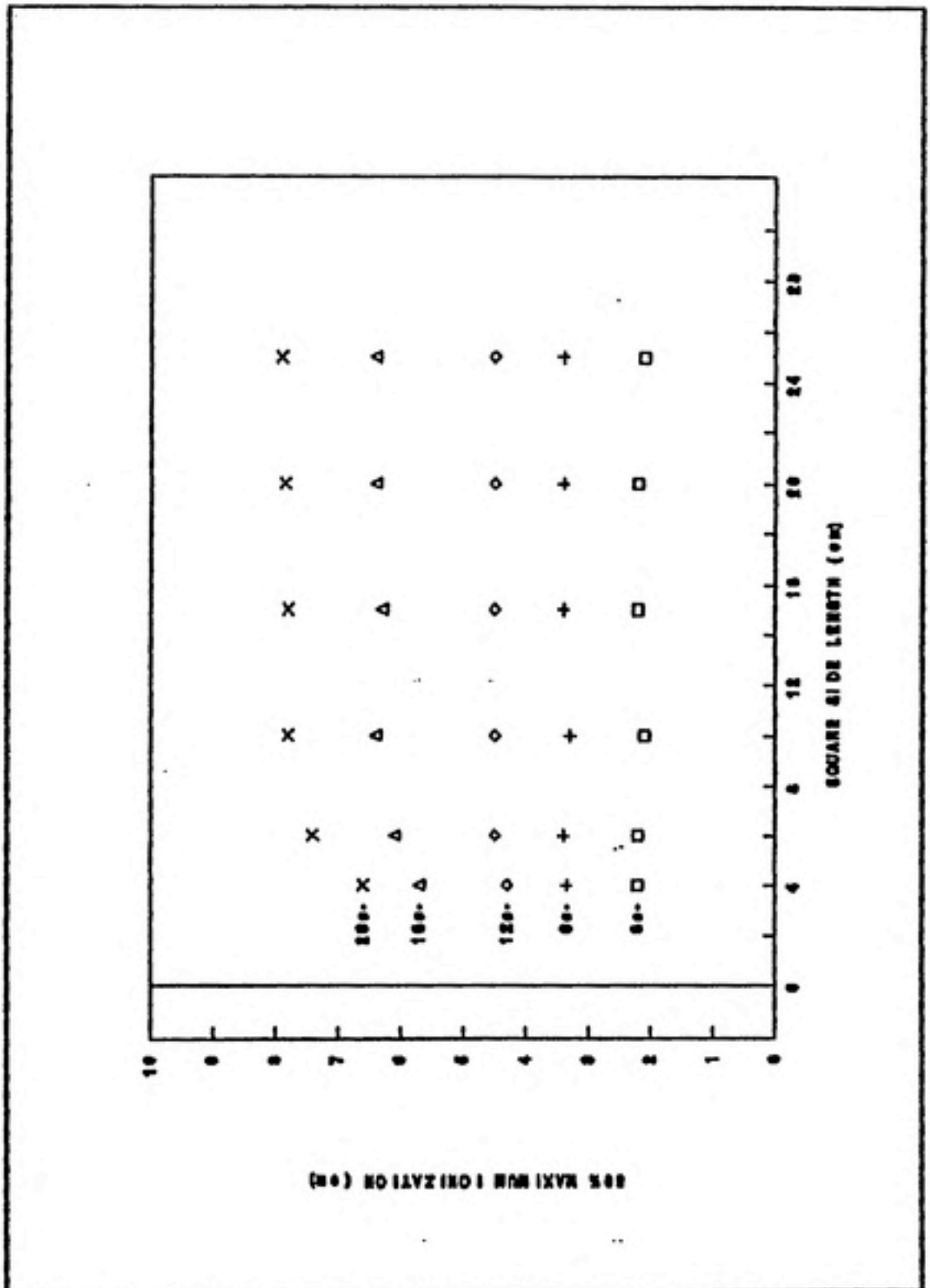

FIGURE 8. Varian Cones. 50% of maximum ionization depth for all nominal beam energies.

combinations. Figure 8 presents thes data graphically. As can be seen, for the 6 MeV, 9 MeV, and 12 MeV nominal beam energies, the R_{50} value remains constant for all combinations. For the 16 MeV and 20 MeV nominal beam energies, these data indicate a R_{50} value decrease for the 6x6 cone with the 6x6 and 4x4 inserts.

Table 8 presents the mean incident energy (R_{50}) measurements for each cone with their respective families of custom inserts. Figures 9 through 13 graphically present these data for each beam. A review of these graphs indicate a R_{50} value decrease for the 16 MeV and 20 MeV nominal beam energies with the 10x10 and greater dimension cones' 4x4 and 6x6 inserts. This R_{50} decrease for the smaller inserts is qualitatively similar to that noted earlier with the cone / manufacturer supplied inset combinations. The 6 MeV, 9 MeV, and 12 MeV nominal beam energies' data are constant for all inserts which is again comparable to data for the individual cones.

Table 9 presents mean incident energy (R_{50}) measurements for the two rectangular custom inserts used in the present study for each cone / nominal beam energy combination.

4.4 Model Application

For application of the square root model for both relative dose output and mean incident energy (R_{50}) predic-

CONE	INSERT	6 MeV	9 MeV	12 MeV	16 MeV	20 MeV
6x6	4x4V	2.2	3.4	4.3	5.7	6.6
	4x4	2.2	3.3	4.4	5.8	6.8
	5X5	2.1	3.3	4.4	6.2	7.3
	6x6V	2.2	3.4	4.5	6.1	7.4
10x10	4x4	2.1	3.3	4.3	5.9	6.8
	6x6	2.1	3.3	4.5	6.3	7.6
	8x8	2.1	3.3	4.5	6.4	7.8
	10x10V	2.1	3.3	4.5	6.4	7.8
15x15	4x4	2.2	3.4	4.4	6.0	7.0
	6x6	2.2	3.5	4.6	6.3	7.6
	8x8	2.2	3.5	4.6	6.3	7.7
	10x10	2.2	3.5	4.6	6.3	7.8
	15x15V	2.2	3.4	4.5	6.3	7.8
20x20	4x4	2.1	3.3	4.3	5.9	6.9
	6x6	2.1	3.4	4.5	6.3	7.6
	8x8	2.1	3.4	4.5	6.4	7.8
	10x10	2.1	3.4	4.5	6.5	7.8
	15x15	2.2	3.5	4.5	6.4	7.8
	20x20V	2.2	3.4	4.5	6.4	7.9
25x25	4x4	2.1	3.3	4.3	5.8	6.9
	6x6	2.1	3.4	4.5	6.3	7.7
	8x8	2.2	3.4	4.5	6.4	8.0
	10x10	2.2	3.4	4.5	6.4	8.0
	15x15	2.2	3.5	4.6	6.5	8.1
	20x20	2.1	3.4	4.5	6.3	7.9
	25x25V	2.1	3.4	4.5	6.4	7.9

TABLE 8. 50% of maximum ionization depth in centimeters for all square custom inserts and Varian supplied inserts.

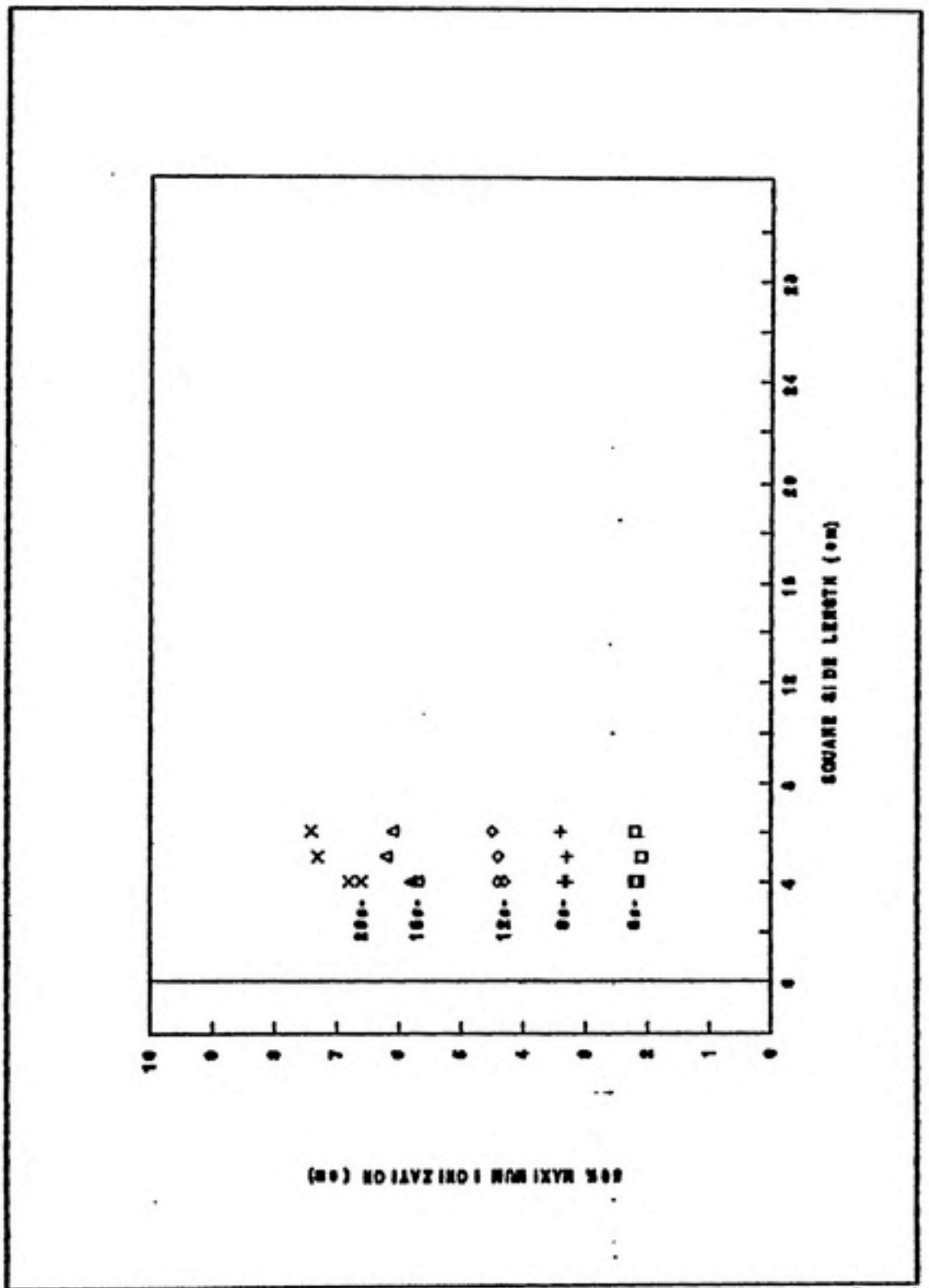

FIGURE 9. 6x6 Cone. 50% of maximum ionization depth for all nominal beam energies.

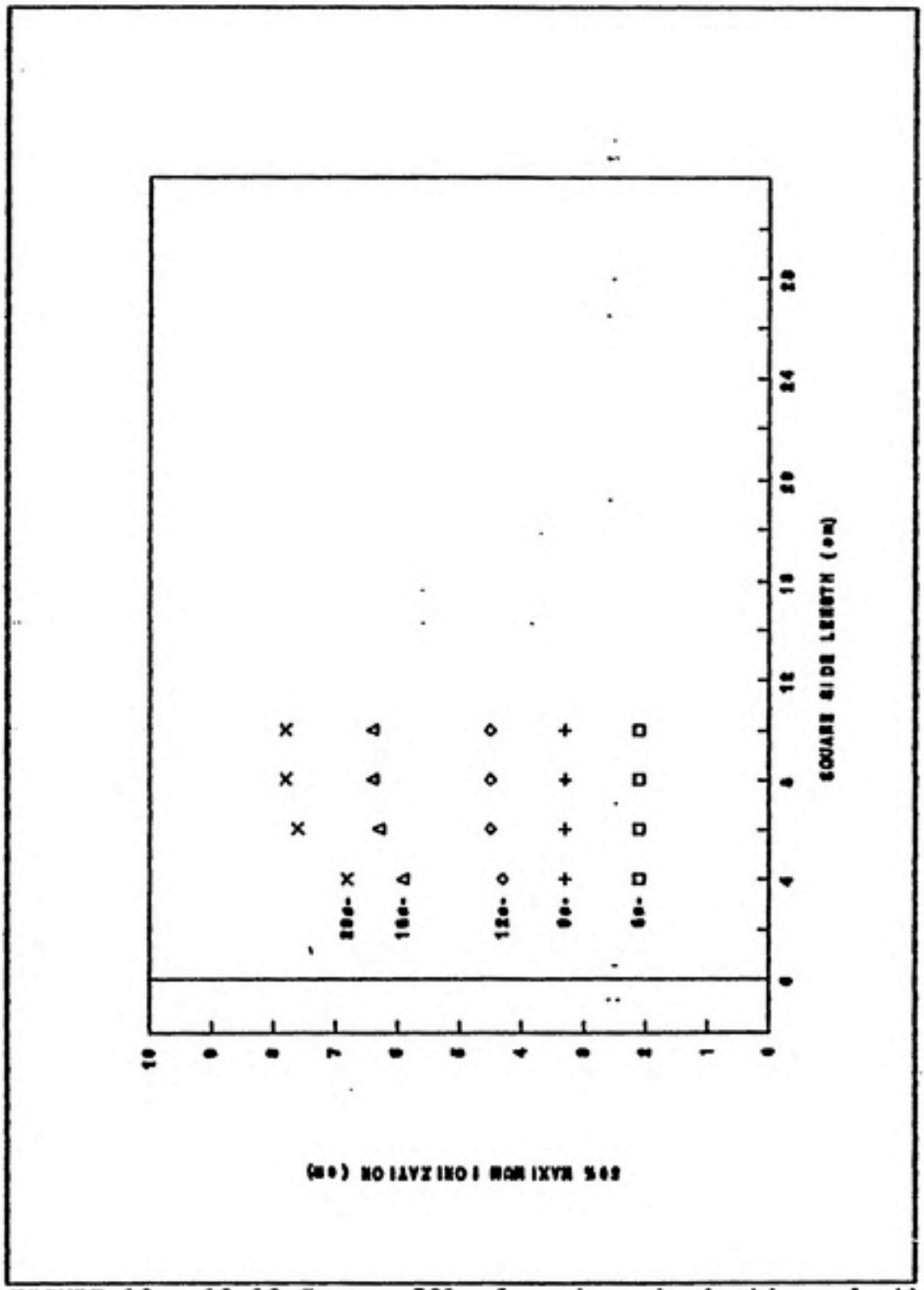

FIGURE 10. 10x10 Cone. 50% of maximum ionization depth for all nominal beam energies.

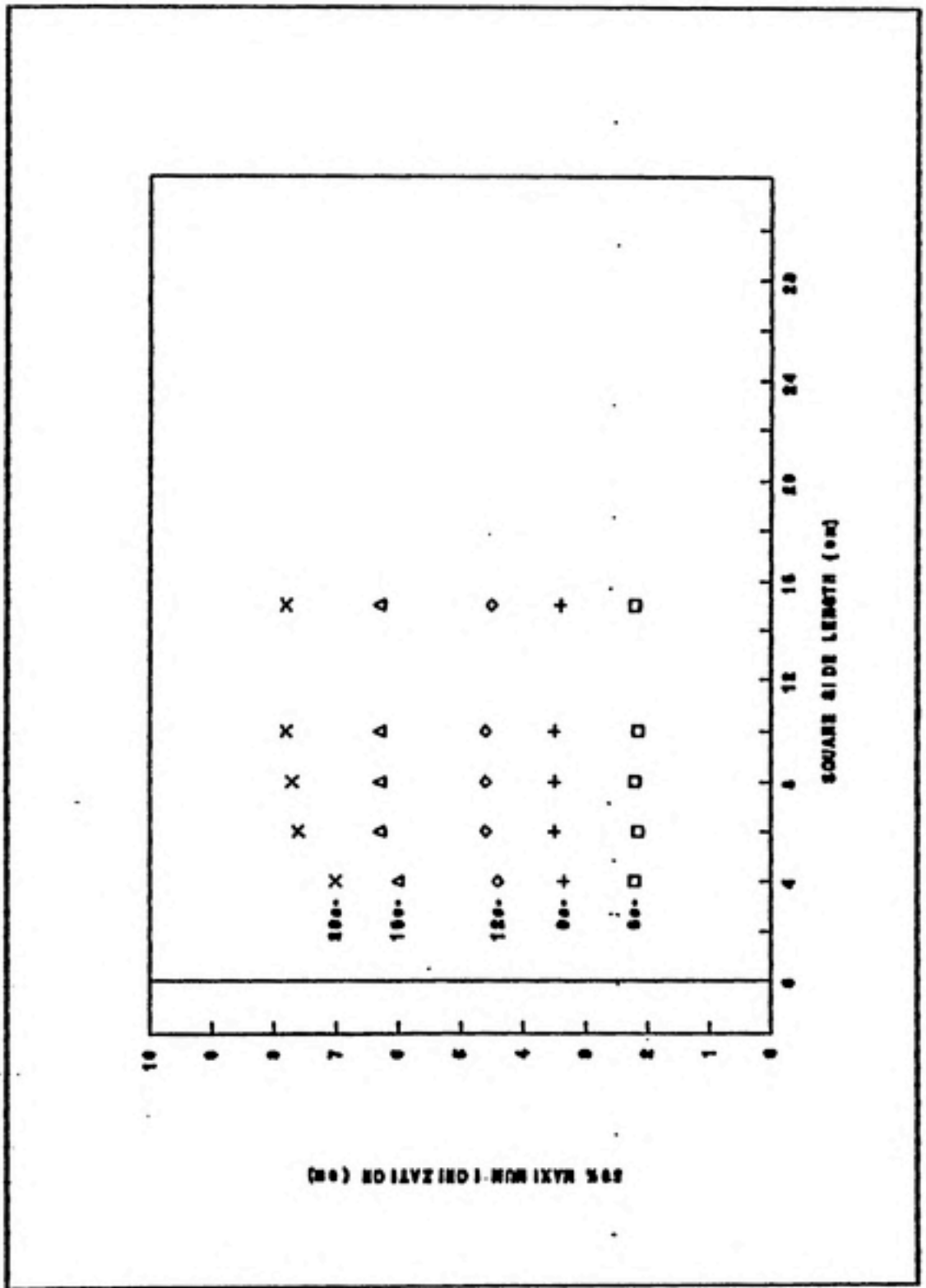

FIGURE 11. 15x15 Cone. 50% of maximum ionization depth for all nominal beam energies.

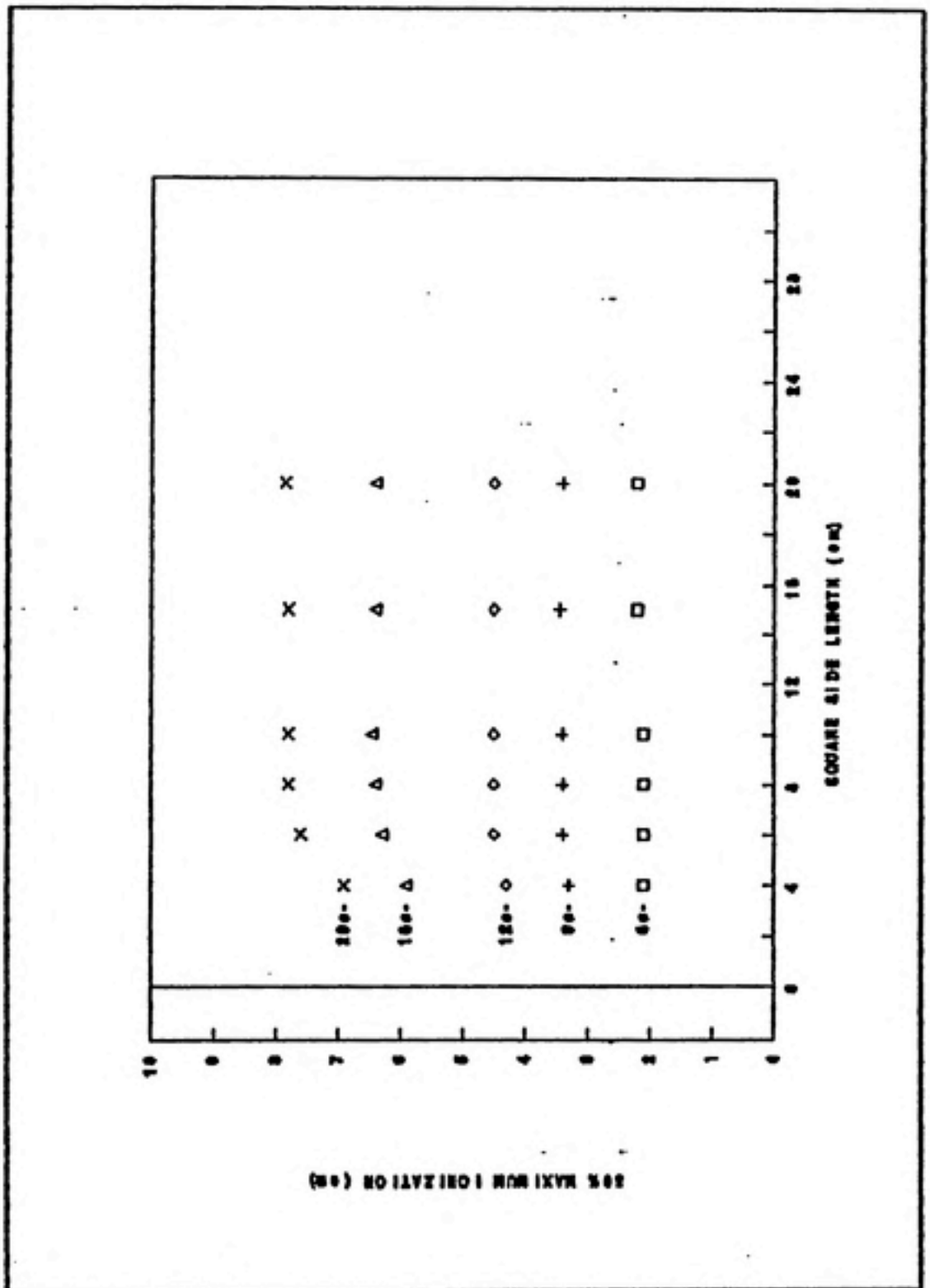

FIGURE 12. 20x20 Cone. 50% of maximum ionization depth for all nominal beam energies.

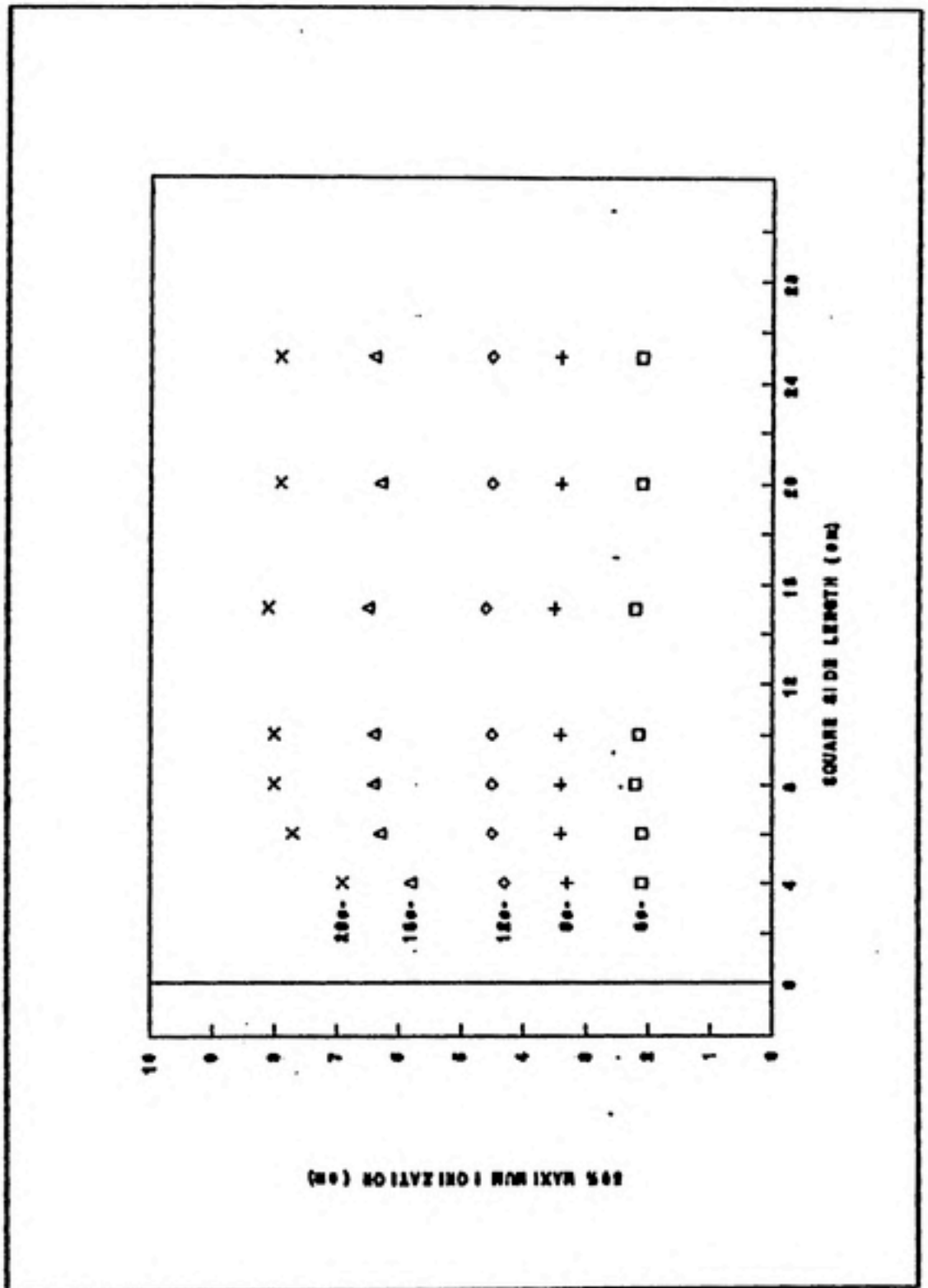

FIGURE 13. 25x25 Cone. 50% of maximum ionization depth for all nominal beam energies.

CONE	INSERT	6 MeV	9 MeV	12 MeV	16 MeV	20 MeV
6x6	4x5	2.1	3.3	4.4	5.9	6.9
	3x6	2.1	3.2	4.3	5.7	6.7
10x10	6x8	2.2	3.3	4.5	6.3	7.6
	3x11	2.2	3.3	4.4	5.9	6.9
15x15	8x11	2.2	3.4	4.5	6.4	7.8
	3x17	2.2	3.4	4.4	5.9	7.0
20x20	10x17	2.2	3.4	4.5	6.4	7.9
	3x23	2.2	3.4	4.4	5.9	7.1
25x25	10x23	2.2	3.4	4.5	6.4	7.9
	3x28	2.2	3.4	4.4	6.0	7.1

TABLE 9. 50% of maximum ionization depth in centimeters for custom rectangular inserts.

tion, a simple table look up algorithm was developed with linear interpolation for field defining dimensions between table values and linear extrapolation for field defining dimensions outside the table values. Examples of this algorithm are:

Example 1 - Relative output prediction using linear interpolation and equation 4.

Cone: 20 cm x 20 cm
Beam: 16 MeV
Table: 10d
Insert: 10 cm x 17 cm
$O^{10\times17}$ (measured) = 0.960 cGy/MU

$$O^{10\times10} = 0.962\ cGy/MU$$
$$O^{17\times17} = O^{15\times15} + \left[(17-15)\times\frac{O^{20\times20}-O^{15\times15}}{|20-15|}\right]$$
$$O^{17\times17} = 0.958 + \left[2\times\frac{0.944-0.958}{5}\right]$$
$$O^{17\times17} = 0.952\ cGy/MU$$

$$O^{10\times17} = \sqrt{O^{10\times10}\times O^{17\times17}}$$
$$O^{10\times17} = \sqrt{0.962\times0.952}$$
$$O^{10\times17} = 0.957\ cGy/MU$$

Example 2 - Energy (R_{50}) prediction using linear extrapolation and equation 5.

Cone: 20 cm x 20 cm
Beam: 16 MeV
Table: 11d
Insert: 3 cm x 23 cm
$DD^{3\times23}$ (measured R_{50} value) = 5.9 cm

$$DD^{3x3} = DD^{4x4} + \left[(4-3) \times \frac{DD^{4x4} - DD^{6x6}}{|4-6|} \right]$$
$$DD^{3x3} = 5.9 + \left[1 \times \frac{5.9-6.3}{2} \right]$$
$$DD^{3x3} = 5.7\ cm$$
$$DD^{23x23} = DD^{20x20} + \left[(20-17) \times \frac{DD^{20x20} - DD^{15x15}}{|20-15|} \right]$$
$$DD^{23x23} = 6.4 + \left[5 \times \frac{6.4-6.4}{5} \right]$$
$$DD^{23x23} = 6.4\ cm$$

$$DD^{3x23} = \sqrt{DD^{3x3} \times DD^{23x23}}$$
$$DD^{3x23} = \sqrt{5.7 \times 6.4}$$
$$DD^{3x23} = 6.0\ cm$$

Tables 10a through 10e present comparisons between the measured and predicted values of the relative output for all square and rectangular inserts for each cone and for each nominal beam energy, 6 MeV through 20 MeV respectively.

Tables 11a through 11e present comparisons between the measured and predicted values of R_{50} for square and rectangular inserts for each cone and for each nominal beam energy, 6 MeV through 20 MeV respectively.

Table 12 contains the variation in depth values between measured R_{50} and measured R_{40} (or R_{80}) for each nominal beam energy. These data are to be used as a possible pass / fail criterion for R_{50} model prediction.

Cone	Insert		Cone	Model	Cone	Model
		Meas.	Pred.	Pred.	%Diff.	%Diff.
6x6	4x4V	0.990	0.990	0.990	0.0%	0.0%
	6x6V	1.015	1.015	1.015	0.0%	0.0%
	4x4	0.982	0.990	0.982	0.8%	0.0%
	5x5	1.012	1.015	1.012	0.3%	0.0%
	4x5	0.997	1.015	0.997	1.8%	0.0%
	3x6	0.980	1.015	0.997	3.6%	1.7%
10x10	4x4	0.962	1.000	0.962	3.9%	0.0%
	6x6	1.001	1.000	1.001	-0.1%	0.0%
	8x8	0.996	1.000	0.996	0.4%	0.0%
	10x10V	1.000	1.000	1.000	0.0%	0.0%
	6x8	0.993	1.000	0.998	0.7%	0.5%
	3x11	0.953	1.000	0.972	4.9%	2.0%
15x15	4x4	0.965	0.993	0.965	2.9%	0.0%
	6x6	0.993	0.993	0.993	0.0%	0.0%
	8x8	0.996	0.993	0.996	-0.3%	0.0%
	10x10	0.995	0.993	0.995	-0.2%	0.0%
	15x15V	0.993	0.993	0.993	0.0%	0.0%
	8x11	1.004	0.993	0.995	-1.1%	-0.9%
	3x17	0.951	0.993	0.972	4.4%	2.2%

TABLE 10a. 6 MeV: Relative Output. Comparison between model prediction, assumption of no effect (cone), and actual measurement for Varian and custom inserts. All absolute values are in units of cGy/MU.

NOTE:

$$\%Diff = \left(\frac{O_{pred}}{O_{meas}} - 1\right) \times 100$$

Cone	Insert	Meas.	Cone Pred.	Model Pred.	Cone %Diff	Model %Diff.
20x20	4x4	1.030	1.068	1.030	3.7%	0.0%
	6x6	1.076	1.068	1.076	-0.7%	0.0%
	8x8	1.078	1.068	1.078	-0.9%	0.0%
	10x10	1.075	1.068	1.075	-0.6%	0.0%
	15x15	1.068	1.068	1.068	0.0%	0.0%
	20x20V	1.068	1.068	1.068	0.0%	0.0%
	10x17	1.081	1.068	1.071	-1.2%	-0.9%
	3x23	1.011	1.068	1.037	5.6%	2.6%
25x25	4x4	1.017	1.052	1.017	3.4%	0.0%
	6x6	1.067	1.052	1.067	-1.4%	0.0%
	8x8	1.072	1.052	1.072	-1.9%	0.0%
	10x10	1.071	1.052	1.071	-1.8%	0.0%
	15x15	1.064	1.052	1.064	-1.2%	0.0%
	20x20	1.059	1.052	1.059	-0.6%	0.0%
	25x25V	1.052	1.052	1.052	0.0%	0.0%
	10x23	1.063	1.052	1.063	-1.0%	0.0%
	3x28	0.977	1.052	1.020	7.7%	4.4%

TABLE 10a (cont.). 6 MeV: Relative Output. Comparison between model prediction, assumption of no effect (cone), and actual measurement for Varian and custom inserts. All absolute values are in units of cGy/MU.

Cone	Insert		Cone	Model	Cone	Model
		Meas.	Pred.	Pred.	%Diff	%Diff
6x6	4x4V	0.981	0.981	0.981	0.0%	0.0%
	6x6V	1.016	1.016	1.016	0.0%	0.0%
	4x4	0.980	1.016	0.980	3.7%	0.0%
	5x5	1.013	1.016	1.013	0.3%	0.0%
	4x5	0.997	1.016	0.996	1.9%	-0.1%
	3x6	0.966	1.016	0.996	5.2%	3.1%
10x10	4x4	0.924	1.000	0.924	8.2%	0.0%
	6x6	0.990	1.000	0.990	1.0%	0.0%
	8x8	0.998	1.000	0.998	0.2%	0.0%
	10x10V	1.000	1.000	1.000	0.0%	0.0%
	6x8	0.983	1.000	0.994	1.7%	1.1%
	3x11	0.912	1.000	0.944	9.6%	3.5%
15x15	4x4	0.874	0.920	0.874	5.3%	0.0%
	6x6	0.920	0.920	0.920	0.0%	0.0%
	8x8	0.932	0.920	0.932	-1.3%	0.0%
	10x10	0.930	0.920	0.930	-1.0%	0.0%
	15x15V	0.920	0.920	0.920	0.0%	0.0%
	8x11	0.930	0.920	0.930	-1.1%	0.0%
	3x17	0.863	0.920	0.883	6.6%	2.3%

TABLE 10b. 9 MeV: Relative Output. Comparison between model prediction, assumption of no effect (cone), and actual measurement for Varian and custom inserts. All absolute values are in units of cGy/MU.

Cone	Insert		Cone	Model	Cone	Model
		Meas.	Pred.	Pred.	%Diff	%Diff
20x20	4x4	0.895	0.949	0.895	6.0%	0.0%
	6x6	0.955	0.949	0.955	-0.6%	0.0%
	8x8	0.962	0.949	0.962	-1.4%	0.0%
	10x10	0.961	0.949	0.961	-1.3%	0.0%
	15x15	0.956	0.949	0.956	-0.7%	0.0%
	20x20V	0.949	0.949	0.949	0.0%	0.0%
	10x17	0.955	0.949	0.957	-0.6%	0.2%
	3x23	0.884	0.949	0.904	7.4%	2.3%
25x25	4x4	0.904	0.950	0.904	5.1%	0.0%
	6x6	0.966	0.950	0.966	-1.6%	0.0%
	8x8	0.974	0.950	0.974	-2.4%	0.0%
	10x10	0.974	0.950	0.974	-2.5%	0.0%
	15x15	0.964	0.950	0.964	-1.5%	0.0%
	20x20	0.954	0.950	0.954	-0.4%	0.0%
	25x25V	0.950	0.950	0.950	0.0%	0.0%
	10x23	0.946	0.950	0.962	0.4%	1.7%
	3x28	0.873	0.950	0.910	8.8%	4.2%

TABLE 10b (cont.). 9 MeV: Relative Output. Comparison between model prediction, assumption of no effect (cone), and actual measurement for Varian and custom inserts. All absolute values are in units of cGy/MU.

Cone	Insert		Cone	Model	Cone	Model
		Meas.	Pred.	Pred.	%Diff	%Diff
6x6	4x4V	0.959	0.959	0.959	0.0%	0.0%
	6x6V	0.982	0.982	0.982	0.0%	0.0%
	4x4	0.948	0.982	0.948	3.6%	0.0%
	5x5	0.960	0.982	0.960	2.3%	0.0%
	4x5	0.963	0.982	0.954	2.0%	-0.9%
	3x6	0.946	0.982	0.954	3.8%	0.8%
10x10	4x4	0.956	1.000	0.956	4.6%	0.0%
	6x6	0.992	1.000	0.992	0.8%	0.0%
	8x8	0.995	1.000	0.995	0.5%	0.0%
	10x10V	1.000	1.000	1.000	0.0%	0.0%
	6x8	0.978	1.000	0.993	2.2%	1.5%
	3x11	0.937	1.000	0.970	6.7%	3.5%
15x15	4x4	0.956	1.002	0.956	4.8%	0.0%
	6x6	0.998	1.002	0.998	0.4%	0.0%
	8x8	1.013	1.002	1.013	-1.1%	0.0%
	10x10	1.012	1.002	1.012	-1.0%	0.0%
	15x15V	1.002	1.002	1.002	0.0%	0.0%
	8x11	1.013	1.002	1.011	-1.1%	-0.2%
	3x17	0.954	1.002	0.966	5.0%	1.3%

TABLE 10c. 12 MeV: Relative Output. Comparison between model prediction, assumptiom of no effect (cone), and actual measurement for Varian and custom inserts. All absolute values are in units of cGy/MU.

Cone	Insert		Cone	Model	Cone	Model
		Meas.	Pred.	Pred.	%Diff	%Diff
20x20	4x4	0.965	1.015	0.965	5.2%	0.0%
	6x6	1.020	1.015	1.020	-0.5%	0.0%
	8x8	1.031	1.015	1.031	-1.5%	0.0%
	10x10	1.035	1.015	1.035	-1.9%	0.0%
	15x15	1.029	1.015	1.029	-1.3%	0.0%
	20x20V	1.020	1.015	1.020	-0.5%	0.0%
	10x17	1.025	1.015	1.030	-1.0%	0.5%
	3x23	0.964	1.015	0.975	5.3%	1.1%
25x25	4x4	0.979	1.020	0.979	4.2%	0.0%
	6x6	1.037	1.020	1.037	-1.6%	0.0%
	8x8	1.047	1.020	1.047	-2.6%	0.0%
	10x10	1.049	1.020	1.049	-2.8%	0.0%
	15x15	1.040	1.020	1.040	-1.9%	0.0%
	20x20	1.028	1.020	1.028	-0.8%	0.0%
	25x25V	1.020	1.020	1.020	0.0%	0.0%
	10x23	1.021	1.020	1.036	-0.1%	1.5%
	3x28	0.950	1.020	0.982	7.4%	3.4%

TABLE 10c (cont.). 12 MeV: Relative Output. Comparison between model prediction, assumption of no effect (cone), and actual measurements for Varian and custom inserts. All absolute values are in units of cGy/MU.

Cone	Insert		Cone	Model	Cone	Model
		Meas.	Pred.	Pred.	%Diff	%Diff
6x6	4x4V	1.027	1.027	1.027	0.0%	0.0%
	6x6V	1.064	1.064	1.064	0.0%	0.0%
	4x4	1.016	1.064	1.016	4.7%	0.0%
	5x5	1.036	1.064	1.036	2.7%	0.0%
	4x5	1.023	1.064	1.026	4.0%	0.3%
	3x6	1.013	1.064	1.026	5.0%	1.3%
10x10	4x4	0.968	1.000	0.968	3.3%	0.0%
	6x6	0.992	1.000	0.992	0.8%	0.0%
	8x8	0.995	1.000	0.995	0.5%	0.0%
	10x10V	1.000	1.000	1.000	0.0%	0.0%
	6x8	0.978	1.000	0.993	2.2%	1.5%
	3x11	0.946	1.000	0.979	5.7%	3.5%
15x15	4x4	0.937	0.971	0.937	3.6%	0.0%
	6x6	0.961	0.971	0.961	1.1%	0.0%
	8x8	0.972	0.971	0.972	-0.1%	0.0%
	10x10	0.980	0.971	0.980	-1.0%	0.0%
	15x15V	0.971	0.971	0.971	0.1%	0.0%
	8x11	0.978	0.971	0.975	-0.7%	-0.3%
	3x17	0.933	0.971	0.946	4.1%	1.4%

TABLE 10d. 16 MeV: Relative Output. Comparison between model prediction, assumption of no effect (cone), and actual measurement for Varian and custom inserts. All absolute values are in units of cGy/MU.

Cone	Insert		Cone	Model	Cone	Model
		Meas.	Pred.	Pred.	%Diff	%Diff
20x20	4x4	0.923	0.944	0.923	2.2%	0.0%
	6x6	0.951	0.944	0.951	-0.7%	0.0%
	8x8	0.957	0.944	0.957	-1.4%	0.0%
	10x10	0.962	0.944	0.962	-1.9%	0.0%
	15x15	0.958	0.944	0.958	-1.4%	0.0%
	20x20V	0.944	0.944	0.944	0.0%	0.0%
	10x17	0.960	0.944	0.957	-1.7%	-0.3%
	3x23	0.918	0.944	0.922	2.8%	0.4%
25x25	4x4	0.934	0.937	0.934	0.4%	0.0%
	6x6	0.966	0.937	0.966	-3.0%	0.0%
	8x8	0.973	0.937	0.973	-3.7%	0.0%
	10x10	0.969	0.937	0.969	-3.3%	0.0%
	15x15	0.966	0.937	0.966	-3.0%	0.0%
	20x20	0.951	0.937	0.951	-1.5%	0.0%
	25x25V	0.937	0.937	0.937	0.0%	0.0%
	10x23	0.948	0.937	0.956	-1.2%	0.8%
	3x28	0.908	0.937	0.923	3.2%	1.7%

TABLE 10d (cont.). 16 MeV: Relative Output. Comparison between model prediction, assumption of no effect (cone), and actual measurement for Varian and custom inserts. All absolute values are in units of cGy/MU.

Cone	Insert		Cone	Model	Cone	Model
		Meas.	Pred.	Pred.	%Diff	%Diff
6x6	4x4V	1.094	1.094	1.094	0.0%	0.0%
	6x6V	1.121	1.121	1.121	0.0%	0.0%
	4x4	1.064	1.121	1.064	5.4%	0.0%
	5x5	1.082	1.121	1.082	3.6%	0.0%
	4x5	1.048	1.121	1.073	7.0%	2.4%
	3x6	1.049	1.121	1.073	6.9%	2.3%
10x10	4x4	0.966	1.000	0.966	3.5%	0.0%
	6x6	0.990	1.000	0.990	1.0%	0.0%
	8x8	0.991	1.000	0.991	0.9%	0.0%
	10x10V	1.000	1.000	1.000	0.0%	0.0%
	6x8	0.979	1.000	0.990	2.1%	1.1%
	3x11	0.946	1.000	0.979	5.7%	3.5%
15x15	4x4	0.931	0.943	0.931	1.3%	0.0%
	6x6	0.941	0.943	0.941	0.2%	0.0%
	8x8	0.953	0.943	0.953	-1.0%	0.0%
	10x10	0.954	0.943	0.954	-1.1%	0.0%
	15x15V	0.943	0.943	0.943	0.0%	0.0%
	8x11	0.950	0.943	0.952	-0.7%	0.2%
	3x17	0.920	0.943	0.932	2.5%	1.3%

TABLE 10e. 20 MeV: Relative Output. Comparison between model prediction, assumption of no effect (cone), and actual measurement for Varian and custom inserts. All absolute values are in units of cGy/MU.

Cone	Insert		Cone	Model	Cone	Model
		Meas.	Pred.	Pred.	%Diff	%Diff
20x20	4x4	0.906	0.899	0.906	-0.8%	0.0%
	6x6	0.915	0.899	0.915	-1.7%	0.0%
	8x8	0.918	0.899	0.918	-2.1%	0.0%
	10x10	0.921	0.899	0.921	-2.4%	0.0%
	15x15	0.919	0.899	0.919	-2.2%	0.0%
	20x20V	0.899	0.899	0.899	0.0%	0.0%
	10x17	0.916	0.899	0.914	-1.9%	-0.2%
	3x23	0.890	0.899	0.894	1.0%	0.4%
25x25	4x4	0.913	0.892	0.913	-2.3%	0.0%
	6x6	0.940	0.892	0.940	-5.1%	0.0%
	8x8	0.939	0.892	0.939	-5.0%	0.0%
	10x10	0.932	0.892	0.932	-4.3%	0.0%
	15x15	0.924	0.892	0.924	-3.5%	0.0%
	20x20	0.907	0.892	0.907	-1.7%	0.0%
	25x25V	0.892	0.892	0.892	0.0%	0.0%
	10x23	0.893	0.892	0.915	-0.1%	2.5%
	3x28	0.876	0.892	0.891	1.8%	1.7%

TABLE 10e (cont.). 20 MeV: Relative Output. Comparison between model prediction, assumption of no effect (cone), and actual measurement for Varian and custom inserts. All absolute measurements are in units of cGy/MU.

Cone	Insert		Cone	Model	Cone	Model
		Meas.	Pred.	Pred.	Diff.	Diff.
6x6	4x4V	2.2	2.2	N/A	0.0	N/A
	6x6V	2.2	2.2	N/A	0.0	N/A
	4x4	2.2	2.2	N/A	0.0	N/A
	5x5	2.1	2.2	N/A	0.1	N/A
	4x5	2.1	2.2	N/A	0.1	N/A
	3x6	2.1	2.2	N/A	0.1	N/A
10x10	4x4	2.1	2.1	N/A	0.0	N/A
	6x6	2.1	2.1	N/A	0.0	N/A
	8x8	2.1	2.1	N/A	0.0	N/A
	10x10V	2.1	2.1	N/A	0.0	N/A
	6x8	2.2	2.1	N/A	-0.1	N/A
	3x11	2.2	2.1	N/A	-0.1	N/A
15x15	4x4	2.2	2.2	N/A	0.0	N/A
	6x6	2.2	2.2	N/A	0.0	N/A
	8x8	2.2	2.2	N/A	0.0	N/A
	10x10	2.2	2.2	N/A	0.0	N/A
	15x15V	2.2	2.2	N/A	0.0	N/A
	8x11	2.2	2.2	N/A	0.0	N/A
	3x17	2.2	2.2	N/A	0.0	N/A

TABLE 11a. 6 MeV: 50% of Maximum Ionization Depth. Comparison between assumption of no effect (cone), and actual measurement for Varian and custom inserts. As stated in the text, model prediction for this energy is unnecessary. All values in units of centimeters.

NOTE:

$$Diff)_{cone} = R_{50})_{cone} - R_{50})_{meas}$$
$$Diff)_{modal} = R_{50})_{modal} - R_{50})_{meas}$$

Cone	Insert		Cone	Model	Cone	Model
		Meas.	Pred.	Pred.	Diff.	Diff.
20x20	4x4	2.1	2.2	N/A	0.1	N/A
	6x6	2.1	2.2	N/A	0.1	N/A
	8x8	2.1	2.2	N/A	0.1	N/A
	10x10	2.1	2.2	N/A	0.1	N/A
	15x15	2.2	2.2	N/A	0.0	N/A
	20x20V	2.2	2.2	N/A	0.0	N/A
	10x17	2.2	2.2	N/A	0.0	N/A
	3x23	2.2	2.2	N/A	0.0	N/A
25x25	4x4	2.1	2.1	N/A	0.0	N/A
	6x6	2.1	2.1	N/A	0.0	N/A
	8x8	2.2	2.1	N/A	-0.1	N/A
	10x10	2.2	2.1	N/A	-0.1	N/A
	15x15	2.2	2.1	N/A	-0.1	N/A
	20x20	2.1	2.1	N/A	0.0	N/A
	25x25V	2.1	2.1	N/A	0.0	N/A
	10x23	2.2	2.1	N/A	-0.1	N/A
	3x28	2.2	2.1	N/A	-0.1	N/A

TABLE 11a (cont.). 6 MeV: 50% of Maximum Ionization Depth. Comparison between assumption of no effect (cone), and actual measurement for Varian and custom inserts. As stated in the text, model prediction for this energy is unnecessary. All values in units of centimeters.

Cone	Insert		Cone	Model	Cone	Model
		Meas.	Pred.	Pred.	Diff.	Diff.
6x6	4x4V	3.4	3.4	N/A	0.0	N/A
	6x6V	3.4	3.4	N/A	0.0	N/A
	4x4	3.3	3.4	N/A	0.1	N/A
	5x5	3.3	3.4	N/A	0.1	N/A
	4x5	3.3	3.4	N/A	0.1	N/A
	3x6	3.2	3.4	N/A	0.2	N/A
10x10	4x4	3.3	3.3	N/A	0.0	N/A
	6x6	3.3	3.3	N/A	0.0	N/A
	8x8	3.3	3.3	N/A	0.0	N/A
	10x10V	3.3	3.3	N/A	0.0	N/A
	6x8	3.3	3.3	N/A	0.0	N/A
	3x11	3.3	3.3	N/A	0.0	N/A
15x15	4x4	3.4	3.4	N/A	0.0	N/A
	6x6	3.5	3.4	N/A	-0.1	N/A
	8x8	3.5	3.4	N/A	-0.1	N/A
	10x10	3.5	3.4	N/A	-0.1	N/A
	15x15V	3.4	3.4	N/A	0.0	N/A
	8x11	3.4	3.4	N/A	0.0	N/A
	3x17	3.4	3.4	N/A	0.0	N/A

TABLE 11b. 9 MeV: 50% of Maximum Ionization Depth. Comparison between assumption of no effect (cone) and actual measurement for Varian and custom inserts. As stated in the text, model prediction for this energy is unnecessary. All values are in units of centimeters.

Cone	Insert		Cone	Model	Cone	Model
		Meas.	Pred.	Pred.	Diff.	Diff.
20x20	4x4	3.3	3.4	N/A	0.1	N/A
	6x6	3.4	3.4	N/A	0.0	N/A
	8x8	3.4	3.4	N/A	0.0	N/A
	10x10	3.4	3.4	N/A	0.0	N/A
	15x15	3.5	3.4	N/A	-0.1	N/A
	20x20V	3.4	3.4	N/A	0.0	N/A
	10x17	3.4	3.4	N/A	0.0	N/A
	3x23	3.4	3.4	N/A	0.0	N/A
25x25	4x4	3.3	3.4	N/A	0.1	N/A
	6x6	3.4	3.4	N/A	0.0	N/A
	8x8	3.4	3.4	N/A	0.0	N/A
	10x10	3.4	3.4	N/A	0.0	N/A
	15x15	3.5	3.4	N/A	-0.1	N/A
	20x20	3.4	3.4	N/A	0.0	N/A
	25x25V	3.4	3.4	N/A	0.0	N/A
	10x23	3.4	3.4	N/A	0.0	N/A
	3x28	3.4	3.4	N/A	0.0	N/A

TABLE 11b (cont.). 9 MeV: 50% of Maximum Ionization Depth. Comparison between assumption of no effect (cone) and actual measurement for Varian and custom inserts. As stated in the text, model prediction for this energy is unnecessary. All values are in units of centimeters.

Cone	Insert		Cone	Model	Cone	Model
		Meas.	Pred.	Pred.	Diff.	Diff.
6x6	4x4V	4.3	4.3	N/A	0.0	N/A
	6x6V	4.5	4.5	N/A	0.0	N/A
	4x4	4.4	4.5	N/A	0.1	N/A
	5x5	4.4	4.5	N/A	0.1	N/A
	4x5	4.4	4.5	N/A	0.1	N/A
	3x6	4.3	4.5	N/A	0.2	N/A
10x10	4x4	4.3	4.5	N/A	0.2	N/A
	6x6	4.5	4.5	N/A	0.0	N/A
	8x8	4.5	4.5	N/A	0.0	N/A
	10x10V	4.5	4.5	N/A	0.0	N/A
	6x8	4.5	4.5	N/A	0.0	N/A
	3x11	4.4	4.5	N/A	0.1	N/A
15x15	4x4	4.4	4.5	N/A	0.1	N/A
	6x6	4.6	4.5	N/A	-0.1	N/A
	8x8	4.6	4.5	N/A	-0.1	N/A
	10x10	4.6	4.5	N/A	-0.1	N/A
	15x15V	4.5	4.5	N/A	0.0	N/A
	8x11	4.5	4.5	N/A	0.0	N/A
	3x17	4.4	4.5	N/A	0.1	N/A

TABLE 11c. 12 MeV: 50% of Maximum Ionization Depth. Comparison between assumption of no effect (cone) and actual measurement for Varian and custom inserts. As stated in the text, model prediction for this energy is unnecessary. All values are in units of centimeters.

Cone	Insert		Cone	Model	Cone	Model
		Meas.	Pred.	Pred.	Diff.	Diff.
20x20	4x4	4.3	4.5	N/A	0.2	N/A
	6x6	4.5	4.5	N/A	0.0	N/A
	8x8	4.5	4.5	N/A	0.0	N/A
	10x10	4.5	4.5	N/A	0.0	N/A
	15x15	4.5	4.5	N/A	0.0	N/A
	20x20V	4.5	4.5	N/A	0.0	N/A
	10x17	4.5	4.5	N/A	0.0	N/A
	3x23	4.4	4.5	N/A	0.1	N/A
25x25	4x4	4.3	4.5	N/A	0.2	N/A
	6x6	4.5	4.5	N/A	0.0	N/A
	8x8	4.5	4.5	N/A	0.0	N/A
	10x10	4.5	4.5	N/A	0.0	N/A
	15x15	4.6	4.5	N/A	-0.1	N/A
	20x20	4.5	4.5	N/A	0.0	N/A
	25x25V	4.5	4.5	N/A	0.0	N/A
	10x23	4.5	4.5	N/A	0.0	N/A
	3x28	4.4	4.5	N/A	0.1	N/A

TABLE 11c (cont.). 12 MeV: 50% of Maximum Ionization Depth. Comparison between assumption of no effect (cone) and actual measurement for Varian and custom inserts. As stated in the text, model prediction for this energy is unnecessary. All values are in units of centimeters.

Cone	Insert		Cone	Model	Cone	Model
		Meas.	Pred.	Pred.	Diff.	Diff.
6x6	4x4V	5.7	5.7	5.8	0.0	0.1
	6x6V	6.1	6.1	6.2	0.0	0.1
	4x4	5.8	6.1	5.8	0.3	0.0
	5x5	6.0	6.1	6.0	0.1	0.0
	4x5	5.9	6.1	5.9	0.2	0.0
	3x6	5.7	6.1	5.9	0.4	0.2
10x10	4x4	5.9	6.4	5.9	0.5	0.0
	6x6	6.3	6.4	6.3	0.1	0.0
	8x8	6.4	6.4	6.4	0.0	0.0
	10x10V	6.4	6.4	6.4	0.0	0.0
	6x8	6.3	6.4	6.3	0.1	0.0
	3x11	5.9	6.4	6.0	0.5	0.1
15x15	4x4	6.0	6.3	6.0	0.3	0.0
	6x6	6.3	6.3	6.3	0.0	0.0
	8x8	6.3	6.3	6.3	0.0	0.0
	10x10	6.3	6.3	6.3	0.0	0.0
	15x15V	6.3	6.3	6.3	0.0	0.0
	8x11	6.4	6.3	6.3	-0.1	-0.1
	3x17	5.9	6.3	6.1	0.4	0.2

TABLE 11d. 16 MeV: 50% of Maximum Ionization Depth. Comparison between model prediction, assumption of no effect (cone), and actual measurement for Varian and custom insert. All values are in units of centimeters.

Cone	Insert		Cone	Model	Cone	Model
		Meas.	Pred.	Pred.	Diff.	Diff.
20x20	4x4	5.9	6.4	5.9	0.5	0.0
	6x6	6.3	6.4	6.3	0.1	0.0
	8x8	6.4	6.4	6.4	0.0	0.0
	10x10	6.5	6.4	6.5	-0.1	0.0
	15x15	6.4	6.4	6.4	0.0	0.0
	20x20V	6.4	6.4	6.4	0.0	0.0
	10x17	6.4	6.4	6.4	0.0	0.0
	3x23	5.9	6.4	6.0	0.5	0.1
25x25	4x4	5.8	6.4	5.8	0.6	0.0
	6x6	6.3	6.4	6.3	0.1	0.0
	8x8	6.4	6.4	6.4	0.0	0.0
	10x10	6.4	6.4	6.4	0.0	0.0
	15x15	6.5	6.4	6.5	-0.1	0.0
	20x20	6.3	6.4	6.3	0.1	0.0
	25x25V	6.4	6.4	6.4	0.0	0.0
	10x23	6.4	6.4	6.4	0.0	0.0
	3x28	6.0	6.4	6.0	0.4	0.0

TABLE 11d (cont.). 16 MeV: 50% of Maximum Ionization Depth. Comparison between model prediction, assumption of no effect (cone), and actual measurement for Varian and custom inserts. All values are in units of centimeters.

Cone	Insert		Cone	Model	Cone	Model
		Meas.	Pred.	Pred.	Diff.	Diff.
6x6	4x4V	6.6	6.6	6.8	0.0	0.2
	6x6V	7.4	7.4	7.4	0.0	0.0
	4x4	6.8	7.4	6.8	0.6	0.0
	5x5	7.1	7.4	7.1	0.3	0.0
	4x5	6.9	7.4	6.9	0.5	0.0
	3x6	6.7	7.4	6.9	0.7	0.2
10x10	4x4	6.8	7.8	6.8	1.0	0.0
	6x6	7.6	7.8	7.6	0.2	0.0
	8x8	7.8	7.8	7.8	0.0	0.0
	10x10V	7.8	7.8	7.8	0.0	0.0
	6x8	7.6	7.8	7.7	0.2	0.1
	3x11	6.9	7.8	7.1	0.9	0.2
15x15	4x4	7.0	7.8	7.0	0.8	0.0
	6x6	7.6	7.8	7.6	0.2	0.0
	8x8	7.7	7.8	7.7	0.1	0.0
	10x10	7.8	7.8	7.8	0.0	0.0
	15x15V	7.8	7.8	7.8	0.0	0.0
	8x11	7.8	7.8	7.7	0.0	-0.1
	3x17	7.0	7.8	7.2	0.8	0.2

TABLE 11e. 20 MeV: 50% of Maximum Ionization Depth. Comparison between model prediction, assumption of no effect (cone), and actual measurement for Varian and custom inserts. All values are in units of centimeters.

Cone	Insert		Cone	Model	Cone	Model
		Meas.	Pred.	Pred.	Diff.	Diff.
20x20	4x4	6.9	7.9	6.9	1.0	0.0
	6x6	7.6	7.9	7.6	0.3	0.0
	8x8	7.8	7.9	7.8	0.1	0.0
	10x10	7.8	7.9	7.8	0.1	0.0
	15x15	7.8	7.9	7.8	0.1	0.0
	20x20V	7.9	7.9	7.9	0.0	0.0
	10x17	7.9	7.9	7.8	0.0	-0.1
	3x23	7.1	7.9	7.2	0.8	0.1
25x25	4x4	6.9	7.9	6.9	1.0	0.0
	6x6	7.7	7.9	7.7	0.2	0.0
	8x8	8.0	7.9	8.0	-0.1	0.0
	10x10	8.0	7.9	8.0	-0.1	0.0
	15x15	8.1	7.9	8.1	-0.2	0.0
	20x20	7.9	7.9	7.9	0.0	0.0
	25x25V	7.9	7.9	7.9	0.0	0.0
	10x23	7.9	7.9	8.0	0.0	0.1
	3x28	7.1	7.9	7.2	0.8	0.1

TABLE 11e (cont.). 20 MeV: 50% of Maximum Ionization Depth. Comparison between model prediction, assumption of no effect (cone), and actual measurement for Varian and custom inserts. All values are in units of centimeters.

Nominal Beam Energy	R_{50} to R_{45} (or R_{55}) Difference
6 MeV	< 0.1 cm
9 MeV	< 0.1 cm
12 MeV	0.1 cm
16 MeV	0.2 cm
20 MeV	0.2 cm

TABLE 12. Variation in depths between R_{50} (50% of maximum ionization depth) and R_{45} (45% of maximum ionization depth) or R_{55} (55% of maximum ionization depth) for each nominal beam energy. Data taken with a 15x15 cone and Varian supplied square insert. These values are to be used as an option for setting acceptable variation limits between R_{50} model prediction and R_{50} measurement.

5.0 DISCUSSION

5.1 Relative Output

The variation between relative output value measurements for custom and Varian inserts indicates a need for a predictive model for all nominal beam energies. As indicated in table 13, for the 100 nominal beam energy / cone / custom square insert combinations, the prediction of no effect of relative output with custom inserts (i.e. the relative output for the Varian inserts for each nominal beam energy / cone), varied from the measured relative output by more than the 1.0% criteria 60 times with a maximum variation of 8.2%. For the 50 combinations with rectangular inserts, the prediction of no effect with using custom inserts resulted in variation from measurements greater than 1.0% occurring 40 times with a maximum variation of 9.6%.

Table 13 also presents the performance of the relative output square root model (equation 4). Due to the table look-up nature of the algorithm used in applying this model, one would expect very good agreement between model prediction and measured values for the custom square insert combinations. This is true with all 100 combinations exactly agreeing with measured values. For the 50 rectangular custom insert combinations, the model predictions exceeded the 1.0% variation criteria 30 times with a maximum varia-

	Number	Cone Prediction		Square Root Model	
		Passed	Failed	Passed	Failed
Square Varian Inserts	30	30	0	30	0
Square Custom Inserts	100	60	40	100	0
Rectangular Custom Inserts	50	10	40	20	30
TOTAL	180	100	80	150	30
Maximum Variation From Measurements			9.6%		4.4%

TABLE 13. Comparison of relative output measurements and the quality of predictions.
Pass / Fail Criteria: 1.0% variation from measurements (see Section 1.5.1)

tion of 4.4%. Dividing this category further, the 25 inserts with a small length to width ratio exceeded the variation criteria 8 times with all variation values ranging from -0.9% to 2.5%. The 25 inserts with a large length to width ratio exceeded the variation criteria 22 times with all variation values ranging from 0.4% to 4.4%.

The model does show improvement for the rectangular inserts relative to the assumption of no observable effect in that the magnitude of the variation between prediction and measurement is reduced. This can be shown by comparing the percent of predictions that meet a specified criteria to various variation limits. This is presented graphically in figure 14. Also, figure 14 allows the reader the option of evaluating one, the need of a predictive model and two, the model's performance for criteria limits greater than the 1.0% variation limit set for this study.

Even though the magnitude of the variation from measurement is reduced, a positive bias of the variation values is apparent (i.e. the model over estimates the relative output value). This is especially true for the inserts with a high length to width ratio. The indicated bias could be due to the extrapolation routine needed for the generation of an estimated relative output value for the narrow field dimension. For example, from table 10a the model prediction of relative output for the 6 MeV beam with a 3x28 insert is 4.4% greater than measured. The estimated relative output for a 3x3 insert extrapolated from the 4x4 and 6x6 data is

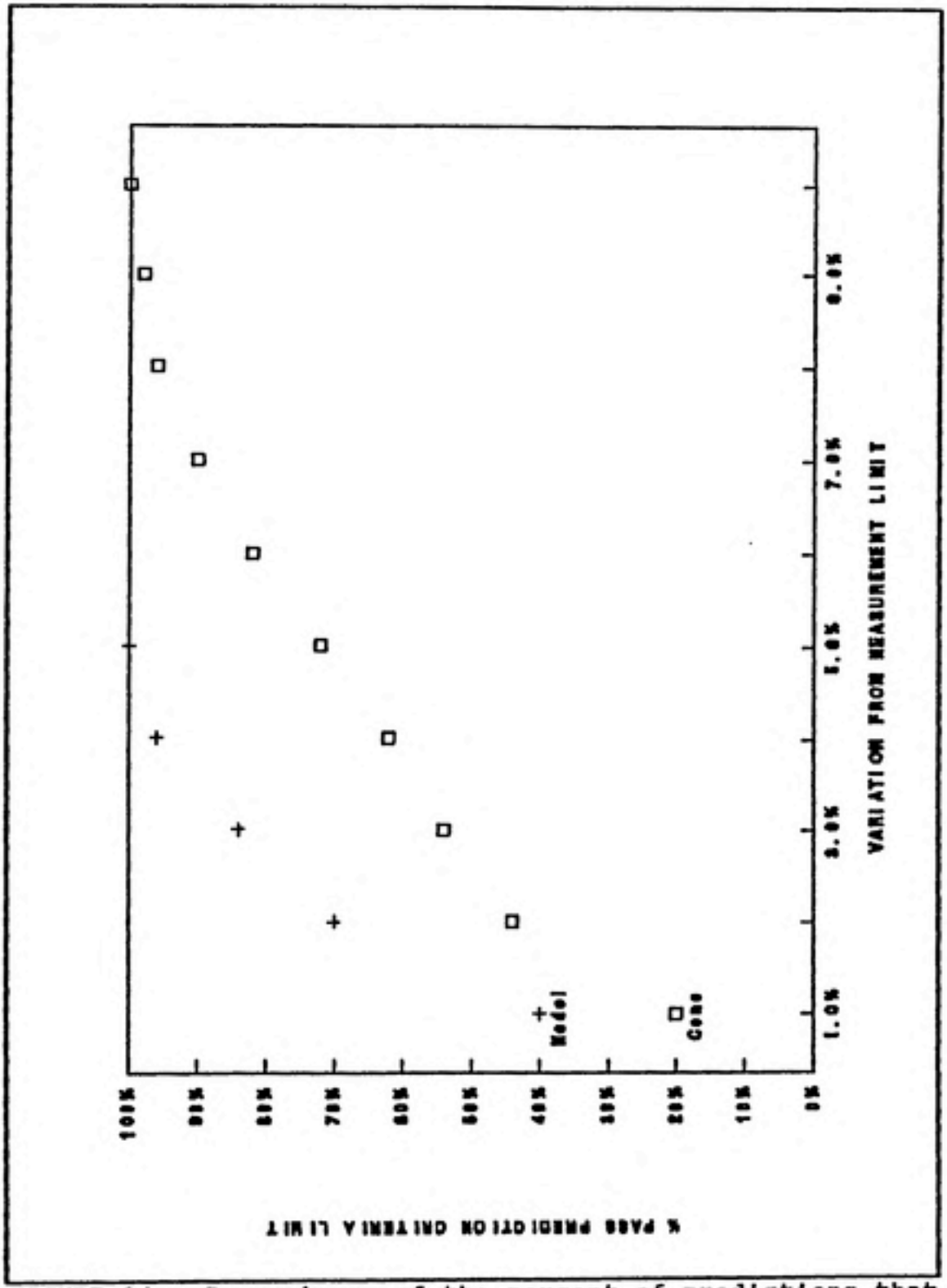

FIGURE 14. Comparison of the percent of predictions that would pass based on a specified criteria versus increasing variation criteria limits.

0.992 cGy/MU. If this linear extrapolation was used to estimate a 0x0 insert (i.e. a fully blocked field), the estimated relative output would be 0.917 cGy/MU. This is clearly an incorrect and much too high value. The ability to measure the relative output for smaller field defining inserts by some alternative method, such as the use of film dosimetry (9), may be a solution to the apparent bias exhibited in this study.

Another possible problem with implementation of this model for relative output prediction that was alluded to previously is the application of a model based on a different mode of electron beam production. While primary effects arise for beam production, beam shaping yield secondary effects. In particular, the square root model ignores the effect of electron scatter of the collimation devices of the accelerator.

5.2 Mean Incident Energy (R_{so})

The effectively constant R_{so} values for the 6 MeV, 9 MeV, and 12 MeV nominal beam energies indicate a lack of need for an energy prediction model at these energies. Of the 90 nominal beam energy / cone / custom insert combinations, the R_{so} measurements for the custom inserts varied from the Varian inserts' R_{so} value by more than the 0.1 cm criteria, applicable for these 3 beams, a total of 5 times (94% pass). For these 5 instances of non-agreement (3

square and 2 rectangular inserts), the variation was 0.2 cm. Therefore, the assumption of no significant mean incident energy shift, resulting in the use of custom inserts, appears to be valid.

Table 14 presents a summary of the data for the 16 MeV and 20 MeV nominal beam energies. These measurements indicate R_{so} shifts toward the phantom surface (i.e. a mean incident energy decrease) of up to 1.0 cm. These two beams apparently need an energy prediction model. As was previously discussed, the algorithm used in applying these models, in this case the mean incident energy model (equation 5), results in exact agreement with measured R_{so} values for the square custom inserts. As indicated in table 14, this is true for the 40 custom square insert combinations. For the 20 custom rectangular insert combinations, all the energy square root model's predictions agreed with measured values within the 0.2 cm criteria applicable for these beams (see table 12). Therefore, these data indicate that for the higher nominal beam energies, the application of the square root model to predict the mean incident energy (in terms of R_{so}) is valid.

5.3 Current Model Developments

Using the same theoretical bases as presented in Appendix I, McParland (5) proposed a more sophisticated method of generating a semiempirical expression to predict dose out

	Number	Cone Prediction		Square Root Model	
		Passed	Failed	Passed	Failed
Square Varian Inserts	12	12	0	12	0
Square Custom Inserts	40	24	16	40	0
Rectangular Custom Inserts	20	7	13	20	0
TOTAL	72	43	29	72	0

Maximum Variation From Measurements 1.0 cm

TABLE 14. Comparison of mean incident energy measurements and the quality of predictions. Pass / Fail Criteria: 0.2 cm variation from measurements (see Table 12).

put. This method was named the 2-D method of calculation. Though data presented indicated better predictive capabilities of this model, the increase in needed computing power for the curve fit routines and the recommendation to measure between 20 to 25 different fields per beam for accelerators which used the trimmer system described earlier has not lend itself to wide spread acceptance. Recently, McParland has proposed a different model for dose output prediction that incorporates the electron scatter off all collimation devices for a true irregular shaped field calculation (6). This latest formulation shows promise but is not as of yet in widespread use.

6.0 SUMMARY

Custom shaped electron beams are needed and used clinically. Data as to how these custom inserts used for beam shaping effect dose output and measured energy for Varian manufactured accelerators is relatively sparse. A method to predict any dose output and / or measured energy variation as opposed to dose output and energy measurement of each custom insert would be useful.

Relative output and mean incident energy (R_{50}) measurements were taken for a Varian Clinac 1800 capable of producing electron beams of 5 different nominal beam energies. Data for one hundred eighty different nominal beam energy / cone / insert combinations (30 Varian and 150 custom insert combinations) were acquired.

For relative output, no consistency in the data for all beams with the manufacturer supplied cones / inserts was observed. For custom square inserts within each individual cone, however, the data presented consistent behavior for all beams. Application of the square root model to relative output for each cone / insert / nominal beam energy combination gave good results for square custom inserts and rectangular inserts with a small length to width ratio. For the rectangular insert with a large length to width ratio, a positive bias of the predicted values for all nominal beam energies was apparent. A possible solution to this bias is using an alternate measurement technique to measure output

values for inserts smaller than 4x4 cm dimensions.

The data indicate no mean incident energy shift for the 6 MeV, 9 MeV, and 12 MeV nominal beam energies. An energy shift for the 16 MeV and 20 MeV beams for the 6x6 cone with Varian supplied inserts is mimicked by square custom inserts of the same dimensions for each individual cone. When needed, the square root model as it applies to mean incident energy prediction appears to be a valid predictive tool.

7.0 CONCLUSION

The goals of this study were to add to the database for Varian manufactured accelerators and investigate the possibility of applying the square root models for dose output and mean incident energy predictions. It is felt that both goals were meet.

Conclusions that can be derived from this study are as follows:

One, the data indicates that custom inserts do measureably affect the absorbed dose delivered relative to the Varian supplied insert for that cone.

Two, for the square custom inserts and rectangular inserts with a low length to width ratio, the relative output square root model perfomed adequately and would be of use as a predictive tool clinically.

Three, for rectangular inserts with a high length to width ratio, the relative output square root model's predictions varied significantly from measured data. More study is needed before the model should be applied clinically to this class of custom inserts.

Four, the data indicates that custom inserts affect the mean incident energy of the electron beam only in cases of the higher (i.e. 16 MeV and 20 MeV) energies.

Five, the application of the mean incident energy square root model to predict the R_{80} values for the 16 and 20 MeV beams was successful. For these energies, the application of this model would be of use clinically.

Appendix A

Reprint of

"Prediction of Electron Beam Output Factors"

by

Mills, M.D., Hogstrom, K.R., and Almond, P.R.

Prediction of electron beam output factors

Michael D. Mills, Kenneth R. Hogstrom, and Peter R. Almond

Department of Physics, The University of Texas System Cancer Center, M. D. Anderson Hospital and Tumor Institute, Texas Medical Center, Houston, Texas 77030

(Received 3 February 1981; accepted for publication 20 July 1981)

A method to predict square and rectangular field output factors from the measurement of selected fields of electron beams on the Therac 20 Saturne has been developed. A two parameter fit of the square field output factor data, based on the functional dependence as predicted by a pencil beam calculational model, has proven clinically acceptable. The pencil beam distributions are given by the Fermi–Eyges theory of multiple Coulomb scattering. For a rectangular field, the output factor can be calculated from the square root of the product of the two square field output factors with sides equal to those of the rectangular field. If however, there is a significant asymmetry between the X and Y collimator systems, then rectangular field output factors should be predicted from the product of the X and Y one-dimensional output factors. One-dimensional output factors are defined as output factors of rectangular fields where one side remains constant and equal to the side of the square reference field. Measured data indicate either of the two methods of determining rectangular field output factors to be clinically acceptable for the Therac 20, the use of one-dimensional output factors demonstrating greater accuracy. Data show agreement to within approximately 1.5% at electron energies of 6, 9, 13, and 17 MeV.

I. INTRODUCTION

The output factor for clinical radiotherapy beams is defined as the ratio of the maximum dose on central axis of the field of interest to that of a reference field size. The variation of output factor versus field size of therapeutic electron beams is substantially greater than that produced by high-energy photon beams. This is because changes in output are caused by the relative contribution of scattered radiation at the depth of maximum dose, d_{max}. For a photon beam, the dose can be divided into a primary and secondary (scattered) photon component. It is the secondary component that contributes to the variation in output factor. As this is much smaller than the primary photon component, a small dependence with respect to field size is expected. For electrons, essentially all of the dose at d_{max} is due to multiply scattered electrons so there is no primary component to the dose in the electron beam. Therefore we expect a strong field size dependence of the output factor at field sizes where there is more scattering out of a cylinder about central axis than scattering in the cylinder, i.e., scattering equilibrium does not exist. The variation in output is primarily due to electron scattering between the electron source and the patient, whereas the shape of the depth-dose curve will depend more on scattering after the secondary collimator. The amount of scattering, being field-size dependent, will be strongly influenced by the nature of the collimation system. This is explicit in the work of Biggs *et al.*,[1] Goede *et al.*,[2] and Choi *et al.*[3] for the Clinac 18 and Almond[4] and Almeida[5] for the Sagittaire. In the present work we will report only measurements made on the Therac 20 Saturne, which is similar in physical design to the Sagittaire.

The collimation system of the Therac 20 consists of interleaved photon collimators, which serve as primary collimators located approximately 28 and 25 cm from the source for the X and Y dimensions, respectively, and a set of secondary collimators or trimmers, which are located approximately 89 and 86 cm from the source, respectively. The two sets of collimators open and close in synchronized movement so that the field defined by the primary collimator always lies 5 cm outside the actual field size projected to the 100 cm source-to-skin distance (SSD). The continuous variation in field size permits innumerable rectangular field sizes for treatment. An efficient method for determination of output factors versus rectangular field size will be derived that may be applied either manually or using a computational device.

Traditionally the concept of equivalent squares has been applied to photon beams for the determination of field size effects on depth dose and output factor. Caution is advised in using this concept for electron beams as the equivalent square field size used to determine the output factor may differ from that used to determine the depth dose. Furthermore, theory shows that the equivalent square field size varies with depth for electron beams (Hogstrom *et al.*[6]). For the Therac 20, Hogstrom *et al.*[6] propose that depth dose for a rectangular field size be determined from the square root of the product of two square field depth doses where the sides of the two square fields are equal to the two sides of the rectangular field. Referred to as the square root method, this concept has been applied to the determination of output factors in the present work.

II. THEORY

The electron beam of the Therac 20 linear accelerator is produced from a beam of electrons that exits the accelerating tube through an aluminum end window (0.2 mm thickness) and which is spread into a broad beam by a scanning quadrupole magnet. The beam is collimated by primary and secondary collimators before impinging on the phantom surface.

 0094-2405/82/010060-09$01.20

As the collimators are opened and closed, the output factor varies considerably, the variation being most significant for the lower energy electrons. In order to quantify this variation the output factor is assumed to be proportional to the electron flux on the central axis at d_{max}. Electron multiple Coulomb scattering (MCS) that arises between the source and the phantom surface, and to a lesser extent from scattering that takes place in the phantom, determines the electron flux at the position of maximum dose.

The electron flux at d_{max} can be calculated by propagating the electron flux from the source to the primary collimators, then from the primary collimator to the secondary collimator, and finally from the secondary collimator to d_{max}. The propagation of electron flux from one transverse plane to the next, assumes the beam at the initial plane to be composed of a collection of pencil beams. A pencil beam is defined as those electrons passing through an imaginary, infinitesimal, rectangular slit, δX by δY, at a particular location in the plane. The lateral spreading of that pencil beam is calculated according to the Fermi–Eyges[7] theory of MCS. The collimators are assumed "perfect" so that we treat them as infinitely thin and located at the proximal surface of the actual collimator. Such a treatment ignores scattering off the walls of the collimators, whose consequences will be discussed later.

Diagrammed in Fig. 1, the beam of monoenergetic electrons exits the vacuum of the accelerator, passing through a thin exit window, a beam-spreading device such as a scanning magnetic field or a scattering foil, and air prior to reaching the primary collimator. For the case of the scanning magnet, a saw-toothed time variation in the transverse magnetic field generates a uniform, time-averaged flux across the aperture of the primary collimator. The flux at the primary collimator is uniform and field size independent. The flux is then propagated to the secondary collimator by treating the beam at the plane of the primary collimator as a collection of pencil beams.

At the level of the secondary collimator, the flux distribution of those pencil beams, originating at the level of the primary collimator (Z_1), can be calculated using the Fermi–Eyges theory. If all electrons passing through the infinitesimal area δX by δY at X', Y' were parallel and approximately normal to the plane at Z_1, then the flux distribution at Z_2 would be Gaussian and given by

$$F(X, Y, Z_2) = \frac{1}{2\pi\sigma_p^2} \exp\left[- \frac{(X-X')^2 + (Y-Y')^2}{2\sigma_p^2} \right], \quad (1)$$

where σ_p is the sigma of the projected Gaussian distribution at Z_2 given by

$$\sigma_p^2 = \sigma_s^2 = \int_{z_1}^{z_2} (Z_2 - Z)^2 \left(\frac{d\sigma_{MCS}^2}{dZ} \right) dZ, \quad (2)$$

where $\frac{d\sigma_{MCS}^2}{dZ}$ is the linear angular scattering power evaluated at the mean electron energy at Z and for the material type located at Z, in this case air. Z_1 and Z_2 are the locations of the primary and secondary collimators, respectively. Because there is scattering prior to the primary collimator, the electrons passing through the infinitesimal area δX by δY will not be parallel, but have a Gaussian spread about their mean direction. This spreading of the pencil beam is added rms (root mean square) to that predicted in its absence, resulting in a new sigma

$$\sigma_p^2 = \sigma_s^2 + \sigma_{\theta_s}^2 (Z_2 - Z_1)^2, \quad (3)$$

where σ_{θ_s} is the sigma of the distribution of the projected angle of rays in the pencil beam. This angular sigma is due to the MCS above the primary collimator produced by the beam spreading device and all other intervening matter between it and the primary collimator. Its functional dependence is the same as that in an earlier paper by Hogstrom *et al.* [6] and is given by

$$\sigma_{\theta_s}^2 = \langle (\theta_s - \bar{\theta}_s)^2 \rangle = a_0 - a_1^2/a_2, \quad (4A)$$

where $\bar{\theta}_s$ is the mean direction of the pencil beam at the level of the primary collimator, and where a_i is the ith moment of the linear angular scattering power given by Eyges,[7]

$$a_i = \int_0^{z_1} (Z_1 - Z)^i \left(\frac{d\sigma_{MCS}^2}{dZ} \right) dZ. \quad (4B)$$

In calculating the flux distribution at the level of the secondary collimator, the contribution from all pencil beams passing through the aperture of the primary collimator are summed. Making the small angle approximations, the theory reduces to that of a parallel pencil beam in which the primary collimator size is projected to the plane of calculation and the flux of each pencil beam is corrected for inverse square fall-off. The result is the relation

$$\Phi_2(X, Y, Z_2) \propto \frac{1}{Z_2^2} \int_{-\left(\frac{WXP}{2} + \Delta W\right)}^{+\left(\frac{WXP}{2} + \Delta W\right)} dX' \int_{-\left(\frac{WYP}{2} + \Delta W\right)}^{+\left(\frac{WYP}{2} + \Delta W\right)} dY' \frac{1}{2\pi\sigma_p^2} \exp\left[- \frac{(X-X')^2 + (Y-Y')^2}{2\sigma_p^2} \right], \quad (5)$$

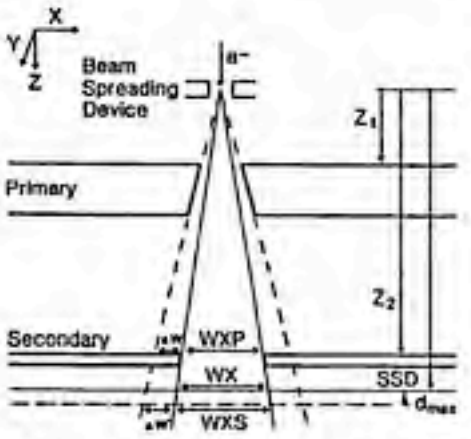

FIG. 1. Schematic of the variable collimation system of the Therac 20 Saturne.

where WXP, WYP is the width of the X, Y collimator projected to the position of the secondary collimator for a field size WX, WY at the SSD. ΔW is the margin that the field defined by the primary collimator lies outside the secondary collimator at the level of the secondary collimator. This margin is necessary so that the flux incident at the level of the secondary collimator will be nearly uniform across its aperature (Brahme[9]). Equation (5) reduces to

$$\Phi_s(X, Y, Z_2) \propto \frac{1}{Z_2^2}\left\{ERF\left[\frac{\frac{WXP}{2}+\Delta W-X}{\sqrt{2}\sigma_p}\right]+ERF\left[\frac{\frac{WXP}{2}+\Delta W+X}{\sqrt{2}\sigma_p}\right]\right\} \times\left\{ERF\left[\frac{\frac{WYP}{2}+\Delta W-Y}{\sqrt{2}\sigma_p}\right]+ERF\left[\frac{\frac{WYP}{2}+\Delta W+Y}{\sqrt{2}\sigma_p}\right]\right\}, \quad (6)$$

where ERF is the standard error function.[8]

The propagation of this flux to d_{max} has been previously discussed (Hogstrom *et al.*[4]). The flux at d_{max} is the sum of the fluxes of individual pencil beams originating at the plane of the secondary collimator, the contribution of each pencil beam being weighted by its relative strength $\Phi_s(X, Y, Z_2)$. For a rectangular collimator, this results in the flux on central axis being

$$\Phi(0, 0, d_{max}) \propto \left(\frac{Z_2}{SSD+d_{max}}\right)^2 \int_{\frac{-WXS}{2}}^{\frac{+WXS}{2}} dX' \int_{\frac{-WXS}{2}}^{\frac{+WXS}{2}} dY' \Phi_s(X', Y', Z_2) \frac{1}{2\pi\sigma_s^2} \exp\left[\frac{-(X'^2+Y'^2)}{2\sigma_s^2}\right]. \quad (7)$$

where WXS, WYS are the field sizes of the secondary collimator projected to the depth of d_{max}, and σ_s is the sigma of the projected Gaussian distribution. σ_s is determined by an expression similar to Eq. (3) for σ_p,

$$\sigma_s^2 = \tfrac{1}{2}\int_{Z_1}^{SSD+d_{max}} (SSD+d_{max}-Z)^2 \frac{d\sigma_{MCS}^2}{dZ} dZ + (A_0 - A_1^2/A_2)\,(SSD+d_{max}-Z_1)^2, \quad (8A)$$

where the scattering powers are given by

$$A_i = \tfrac{1}{2}\int_0^{Z_2} (Z_2 - Z)^i \left(\frac{d\sigma_{MCS}^2}{dZ}\right) dZ. \quad (8B)$$

As previously discussed, the flux incident at the level of the secondary collimator within its aperture is nearly uniform so that the approximation $\Phi_s(X, Y, Z_2) = \Phi_s(0, 0, Z_2)$ can be made. This allows the integral in Eq. (7) to be evaluated analytically, reducing to

$$\Phi(0, 0, d_{max}) \propto \frac{1}{(SSD+d_{max})^2}\left\{ERF\left[\frac{\frac{WXP}{2}+\Delta W}{\sqrt{2}\sigma_p}\right] ERF\left[\frac{\frac{WYP}{2}+\Delta W}{\sqrt{2}\sigma_p}\right]\right\}\left\{ERF\left[\frac{WXS}{2\sqrt{2}\sigma_s}\right] ERF\left[\frac{WYS}{2\sqrt{2}\sigma_s}\right]\right\}. \quad (9)$$

It is not unusual for the shape of the depth dose curve to vary with field size, particularly at the higher electron energy beams. Physically, this occurs when the field size becomes small relative to the sigma of the pencil beams originating from the plane of the secondary collimator. This causes a decrease in the flux on central axis as fewer electrons scatter into a small volume along central axis. Occasionally, the change in the shape of the depth-dose curve will be enough so that d_{max} will shift proximally for the smaller field sizes. Then the dose peak will occur before maximum buildup of delta rays can occur, and a correction factor should be applied to the flux in Eq. (9) of the form

$$CF = \left[\frac{D_0^{WXO}(0, 0, d_{max}^{WX, WY})}{D_0^{WXO}(0, 0, d_{max}^{WXO})}\right] \times \left[\frac{ERF\left(\frac{WXOS}{2\sqrt{2}\,\sigma_0(d_{max}^{WX, WY})}\right)^{-2}}{ERF\left(\frac{WXOS}{2\sqrt{2}\,\sigma_0(d_{max}^{WXO})}\right)^{-2}}\right] \times \left[\frac{(SSDO+d_{max}^{WX, WY})^2}{(SSDO+d_{max}^{WXO})^2}\right], \quad (10)$$

where D_0^{WXO} is the central axis depth dose for the standard reference square field with a side width WXO; σ_0 is the σ_s for the reference field; $SSDO$ is the source to skin distance of the reference field; and d_{max}^{WXO} is the depth of maximum dose for the reference field. The difference in the percentage depth dose at any depth depends on delta ray buildup, inverse square fall off, and side scatter equilibrium. Therefore the

effect of delta ray buildup can be calculated from the percentage depth dose at the depth $d_{max}^{WX,WY}$ [first ratio of Eq. (10)] by removing the inverse square dependence (third ratio) and the dependence on side scatter (second ratio). Physically, the correction factor of Eq. (10) is simply the depth-dose factor of an infinitely broad parallel electron beam at depth $d_{max}^{WX,WY}$. The basis for writing this equation is discussed in greater length in papers by Hogstrom *et al.*[8] and Werner *et al.*[10] Applying the correction factor to Eq. (9) and assuming that dose is proportional to the electron flux, the maximum dose becomes

$$D_{max}^{WX,WY}(0,0,d_{max}^{WX,WY}) \propto \left(\frac{1}{SSD + d_{max}^{WX,WY}}\right)^2 \left\{ERF\left[\frac{WXP}{2} + \Delta W}{\sqrt{2}\sigma_p}\right] ERF\left[\frac{\frac{WYP}{2} + \Delta W}{\sqrt{2}\sigma_p}\right]\right\} \times \left\{ERF\left[\frac{WXS}{2\sqrt{2}\sigma_s}\right] ERF\left[\frac{WYS}{2\sqrt{2}\sigma_s}\right]\right\} \times \left\{D_0^{WXO}(0,0,d_{max}^{WX,WY}) \left[ERF\left(\frac{WXOS}{2\sqrt{2}\,\sigma_0(d_{max}^{WX,WY})}\right)\right]^{-2} (SSDO + d_{max}^{WX,WY})^2\right\}. \quad (11)$$

where the denominator of Eq. (10) is excluded as it is absorbed in the constant of proportionality. The first term is the traditional inverse-square factor, the second term is the influence of the primary collimator on scattering equilibrium along the central axis, the third term is the influence of the secondary collimator on scattering equilibrium along the central axis, and the final term is the influence of d_{max} shifting, causing a change in delta ray build-up. Irregular collimation would be handled by replacing the third term in Eq. (11) with that evaluated for an irregular shaped collimator.

The dependence of D_{max} is most influenced by the primary collimator and can be demonstrated by calculating the terms of Eq. (11) for most clinical collimation situations. This has been qualitatively demonstrated in the measurements of Biggs *et al.*[1] (1979) on a Clinac 18 linear accelerator. They showed that the dose output for square fields, for the case in which the primary collimator varies and the secondary collimator is fixed, is similar in field-size dependence to the case in which both collimators vary with the primary collimator always set 5 cm larger than the secondary collimator. The similarity is most obvious at the lower electron energies 4, 6, and 9 MeV. The data of Goede *et al.*[2] also support the hypothesis. Their data at 9 MeV on the Clinac 18 showed that variation of the output for a fixed primary collimator with a variable secondary collimator yields an almost constant output except for very small field sizes ($< 5 \times 5$ cm). Side scatter from the walls of the cones of the Clinac 18 is important, and as the present model completely ignores collimator scatter, it would be difficult to fit Eq. (11) to Clinac 18 data, especially at the higher energies [> 10 MeV] where the shape of the cone-ratio curve clearly has a peak that cannot be accounted for by the present theory. The field-size dependence of output factors on the Sagittaire linear accelerator (Almond,[4] Almeida[5]) and the Therac 20 Saturne linear accelerator better follows the shapes predicted by Eq. (11) as the collimation system is more accurately described by the idealized derivation reported here.

Our goal is to produce some practical methods of determining output factors for rectangular fields. Using Eq. (11), and assuming *SSD* for the reference field to be the same as *SSD* of the fields, the output factor is

$$OF^{WX,WY} = \left\{\frac{\left[ERF\left(\frac{WXP/2 + \Delta W}{\sqrt{2}\sigma_p}\right) ERF\left(\frac{WYP/2 + \Delta W}{\sqrt{2}\sigma_p}\right)\right]}{\left[ERF\left(\frac{WXOP/2 + \Delta W}{\sqrt{2}\sigma_p}\right)\right]^2}\right\} \times \left\{\frac{\left[ERF\left(\frac{WXS}{2\sqrt{2}\sigma_s(d_{max}^{WX,WY})}\right) ERF\left(\frac{WYS}{2\sqrt{2}\sigma_s(d_{max}^{WX,WY})}\right)\right]}{\left[ERF\left(\frac{WXOS}{2\sqrt{2}\sigma_s(d_{max}^{WX,WY})}\right)\right]^2}\right\} \times D_0^{WXO}(0,0,d_{max}^{WX,WY}), \quad (12)$$

where it is recognized that

$$D_0^{WXO}(0,0,d_{max}^{WXO,WYO}) = 100\%.$$

For energies where d_{max} remains constant, the output factor reduces to

$$OF^{WX,WY} = \left\{\frac{\left[ERF\frac{WXP/2 + \Delta W}{\sqrt{2}\sigma_p} ERF\frac{WYP/2 + \Delta W}{\sqrt{2}\sigma_p}\right]}{\left[ERF\left(\frac{WXOP/2 + \Delta W}{\sqrt{2}\sigma_p}\right)\right]^2}\right\} \times \frac{\left[ERF\left(\frac{WXS}{2\sqrt{2}\sigma_s}\right) ERF\left(\frac{WYS}{2\sqrt{2}\sigma_s}\right)\right]}{\left[ERF\left(\frac{WXOS}{2\sqrt{2}\sigma_s}\right)\right]^2}. \quad (13)$$

This expression should also approximate energies where d_{max} shifts, since in those cases D_0 is relatively uniform. To simplify Eq. (13) even more, the secondary collimation can be ignored, in which case

$$OF^{WX,WY} = \frac{\left[ERF\left(\frac{WXS/2+\Delta W'}{\sqrt{2}\sigma'_p}\right)ERF\left(\frac{WYS/2+\Delta W'}{\sqrt{2}\sigma'_p}\right)\right]}{\left[ERF\left(\frac{WXOS/2+\Delta W'}{\sqrt{2}\sigma'_p}\right)\right]^2}. \quad (14)$$

where we replace σ_p with σ'_p which corresponds to now integrating from the location of the primary collimator to the location of d_{max} in Eq. (2).

From Eqs. (13) or (14) it can be shown for rectangular collimation that

$$OF^{WX,WY} = \sqrt{OF^{WX,WX}.OF^{WY,WY}}. \quad (15)$$

Although scattering off the collimators has been neglected, this will have some effect so that neither Eqs. (12), (13), nor (14) might accurately predict the output factor versus field size. However, the output factor predicted by Eq. (15) is now related back to measured data, which should help in partially correcting for that simplification.

In some instances the X and Y collimation systems may slightly differ from one another causing different sigmas between X and Y. In these cases, Eq. (15) may not be clinically acceptable. However, it can be shown from Eqs. (13) or (14) that

$$OF^{WX,WY} = OF^{WX,W10}.OF^{W10,WY}. \quad (16)$$

Equation (15) requires only a curve of output factors versus square-field sizes, whereas Eq. (16) requires two curves, both X and Y one-dimensional output factors. One-dimensional output factors are defined for fields in which one side is the same as the standard field width while the other varies.

Both Eqs. (15) and (16) can be derived assuming rectangular symmetry and that the functional dependence of the flux can be separated into factors depending only on X and Y, respectively. The separable nature of the function is a direct result of the small angle approximations in the theory of MCS. Therefore, one should not expect these formulas to hold for photon beams where the field size dependence of the output factor arises primarily from large angle Compton scattering.

III. METHODS OF MEASUREMENT

A number of square-field and rectangular-field measurements for electron beam output factors on the Therac 20 were carried out at the 6, 9, 13, and 17 MeV energies using a PTW 0.1 cc ionization chamber, internal diameter 3.4 mm. For the energies where d_{max} varied, namely 13 and 17 MeV, the location of d_{max} was determined from ionization measurement about d_{max} in a water phantom. The dose output was then measured at the d_{max} for the particular field size. The output factor was calculated by normalizing each measured output to the measured output at d_{max} for a 10×10 cm² field. For repeat measurements at 13 and 17 MeV, and for energies where d_{max} did not significantly vary, namely 6 and 9 MeV, the measurements were made in a polystyrene phantom. Stem effect was normalized to 1.00 for a 10×10 cm² field, and corrections were necessary for the smaller field sizes.

Effects which must be considered when using an ion chamber for small field electron beams are:

(a) the chamber demonstrates a stem effect of +1% correction for the 5×5 cm² field and +2% for the 4×4 cm² field;

(b) with small fields, there may be a variation in dose across the active volume of the chamber (not accounted for in the present data);

(c) d_{max} shifts toward the surface for the smaller fields at higher energies.

The theory indicates that geometrical differences between the two orthogonal collimation systems may lead to variation in how a specific field width or length contributes to the dose measured along the central axis. If this is true, then each collimator should be varied independently to give a one-dimensional output factor. In this case, the collimator in the nonvarying dimension was placed at the 10 cm position. According to Eq. (16), the product of the measured X×10 and 10×Y output factors yields the $X \times Y$ output factor calculated by this one-dimensional method. This technique has the following advantages:

(a) the stem effect is eliminated, as the long axis of the chamber can be placed along the axis of the standard dimension.

(b) for small fields, the variation in dose across the active volume is minimized since orientation of the chamber according to advantage (a) leaves the shortest dimension of the chamber along the axis with minimum dose variation.

(c) the different contributions of each collimator axis to the output factor can be accounted for since measurements in both the x and y dimensions are performed.

Lithium fluoride thermoluminescent dosimetry (LiF TLD) measurements were performed at d_{max} for small field sizes to compare to each of the two ion chamber techniques for producing output factor values. The powder system used has a dose precision of about 2%. Therefore, in the calculation of the output factor, the output of the field size of interest contributes a 2% random error and the standard field size to which each output is normalized contributes a 2% systematic error, resulting in a net standard error of 3% for any single output factor.

IV. RESULTS

Table I compares small square-field output factors determined three separate ways; (1) using the ionization chamber and correcting for stem effect, (2) using the ionization chamber but making the calculations by the one-dimensional output factor technique [Eq. (15)] $OF^{4\times4} = OF^{4\times10}\times OF^{10\times4}$, e.g., and (3) using TLD. The results of all methods of measurement are in agreement within the accuracy of the measuring technique. However, the 4×4 cm² field measure-

TABLE I. Comparison of small field output factors measured by different techniques.

Field size	4×4	5×5	6×6
	6 MeV		
Measurements			
Ion chamber	0.762	0.843	0.886
Calculated			
1-D method	0.769	0.837	0.882
Measurements TLD	0.786	0.847	0.900
	9 MeV		
Measurements			
Ion chamber	0.859	0.922	0.948
Calculated			
1-D method	0.871	0.917	0.950
Measurements TLD	0.893	0.913	0.947
	13 MeV		
Measurements			
Ion chamber	0.871	0.936	0.955
Calculated			
1-D method	0.887	0.924	0.953
Measurements TLD	0.907	0.937	0.961
	17 MeV		
Measurements			
Ion chamber	0.960	0.966	0.980
Calculated			
1-D method	0.967	0.980	0.991
Measurements TLD	0.961	0.962	0.985

ments show that the conventional ion chamber technique yields values systematically less than the one-dimensional derived values. This effect can be accounted for by considering the small variation in dose across the active volume of the ion chamber as the active volume reaches the edges of the penumbra of the beam.

Square-field output factors at 9 MeV have been plotted as a function of side of field in Fig. 2. One-dimensional output factors at 9 MeV have been plotted in Fig. 3. The variation between the results in the X and Y dimensions are indicative of the fact that the interleaved collimation on the Therac 20

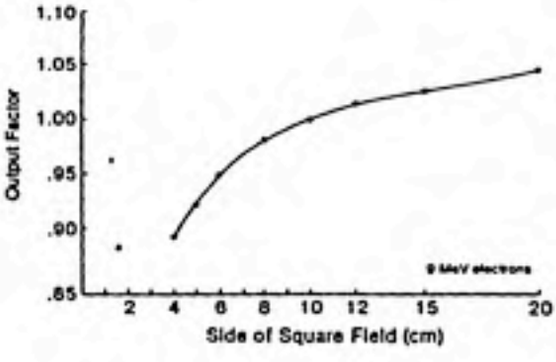

FIG. 2. Output Factors for 9 MeV electrons as a function of side of square field. All measurements were made using corrected ion chamber readings except for the 4×4 cm² field, which was measured with TLD.

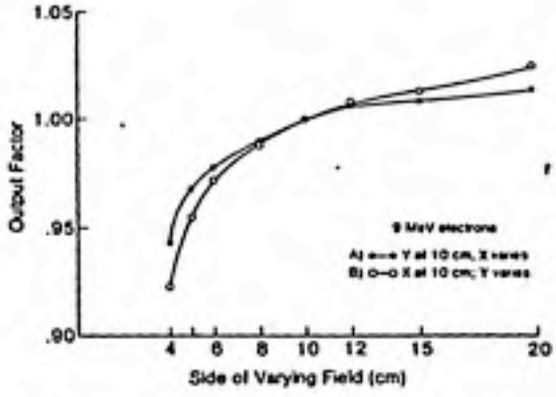

FIG. 3. One-dimensional output factors for 9 MeV electrons. The Y dimension was held constant at 10 cm and the X-setting allowed to vary in Graph A. This was reversed in Graph B. The chamber was placed along the 10 cm axis for all measurements.

TABLE II. Comparison of predicted output factors using 1-D and square root techniques measured at 9 MeV.

Field size ($X \times Y$ cm^2)	Measurements Ion chamber	Calculated $\sqrt{\ }$ method	Calculated 1-D method
4×4	0.893[a]	–	0.870
5×5	0.922[b]	–	0.924
6×6	0.950	–	0.951
8×8	0.982	–	0.978
10×10	1.000	–	1.000
12×12	1.015	–	1.014
15×15	1.027	–	1.021
20×20	1.047	–	1.039
(Chamber along Y axis)			
5×7	0.932	0.945	0.951
5×10	0.968	0.960	0.968
5×15	0.984	0.973	0.981
5×20	0.993	0.983	0.992
7×10	0.988	0.969	0.985
7×15	1.000	0.998	0.998
7×20	1.013	1.007	1.010
10×15	1.013	1.013	1.013
10×20	1.025	1.023	1.025
(Chamber along 10 cm axis)			
4×10	0.943	0.945	–
5×10	0.968	0.960	–
6×10	0.978	0.975	–
8×10	0.990	0.991	–
12×10	1.006	1.007	–
15×10	1.008	1.013	–
20×10	1.014	1.023	–
10×4	0.923	0.945	–
10×5	0.955	0.960	–
10×6	0.972	0.975	–
10×8	0.988	0.991	–
10×12	1.008	1.007	–
10×15	1.013	1.013	–
10×20	1.025	1.023	–

[a]TLD.
[b]Corrected for stem effect.

cause the X and Y collimator geometry to be different. The Y collimator is physically 3 cm closer to the source leading to a greater σ_p in that dimension, hence giving the observed difference. Table II shows the results of ion chamber measurements performed at 9 MeV for square and rectangular fields. The 4×4 cm^2 field was measured using TLD and the 5×5 cm^2 field was corrected for stem effect. Chamber placement was as indicated: along the y-axis for rectangular fields, along the 10-cm-axis for fields used to generate the one-dimensional output factors. Figures 2 and 3 were used to generate output factors in columns 3 and 4 of Table II using Eqs. (15) and (16), respectively.

The measured output factors of rectangular fields show a better correlation with the calculations by the one-dimensional method than with those of the square root method. This is to be expected as the former method accounts for the difference in scatter between the X and Y collimators, while the square root technique does not.

V. DISCUSSION

The ability of the theory to predict square-field output factors is important in that it tests the accuracy of the assumptions in generating the theory, as well as evaluating the ability to describe the parameters of the field-size dependence for computational use. The output factors of rectangular fields may by calculated using either Eq. (12), (13), or (14). Calculations of the output factors based solely on the theory were typically found to significantly underestimate the measured values at large field sizes due to the model ignoring collimator scattering. Equation (14) was found to better predict the measured data than Eq. (13), although the reason for this is not appreciated. For small field sizes the theory typically overestimates the output factor again probably due to the absence of collimator scattering in the model. In this case, Eq. (13) was found to better predict the measured data than Eq. (14), especially at higher energies. This is because of the importance of the secondary collimator term at the higher energies due to d_{max} being deeper, and because of the assumption of a uniform flux being incident on the secondary collimator at the lower energies. Neither equation adequately calculated the measured square-field output factors, although the predicted curves had the same characteristic

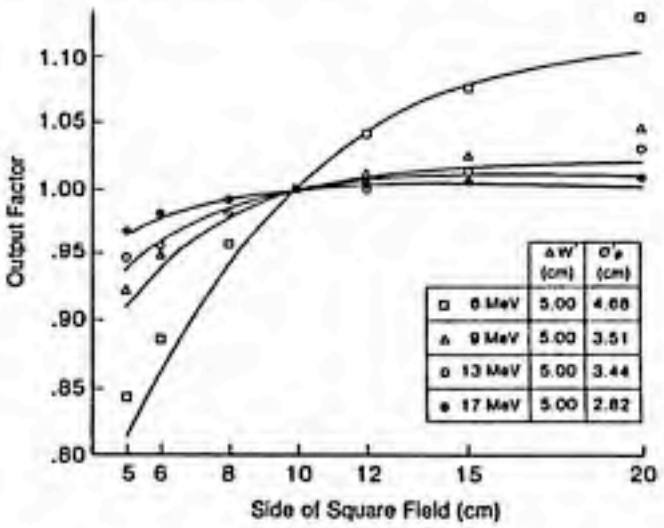

FIG. 4. Fitting of output factor data. $\Delta W'$ was required to be 5.0 cm, its physical value. The resulting σ'_p is computer-generated to give the best curve fit to the data.

shape. Therefore, it was decided to use Eq. (14) and allow the parameters to vary in order to fit the data.

In the first case, $\Delta W'$ of Eq. (14) was taken to be its physical value of 5.0 cm. σ'_p was then varied to fit the experimental data by the least squares method. The resulting fits are compared to the measured values in Fig. 4. The resulting sigmas are 4.68, 3.51, 3.44, and 2.82 cm for the 6, 9, 13, and 17 MeV electron beams, respectively. These values are compared to the corresponding theoretical values of 4.62, 3.29, 2.42, and 1.94 cm [Eq. (3)]. The disagreement in the sigmas is largest at the higher energies and largest field sizes, which is consistent with what would be expected because of collimator scattering. Considering only collimator scattering, the output factor should increase proportionally to the side of the square field for larger field sizes as the exposed area of the photon collimation jaws increases proportionally. This is qualitatively observed as the output factor predicted by Eq. (14) asymptotically approaches a constant value and consistently underestimates the output factor at the largest field sizes.

Nonetheless, the form of Eq. (14) seemed appropriate, so that both parameters $\Delta W'$ and σ'_p were allowed to vary in fitting the data. The results, shown in Fig. 5, show the data and the calculations to lie within approximately 0.5% of one another. This suggests that the field-size dependence for the output factor may be determined by Eq. (14) provided the user fits the data by varying $\Delta W'$ and σ'_p. The nonphysical values of $\Delta W'$ and σ'_p are a result of chi-square varying slowly with changes in the parameters and the fact that both parameters increase in unison in minimizing chi-square. The two-parameter search is simple enough to do on a hand calculator using a table of the error function or an approximation [Drenick[11]]. It is also possible to fit the "one-dimensional" output factors by varying $\Delta W'$ and σ'_p. For machines other than the Therac 20, these fitting methods may not be applicable.

Once the square-field or one-dimensional factors have been determined, the rectangular-field output factors can be determined using Eq. (15) or (16), respectively. Both methods are clinically acceptable in the present case, the latter being most accurate. We expect this approach may be useful with other therapeutic electron beams having a similar collimation system. If Eq. (14) will not fit the data, as will be the case for the Clinac 18, then smoothed curves drawn through the data might be used in calculating the output factors of rectangular fields. As collimator scatter is neglected in this model, the applicability of Eq. (15) or (16) to those machines where collimator scatter is important has yet to be tested.

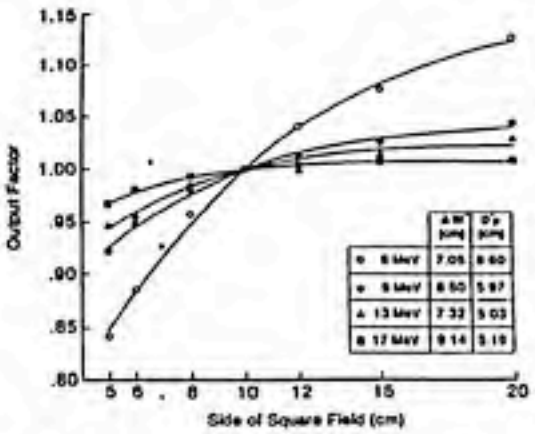

FIG. 5. Fitting of output factor data. $\Delta W'$ and σ'_p were allowed to vary until the best computer generated fit to the data was obtained.

VI. SUMMARY

A simple approach to the prediction of output factors versus field size for electron beams on the Therac 20 linear accelerator has been given. We have derived equations based

on the Fermi–Eyges theory of multiple Coulomb scattering. The resulting equations do not predict the measured data, most likely because the effect of collimator scattering was neglected. However, their functional dependence is useful, and by variation of the parameters the square field data can be fitted. Equations relating rectangular-field output factors to measured square field or one-dimensional output factors have proven clinically acceptable for the Therac 20.

In summary we recommend the following as a practical approach for the determination of rectangular-field output factors on the Therac 20:

1. Measure square field or one-dimensional output factors using methods previously described.

2. Either graph or fit the data using Eq. (14) so that square field or one-dimensional output factors may be extracted for any field size.

3. Calculate the output factor for the rectangular field of interest using Eq. (15) or (16), whichever is appropriate.

4. Verify the process by making measurements at a few of the rectangular field sizes.

ACKNOWLEDGMENTS

We wish to thank Jack Cundiff for his support in the performance of the ion chamber and TLD dosimetry. We are indebted to John Ames and William Simon for engineering maintenance of the Therac 20 during the course of this investigation.

This work was supported in part by Research Grant CA–06294 from the National Cancer Institute.

[1] P. J. Biggs, A. L. Boyer, and K. P. Doppke, Int. J. Radiat. Onc. Biol. Phys. 5, 433 (1979).
[2] M. R. Goode, D. S. Gooden, R. S. Ellis, T. J. Brickner, Jr., Int. J. Radiat. Onc. Biol. Phys. 2, 791 (1977).
[3] M. C. Choi, J. A. Purdy, B. Gerbi, F. G. Abrath, and G. P. Glasgow, Med. Phys. 6, 137 (1979).
[4] P. R. Almond, in *Clinical Applications of the Electron Beam*, edited by N. du V. Tapley (Wiley, New York, 1976), p. 7–80.
[5] C. E. V. de Almeida, M. S. Thesis, University of Texas at Houston Graduate School of Biomedical Sciences, Houston, Texas (1973).
[6] K. R. Hogstrom, M. D. Mills, and P. R. Almond, Phys. Med. Biol. 26, 445 (1981).
[7] L. Eyges, Phys. Rev. 74, 1534 (1948).
[8] $ERF[X] = \frac{2}{\sqrt{\pi}} \int_0^X e^{-t^2} dt$
[9] A. Brahme, presented at The 14th International Congress of Radiology, Rio de Janeiro, Brazil (1977).
[10] B. L. Werner, F. M. Khan, and F. C. Deibel, Med. Phys. (to be published).
[11] *Computer Approximations*, edited by R. F. Dremick, H. Hochstadt, and D. Gillette (Wiley, New York, 1968), p. 136.

Appendix B

Reprint of

"Electron Beam Dose Calculations"

by

Hogstrom, K.R., Mills, M.D., and Almond, P.R.

Phys. Med. Biol., 1981, Vol. 26, No. 3, 445–459. Printed in Great Britain

Electron beam dose calculations

Kenneth R Hogstrom, Michael D Mills and Peter R Almond

Department of Physics, The University of Texas System Cancer Center, MD Anderson Hospital and Tumor Institute, Texas Medical Center, Houston, TX 77030, USA

Received 5 September 1980

Abstract. Electron beam dose distributions in the presence of inhomogeneous tissue are calculated by an algorithm that sums the dose distribution of individual pencil beams. The off-axis dependence of the pencil beam dose distribution is described by the Fermi-Eyges theory of thick-target multiple Coulomb scattering. Measured square-field depth-dose data serve as input for the calculations. Air gap corrections are incorporated and use data from 'in-air' measurements in the penumbra of the beam. The effective depth, used to evaluate depth-dose, and the sigma of the off-axis Gaussian spread against depth are calculated by recursion relations from a CT data matrix for the material underlying individual pencil beams. The correlation of CT number with relative linear stopping power and relative linear scattering power for various tissues is shown. The results of calculations are verified by comparison with measurements in a 17 MeV electron beam from the Therac 20 linear accelerator. Calculated isodose lines agree nominally to within 2 mm of measurements in a water phantom. Similar agreement is observed in cork slabs simulating lung. Calculations beneath a bone substitute illustrate a weakness in the calculation. Finally a case of carcinoma in the maxillary antrum is studied. The theory suggests an alternative method for the calculation of depth-dose of rectangular fields.

1. Introduction

Radiation therapy with electron beams has been useful because of the properties of its physical dose distribution: (i) the dose is relatively uniform from the surface to a given depth; (ii) the depth of penetration can be controlled by varying the incident beam energy and by using tissue compensators; and (iii) the mass stopping power of electrons does not vary significantly for normal tissues (Zatz *et al* 1961). These allow single-port irradiations, which may be aimed directly at critical organs and structures, provided the depth of penetration is properly controlled to stop short of that area. Algorithms for electron beam dose calculations that are accurate for inhomogeneous tissue are required in order that treatment planning may be of maximum patient benefit. An accurate description of the patient anatomy, upon which such an algorithm depends, has been difficult or impossible to obtain until the recent advent of computerised tomography (CT). It is the purpose of this work to develop a computer algorithm for the calculation of electron beam dose distributions in patients in the presence of inhomogeneous tissue by making use of CT data.

Innumerable papers related to electron beam dose calculations are available, and excellent reviews of such works have been written (Sternick 1978, Nusslin 1979). A careful review of these works has led to the conclusion that a pencil beam calculation algorithm would be the most practical. Lillicrap *et al* (1975) have demonstrated that measured pencil beam dose distributions can be summed to predict broad beam

0031-9155/81/030445+15 $1.50

distributions accurately. However, in heterogeneous tissue it is impractical to measure all the pencil beams that are required.

We have independently developed an algorithm similar to that reported by Perry and Holt (1980). This algorithm calculates dose by summing pencil beam dose distributions, which are calculated as if the inhomogeneity structures underlying the central ray of a pencil beam are infinite in their lateral extent. Our methods complement those of Perry and Holt (1980) in that the scattering theory presented explicitly deals with: (i) the continuous variation of material type in patient tissue that is required when using CT data; (ii) the continuous energy loss of electrons through the media; and (iii) the simultaneous calculation of beam penumbra and inhomogeneity scatter effects. In particular, we discuss the incorporation of CT data into the algorithm, which includes both recursion relations for increasing the efficiency of computer run time and the correlation of CT number to physical parameters required by the algorithm.

We will discuss the derivation of the algorithm based on the Fermi–Eyges theory of multiple Coulomb scattering (Eyges 1948), the dosimetry required as input into the calculation, and the use of CT data in describing inhomogeneous tissue. In addition we will look at the results in a variety of ways in order to emphasise various applications of the algorithm, such as prediction of depth-dose for rectangular field sizes and calculation of irregular-field dose distributions. Finally, we will compare calculation with measurements in order to evaluate adequately the strengths and limitations of the algorithm.

2. Theory

2.1. General considerations

The success of multiple Coulomb scattering theory applied to charged particle therapy beams in the prediction of the penumbra in homogeneous water phantoms (Hogstrom *et al* 1980) and the dose distributions distal to thin inhomogeneities (Goitein 1978, Goitein *et al* 1978) has made this approach attractive. Goitein and Sisterson (1978) resorted to a Monte Carlo calculation for the more general case involving thick inhomogeneities to account for: (i) significant energy loss of the particle traversing the inhomogeneity; (ii) the lateral displacements of the particles in traversing the thick slabs of matter; and (iii) the particle escaping the thick inhomogeneity at its lateral border. The impracticability of using Monte Carlo calculations for routine treatment planning algorithms has encouraged the development of the present analytical method. Only the latter effect will not be adequately accounted for by the algorithm.

Ideally, a general purpose algorithm such as ours will be most effective if the calculation uses measured data for input and manipulates that data according to the physics involved. The algorithm accounts for multiple Coulomb scattering by using the Fermi–Eyges theory (Eyges 1948). The angular spread of the electron–electron Möller scattering component is approximated according to Williams (1940) by replacing Z^2 with $Z(Z+1)$. On the other hand, the resulting energy loss and production of secondary electrons due to Möller scattering, which changes the shape of the scatter distribution in thick targets, is ignored. The effect of Möller scattering on the depth–dose is accounted for by using measured depth-dose curves as input into the algorithm. Bremsstrahlung is insignificant and is accounted for by using measured depth-dose data and assuming a uniform photon dose component. The effect of backscatter caused by electron–electron scattering is ignored although investigations to quantify this effect are

currently under way. Geometrical effects of air gap and skin contours are inherently predicted by the algorithm.

Most radiotherapeutic electron beams can be conceptually described as a narrow beam emerging from an accelerator, converted to a broad beam by either a scanning magnet or scattering foils, and incident on a set of collimation devices, the final collimator being perhaps irregular in shape. The beam at this point may be considered as a collection of pencil beams passing through the collimator aperture. A pencil beam consists of those particles passing through an infinitesimal area $\delta X \delta Y$ as graphically

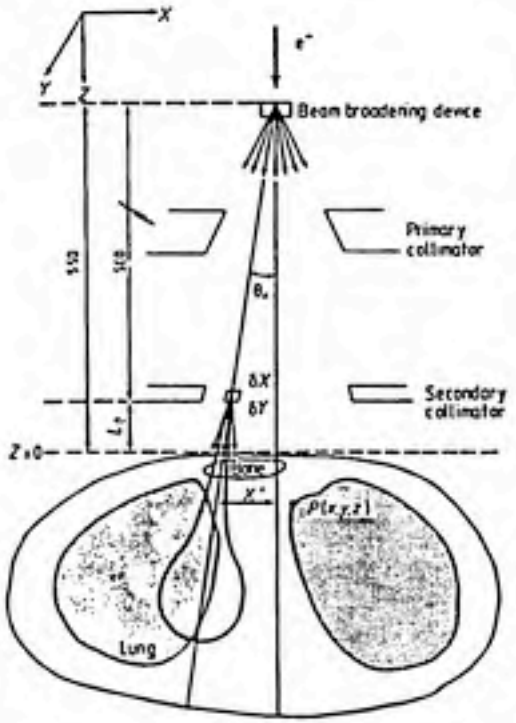

Figure 1. Schematic representation in the X-Z plane of a therapeutic electron beam incident on a patient.

represented in figure 1. Each pencil beam is considered to be composed of monoenergetic electrons having an average angular divergence θ_x, θ_y and RMS spread in angles σ_{θ_x}, σ_{θ_y}. The dose distribution resulting from each pencil beam can then be summed to give the dose distribution in the material lying beneath the collimator by

$$D(X, Y, Z) = \iint_{\text{collimator at } Z} S(X', Y') d(X' - X, Y' - Y, Z)\, dX'\, dY' \quad (1)$$

where $S(X', Y')$ is the relative strength of the pencil beam at X', Y' and $d(X' - X, Y' - Y, Z)$ is the dose contribution at X, Y, Z from the pencil beam at X', Y'. For calculation purposes, we evaluate equation (1) assuming the incident beam to be a collection of parallel pencil beams incident normally to the collimation plane. Consequently, we must integrate over the collimator limits as projected to position Z and make an inverse-square correction.

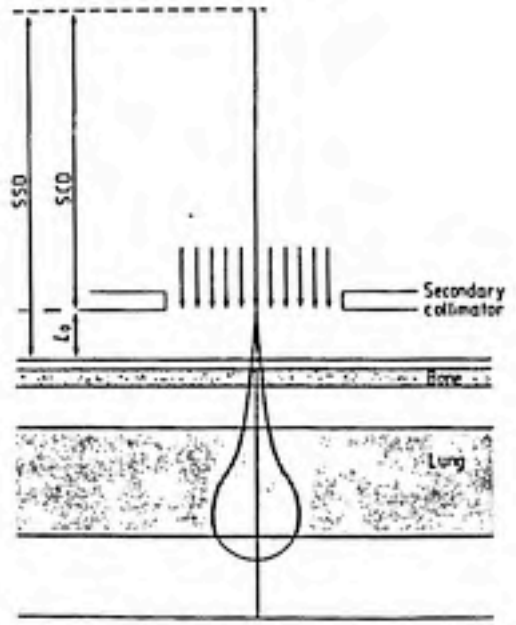

Figure 2. Schematic representation in the X-Z plane of a model electron beam incident on a stack of infinite slabs of varying material. The configuration corresponds to those inhomogeneities underlying the central ray of the pencil beam drawn in figure 1.

2.2. Slab inhomogeneities

Consider a stack of inhomogeneous slabs, each slab being homogeneous, but of a different material, as pictured in figure 2. The dose distribution due to a pencil beam incident normally on that configuration is separated into a central-axis term $g(Z)$ and an off-axis term $f(X, Y, Z)$,

$$d(X, Y, Z) = f(X, Y, Z)g(Z). \tag{2}$$

The off-axis term is assumed equal to the lateral flux distribution due to thick-target multiple Coulomb scattering (MCS) as formulated by the Fermi–Eyges theory (Eyges 1948) and applied to electrons:

$$f(X, Y, Z) = \frac{1}{2\pi\sigma_{\mathrm{MCS}}^2} \exp - \frac{X^2 + Y^2}{2\sigma_{\mathrm{MCS}}^2} \tag{3}$$

where σ_{MCS} is the RMS of the lateral distribution and is given by

$$\sigma_{\mathrm{MCS}}^2 = \frac{1}{2}\int_{-L_0}^{Z} (Z - Z')^2 \frac{\mathrm{d}\sigma_{\mathrm{MCS}}^2}{\mathrm{d}Z'}\,\mathrm{d}Z' \tag{4}$$

where $\mathrm{d}\sigma_{\mathrm{MCS}}^2/\mathrm{d}Z'$ is the linear angular scattering power evaluated at electron energy T corresponding to the mean energy of the electron beam at Z'. The linear angular scattering power is the product of mass density and the mass angular scattering power (see ICRU 21 (1972)). The mean energy at Z' is calculated by using Harder's linear relationship (Harder 1965)

$$T(Z') = T_0(1 - Z_{\mathrm{eff}}(Z')/R_{\mathrm{p}}) \tag{5}$$

where R_p is the practical range in water of the electron beam, T_0 is the incident electron energy, and Z_{eff} is the effective depth. The effective depth is calculated assuming that the linear stopping power, dE/dZ, of the material at Z relative to that of water is relatively independent of electron energy for normal body tissues;

$$Z_{eff}(Z) = \int_{-L_0}^{Z} \frac{(dE/dZ')}{(dE/dZ')_{H_2O}} dZ'. \tag{6}$$

Because the electron beam has traversed vacuum windows, scatter foils, beam monitors, air, etc. prior to reaching the secondary collimator, each pencil beam has an angular spread at any point in space that again is Gaussian according to the Fermi–Eyges theory (Eyges 1948) with an RMS projected scattering angle

$$\sigma_{\theta_x}^2 = \sigma_{\theta_y}^2 = A_0 - A^2/A_2 \tag{7}$$

where A_i is the ith moment of linear angular scattering power given by

$$A_i = \frac{1}{2}\int_0^{SCD} (SCD - Z')^i \frac{d\sigma_{MCS}^2}{dZ'} dZ'. \tag{8}$$

This RMS angular spread is projected into a lateral spread at Z equal to $(Z + L_0)\sigma_{\theta_x}$. The convolution of that Gaussian with that due to MCS after the collimator in equation (3) gives

$$f(X, Y, Z) = \frac{1}{2\pi\sigma^2} \exp - \frac{X^2 + Y^2}{2\sigma^2} \tag{9}$$

where

$$\sigma^2 = \sigma_{MCS}^2 + (Z + L_0)^2\sigma_{\theta_x}^2. \tag{10}$$

We assume that the depth-dose term of equation (2) is related to the same depth-dose term in water, g_0, by

$$g(Z) = g_0(Z_{eff})[(SSD + Z_{eff})/(SSD + Z)]^2 \tag{11}$$

where we have corrected for the effective depth and inverse square. By assuming a uniform incident beam ($S = 1$), g_0 can be extracted from a measured depth-dose curve in a water phantom, D_0, by substituting equations (9) and (11) into equation (1)

$$D_0(X, Y, Z) = \left(\frac{1}{2\pi\sigma_0^2}\iint_{\text{collimator at } Z} \exp - \frac{(X - X')^2 + (Y - Y')^2}{2\sigma_0^2} dx'\, dy'\right) g_0(Z). \tag{12}$$

For rectangular fields of dimension WX by WY at the SSD, equations (1), (9), and (11) can be solved assuming a uniform incident beam ($S = 1$):

$$D(X, Y, Z) = \frac{1}{4}\left(\text{erf}\,\frac{WXZ/2 - X}{\sqrt{2}\sigma} + \text{erf}\,\frac{WXZ/2 + X}{\sqrt{2}\sigma}\right) \times \left(\text{erf}\,\frac{WYZ/2 - Y}{\sqrt{2}\sigma} + \text{erf}\,\frac{WYZ/2 + Y}{\sqrt{2}\sigma}\right) g_0(Z_{eff})\left(\frac{SSD + Z_{eff}}{SSD + Z}\right)^2 \tag{13}$$

where WXZ, WYZ are the projected collimator sizes at Z given by $WXZ = WX(1 + Z/SSD)$ and $WYZ = WY(1 + Z/SSD)$. If we now use a measured central-axis depth-dose curve $D_0(0, 0, Z)$ for a square field size $WX\phi$, in order to determine g_0 in

equation (12), we obtain

$$D(X, Y, Z) = \frac{1}{4}\left(\operatorname{erf}\frac{WXZ/2 - X}{\sqrt{2}\sigma} + \operatorname{erf}\frac{WXZ/2 + X}{\sqrt{2}\sigma}\right) \times \left(\operatorname{erf}\frac{WYZ/2 - Y}{\sqrt{2}\sigma} + \operatorname{erf}\frac{WYZ/2 + Y}{\sqrt{2}\sigma}\right) \times D_0(0, 0, Z_{\text{eff}})\left(\operatorname{erf}\frac{WX\phi Z/2}{\sqrt{2}\sigma_0}\right)^{-2}\left(\frac{\text{SSD} + Z_{\text{eff}}}{\text{SSD} + Z}\right)^2. \quad (14)$$

This result is for rectangular fields, whereas irregular fields can be evaluated similarly from equations (1), (9), and (12) to give

$$D(X, Y, Z) = \left(\frac{1}{2\pi\sigma^2}\iint_{\text{collimator at } Z} S(X', Y') \exp -\frac{(X - X')^2 + (Y - Y')^2}{2\sigma^2}\,dx'\,dy'\right) \times D_0(0, 0, Z_{\text{eff}})\left(\operatorname{erf}\frac{WX\phi Z/2}{\sqrt{2}\sigma_0}\right)^{-2}\left(\frac{\text{SSD} + Z_{\text{eff}}}{\text{SSD} + Z}\right)^2. \quad (15)$$

The dose distribution for rectangular fields, equation (14), has the same off-axis dependence as the age–diffusion algorithm formulated by Kawachi (1975) and extended by Steben *et al* (1979) and Millan *et al* (1979). The $\kappa\tau$ parameter is replaced by σ^2, which now has physical meaning and can be calculated for arbitrary slabs of inhomogeneous media. The latter term in equation (10) represents the contribution to the beam penumbra due to MCS prior to the collimation device and explains why an increasing air gap causes the penumbra width to increase.

The depth-dose dependence is extracted from a measured depth-dose distribution rather than a parametrisation as proposed by Steben *et al* (1979) because of the apparent difficulty in fitting distributions without using several parameters as shown by Millan *et al* (1979). In all cases, the field-size dependence of the depth-dose curve comes from the off-axis terms whose erfs contain the ratio of field width to beam sigma, which varies with depth. The equation defining equivalent square field size, $W_{\text{eq.sq}}$, for rectangular fields is

$$\operatorname{erf}\frac{WXZ/2}{\sqrt{2}\sigma}\operatorname{erf}\frac{WYZ/2}{\sqrt{2}\sigma} = \left(\operatorname{erf}\frac{W_{\text{eq.sq}}/2}{\sqrt{2}\sigma}\right)^2 \quad (16)$$

therefore, $W_{\text{eq.sq}}$ varies with depth; thus, the concept of equivalent squares for electrons is meaningless. However, we may extract the depth-dose for rectangular field sizes from square-field data by noting from equation (14) that

$$D^{WX,WY}_{(0,0,Z)} = (D^{WX,WX}_{(0,0,Z)} D^{WY,WY}_{(0,0,Z)})^{1/2}. \quad (17)$$

This same expression can also be shown to hold for output factors (Mills *et al* 1980) so that equation (17) should be true for depth-dose data normalised to individual maxima as well as to the maximum of a reference field size.

Because of bremsstrahlung in the beam, a small photon contribution must be considered. This is done by assuming that the dose beyond the depth of the practical range is entirely due to photons and that photon dose short of that depth increases only by the inverse-square correction. The off-axis dependence of the photon dose is taken to be constant within the collimator and zero outside. The net result is that the field size

dependence of the depth-dose curve built into equation (14) applies only to the electron dose component.

2.3. Patient calculations

In order to calculate the dose distribution in an inhomogeneous patient, we assumed that the dose contribution from the pencil beam at X', Y' to each point of calculation can be made considering the inhomogeneity structure along that ray to be infinite in lateral extent, i.e., we assume the geometry in figure 2 for calculating the contribution from the ray drawn in figure 1 to the dose at every point P. The equation (15) must be modified as σ becomes a function of lateral position (X, Y) as well as Z.

In the presence of large air gaps, the latter term of equation (10) for σ^2 dominates so that the effects of sharp discontinuities are underestimated as the severe local changes in σ^2_{MCS} will not be reflected in σ^2. This effect is minimised if one recalls that the Gaussian in equation (15) came from the convolution of the two Gaussians, with σ^2_{MCS} and $\sigma^2_{air} = (Z + L_0)^2 \sigma^2_{\theta_s}$ of equation (10) when σ_{MCS} was independent of X and Y. Therefore, before the convolution, equation (15) can be expressed as

$$D(X, Y, Z) = \iint_{\text{collimator at } Z} S(X', Y') \Bigg[\frac{1}{2\pi\sigma^2_{air}} \iint \exp - \frac{(X'-X'')^2 + (Y'-Y'')^2}{2\sigma^2_{air}} \times \frac{1}{2\pi\sigma^2_{MCS}} \exp - \frac{(X-X'')^2 + (Y-Y'')^2}{2\sigma^2_{MCS}} D_0(0, 0, Z_{eff}) \times \left(\operatorname{erf} \frac{WX\phi Z/2}{\sqrt{2}\sigma_0} \right)^{-2} \left(\frac{SSD + Z_{eff}}{SSD + Z} \right)^2 dx'' dy'' \Bigg] dx' dy'. \tag{18}$$

If we now switch the order of integration,

$$D(X, Y, Z) = \iint S_{air}(X'', Y'', Z) \frac{1}{2\pi\sigma^2_{MCS}} \exp - \frac{(X-X'')^2 + (Y-Y'')^2}{2\sigma^2_{MCS}} \times D_0(0, 0, Z_{eff}) \left(\operatorname{erf} \frac{WX\phi Z/2}{\sqrt{2}\sigma_0} \right)^{-2} \left(\frac{SSD + Z_{eff}}{SSD + Z} \right)^2 dx'' dy'' \tag{19a}$$

$$S_{air}(X'', Y'', Z) = \frac{1}{2\pi\sigma^2_{air}} \iint_{\text{collimator at } Z} S(X', Y') \exp - \frac{(X'-X'')^2 + (Y'-Y'')^2}{2\sigma^2_{air}} dx' dy'. \tag{19b}$$

Physically, S_{air} represents the flux at position Z in air in the absence of all matter below the collimator. We then propagate that flux to Z in the presence of inhomogeneous material. All terms involving Z_{eff} and σ_{MCS} are inside the integral, recalling that these quantities are defined with respect to the central axis of individual pencil beams. The limits on the integral of equation (19a) are infinite, but in reality the integration is carried out only 2–3 cm past the collimator's edge. For the case of infinite slabs these results reduce to equation (14).

The approximation of this algorithm, that the medium under the central ray of each pencil beam is infinite in extent, produces calculational errors greatest in the shadow of thick inhomogeneities whose edge is parallel to the beam. This is due to a lack of subsequent scattering of the particles scattered from the denser medium into the less dense medium, as well as the miscalculation of particle ranges as discussed by Goitein and Sisterson (1978). We believe that the algorithm is a compromise between speed

and accuracy in calculating dose in the penumbra as well as in the presence of inhomogeneities.

2.4. Incorporation of CT data

The algorithm was developed assuming that an accurate description of patient inhomogeneities is available. Such information is adequately supplied by CT data. In particular, the linear collision stopping power relative to that of water and the linear scattering power are required at each point in the patient. These quantities are assumed to be a function of CT number, H. The linear stopping power ratio of the medium to that of water is assumed to be independent of energy and related to the CT number. This relationship is independent of electron energy within approximately ±0.5% from 1–20 MeV for the tissues listed in table 1 and plotted in figure 3. The linear collision stopping powers are calculated according to ICRU 21 (1972) with the density correction calculated according to Kim (1973). The CT number H is defined to be $500\,\mu/\mu_0$, where μ is the linear attenuation coefficient of the medium and μ_0 is that of water. The μ values are calculated from the tables of NSRDS-NBS 29 (Hubbell 1969) at the average X-ray energy of the scanner.

Table 1. Electron properties and CT number of various tissues

Tissue	H(120 kV$_p$)†	H(140 kV$_p$)‡	$\frac{(dE/dZ)}{(dE/dZ)_{H_2O}}$§	$\frac{(d\sigma^2/dZ)}{(d\sigma^2/dZ)_{H_2O}}$§
ICRU 21 (1972)				
Fat	449	456	0.933	0.729
Muscle	528	527	1.051	1.040
Bone	936	839	1.422	1.863
ICRP 23 (1975), Constantinou (1978)				
Lung	147	148	0.311	0.292
Adipose	452	457	0.930	0.761
Red marrow	503	507	1.027	0.912
Brain	515	514	1.027	1.002
Kidney	522	522	1.043	1.025
Liver	532	531	1.059	1.045
Inner bone	599	576	1.098	1.135

† Evaluated at $\bar{E}_\gamma = 67$ keV.
‡ Evaluated at $\bar{E}_\gamma = 80$ keV.
§ Evaluated at $T_e = 10$ MeV.

The ratio of the linear scattering power of the medium to that of water is also assumed to be energy-independent and again related to the CT number. The relationship is electron-energy-independent within approximately ±0.5% from 1–20 MeV for the tissues listed in table 1 and plotted in figure 4. The linear scattering powers are calculated according to ICRU 21 (1972). The linear scattering power for a given CT number is then extracted by multiplying this ratio by $(d\sigma^2/dZ)|_{H_2O}$ at the energy of equation (5) corresponding to the effective depth.

CT data is normally available on a rectangular grid, where each volume element is a voxel. For clarity consider the problem in two dimensions, in which case a CT number corresponds to the mean attenuation coefficient within a pixel. The first step in the

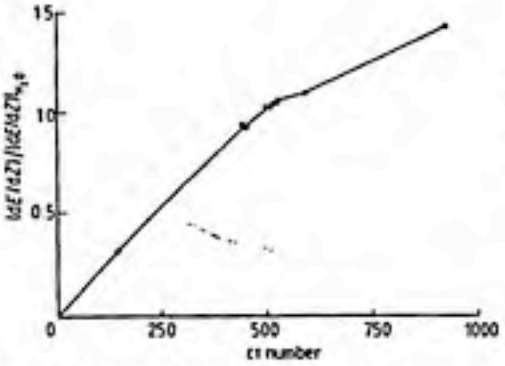

Figure 3. Plot of electron linear stopping power ratio against CT number of 120 kV_p X-rays for tissues of table 1. Full curve represents the function used by the algorithm.

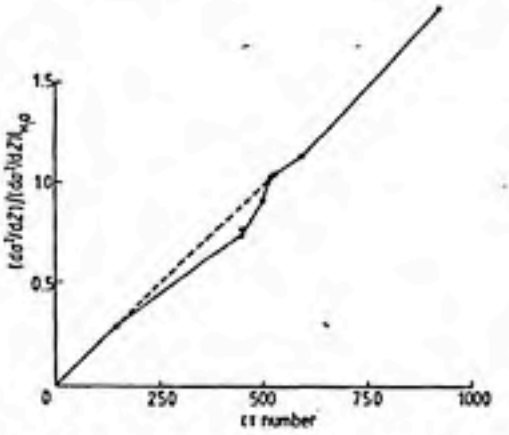

Figure 4. Plot of electron linear scattering power ratio against CT number of 120 kV_p X-rays for tissues of table 1. Full curve represents the function used by the algorithm; the broken curve could be used for lung.

algorithm is to construct a fan grid in which the fan lines intersect at the electron source, and the horizontal lines are perpendicular to the central-ray fan line. The CT number is then interpolated at the intersection of these grid lines from the original CT data matrix. This method has been previously described by Parker *et al* (1979).

A matrix of the efficient depths is then calculated along the points of the fan grid by applying equation (6) numerically for each fan line, i.e.

$$Z_{\text{eff}}^{i,j} = Z_{\text{eff}}(Z_i, X_j) = \sum_{k=1}^{i-1}\left(\frac{(dE/dZ)}{(dE/dZ)_{H_2O}}\right)_{k,j}\Delta Z + \frac{\Delta Z}{2}\left(\frac{(dE/dZ)}{(dE/dZ)_{H_2O}}\right)_{i,j} \tag{20}$$

where ΔZ is the interval between grid points along a fan line. A matrix of MCS sigmas is calculated along the points of the fan grid by applying equation (4) numerically for each fan line:

$$(\sigma^2_{\text{MCS}})_{i,j} = \sigma^2_{\text{MCS}}(Z_i, X_j) = \sum_{k=1}^{i-1}\left(\frac{d\sigma^2_{\text{MCS}}}{dZ}\right)_{k,j}\int_{Z_k}^{Z_k+\Delta Z}(Z_i - Z')^2\,dZ'$$

$$= \sum_{k=1}^{i-1}\left[\left(\frac{d\sigma^2_{\text{MCS}}}{dZ}\right)_{k,j}\Delta Z\right]\left((Z_k - Z_i)^2 + \Delta Z(Z_k - Z_i) + \frac{\Delta Z^2}{3}\right). \tag{21}$$

In order to increase the computational speed, a recursion relation is used to evaluate equations (20) and (21). That relationship for the MCS sigmas is

$$(\sigma^2_{\text{MCS}})_{i,j} = [(M_2^{i,j} + M_1^{i,j} + (M_0^{i,j}/3)]\Delta Z^2 \tag{22a}$$

$$M_2^{i,j} = M_2^{i-1,j} - 2M_1^{i-1,j} + M_0^{i-1,j} + \Delta Z(d\sigma^2_{\text{MCS}}/dZ)_{i-1,j} \tag{22b}$$

$$M_1^{i,j} = M_1^{i-1,j} - M_0^{i-1,j} - \Delta Z(d\sigma^2_{\text{MCS}}/dZ)_{i-1,j} \tag{22c}$$

$$M_0^{i,j} = M_0^{i-1,j} + \Delta Z(d\sigma^2_{\text{MCS}}/dZ)_{i-1,j}. \tag{22d}$$

The linear scattering powers are calculated from the curve of figure 4 and the linear scattering power of water evaluated at the mean electron energy corresponding to $Z_{\text{eff}}^{i,j}$.

3. Results

The algorithm has been evaluated by comparing measurements with the various predictions. In all cases the comparison was reduced to a two-dimensional problem by making the phantom independent of the third dimension (X or Y). The third dimension was incorporated only when the field size dependence of depth-dose was compared. Calculations were made on a Control Data Corporation CYBER 171-24. Dose was calculated on a 0.25 cm grid and CT data were stored on a fan grid of 0.25 cm in depth and 0.25 cm laterally at the proximal edge of the CT fan matrix. For those calculations involving numerical integration, the step size is that of the CT grid spacing.

Measurements were made on an AECL Therac 20 linear accelerator with the 17 MeV electron beam. Ion chamber dosimetry was done with a 0.1 cm^3 air-gas cylindrical ionisation chamber manufactured by PTW. The chamber was operated at 300 V with the beam operated at an average dose rate of approximately 1 Gy min^{-1}. The readings were not corrected for polarity or saturation effects which were less than 1%. For that data expressed as dose, the conversion from ionisation to dose was made according to the methods described by Almond (1976).

Film dosimetry was done by using Kodak Type M film that was hand developed. Film was used only for the measurement of distributions perpendicular to the incident beam, in which case the film was normal to the beam. The exposures were nominally 15 cGy maximum to ensure that film response was linear (Almond 1976).

For large air gaps between the collimator and patient, the scattering upstream of the collimator either dominates or contributes significantly to the penumbra via the latter term in equation (10). σ_{θ_x} is best determined by in-air measurements of the penumbra using film. Films were exposed for a 10 cm × 10 cm field size at varying distances below the collimator. The results are plotted in figure 5 as the 90%–10% distance in the penumbra against distance below the collimator. The angular sigmas are then equal to 0.391 times the slope of the line fitting the data. These results show: (i) that the angular sigma is independent of the transverse axis; (ii) that the theory adequately describes the penumbra in-air; and (iii) that the angular sigma can be adequately predicted using equation (7) giving 24 mrad for the setup. In the evaluation of equations (7) and (8), the

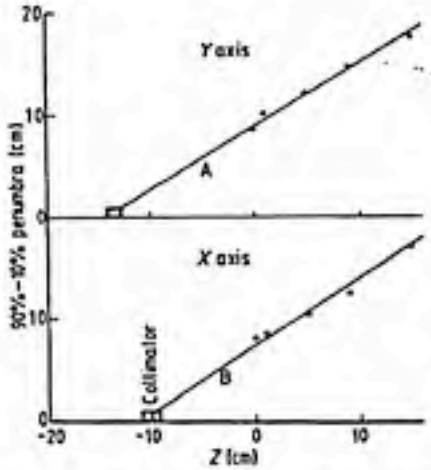

Figure 5. In-air penumbra measurements against distance from collimator. Line A, $\sigma_{\theta_x} = 24$ mrad, line B, $\sigma_{\theta_x} = 26$ mrad.

scanning magnet of the Therac 20 was assumed to be equivalent to an infinitely thin scattering foil with a very large scattering power and negligible energy loss located at the source position. Preferably, σ_{air} should be selected to fit the measured penumbra rather than derived from equation (7).

The dose distribution in a water phantom calculated by equation (14) for a 10 cm × 10 cm field size at 100 cm SSD is compared to measured data in figure 6. The

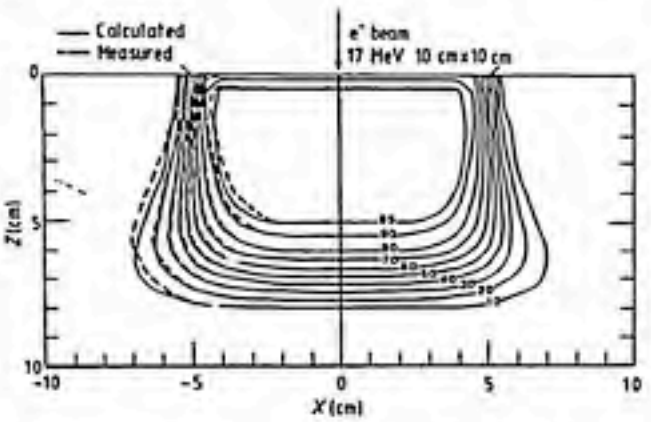

Figure 6. Comparison of calculated with measured isodose lines for 10 cm × 10 cm field size at 100 cm SSD from 17 MeV electrons on the Therac 20.

measured depth-dose curve was used as input; therefore, this comparison tests the off-axis calculation only. Agreement was within approximately ±1 mm except near the 10% and 95% isodose lines, where agreement was within ±3 mm. The overestimate of dose above 80% is most likely due to the fact that we have assumed the beam incident on the collimator $S(X'Y')$ to be uniform. In reality the primary collimators cause the beam incident on the secondary collimators to be non-uniform at the edges. This non-uniformity is due to in-air scattering (Brahme 1977) and is why the primary collimators are opened 5 cm outside the secondary collimator. The effect may be corrected by incorporating $S(X', Y')$, which should be approximately equal to the off-axis dependence term in equation (14) with σ calculated from equation (10), where σ_{MCS} is calculated from equation (4) for the air between the primary and secondary collimators and σ_{air} is calculated from equation (7) for the material above the primary collimator. The wider beam penumbra at the 10% isodose line is possibly due to the neglect of electron–electron scattering at the shallow depths and the non-explicit dependence of bremsstrahlung at the deeper depths. These results are consistent with those reported by Perry and Holt (1980).

The depth-dose for any field size can be predicted from a single measured field by equation (14) as previously discussed. 6 cm × 6 cm and 8 cm × 8 cm depth-dose distribution are predicted from a 10 cm × 10 cm distribution in figure 7. The calculation exhibits the same trend in the data; however, there is significant disagreement for the smaller field size, which is believed to be due to the neglect of electron–electron scattering. Therefore, we recommend that data either be measured or interpolated from measured data for determining the depth-dose of the field size being calculated. For rectangular fields, the depth-dose can be calculated from the appropriate square

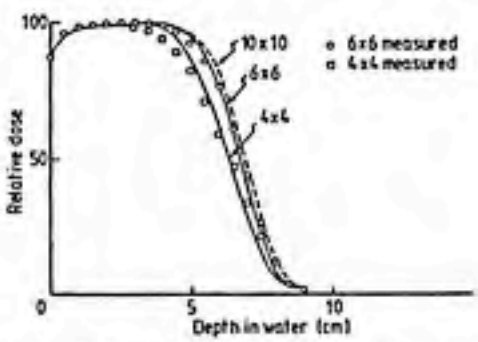

Figure 7. Comparison of measured depth-dose distributions with those calculated from 10 cm × 10 cm field size for Therac 20 17 MeV electrons using equation (14).

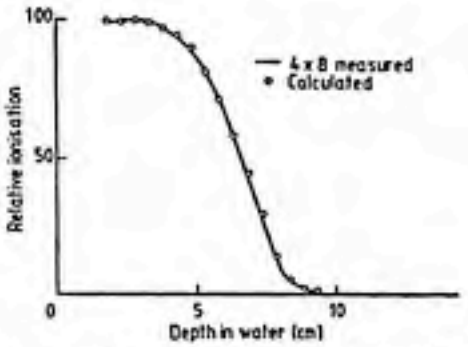

Figure 8. Comparison of measured depth-dose of a 4 cm × 8 cm field size with that calculated from 4 cm × 4 cm and 8 cm × 8 cm depth-dose data using equation (17).

fields as predicted by equation (17). Figure 8 demonstrates that the measured depth-dose distribution of a 4 cm × 8 cm field can be sufficiently calculated from those of 4 cm × 4 cm and 8 cm × 8 cm fields by using this method.

The beam edges in inhomogeneous phantoms have been studied. This effect would be most significant in low-density lung tissue. A 3.1 cm polystyrene–10.2 cm cork–5.0 cm polystyrene phantom was used to simulate the thorax, and beam profiles were measured using film at depths of 0, 2.6, 5.2 and 7.8 cm below the polystyrene–cork interface. The results are compared with calculations in figure 9. The agreement is consistent with the water phantom comparison, in that the measured profiles lie up to 3 mm outside the calculated profiles at the 10% level at the shallow effective depths.

The effect of side scatter is expected to be significant for inhomogeneities near the skin surface, in particular for hard bone. As a stringent test of the algorithm, the

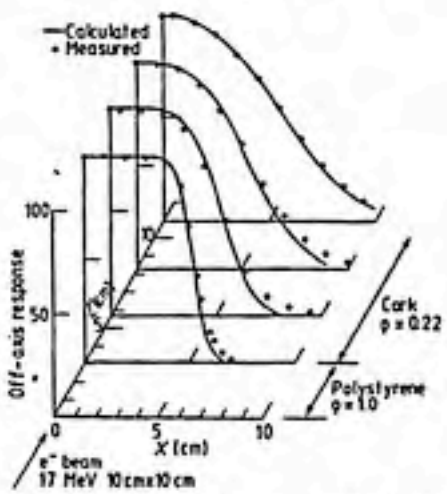

Figure 9. Comparison of measured with calculated beam profiles in a polystyrene/cork/polystyrene slab phantom for a 10 cm × 10 cm field size for Therac 20 17 MeV electrons.

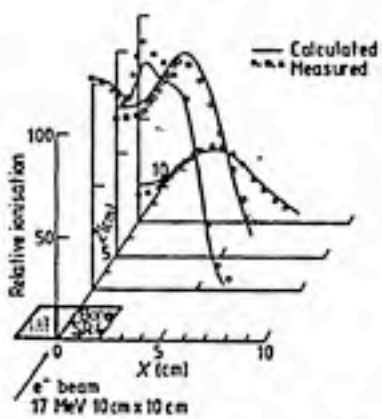

Figure 10. Comparison of measured with calculated ionisation profiles at various depths in a water phantom behind a 4 cm wide by 2 cm thick bone substitute block in a 10 cm × 10 cm field size for Therac 20 17 MeV electrons. The data have been normalised to calculation at central axis of the first profile.

ionisation profiles beneath a 2 cm deep × 4 cm wide cross-section of a bone substitute were measured. In figure 10 they are compared with the distributions calculated by the present theory. The effect of MCS was significant, generating hot and cold spots proximal to the inhomogeneity, while smoothing the dose profiles distally. The limitations of the theory as previously discussed are observable in the present case in that the hot and cold areas are underestimated by approximately 10%. However, bone in general will not be that thick nor have that sharp an edge, so that we might normally expect accuracy of this magnitude or better in our calculations.

A typical patient calculation using the present algorithm is shown in figure 11. It shows the treatment plan for a carcinoma in the maxillary antrum and demonstrates the influence of the antrum and nasal cavities on the distribution. In particular, consideration of the inhomogeneities provides the therapist with a more accurate dose distribution by correcting for range changes and scatter effects.

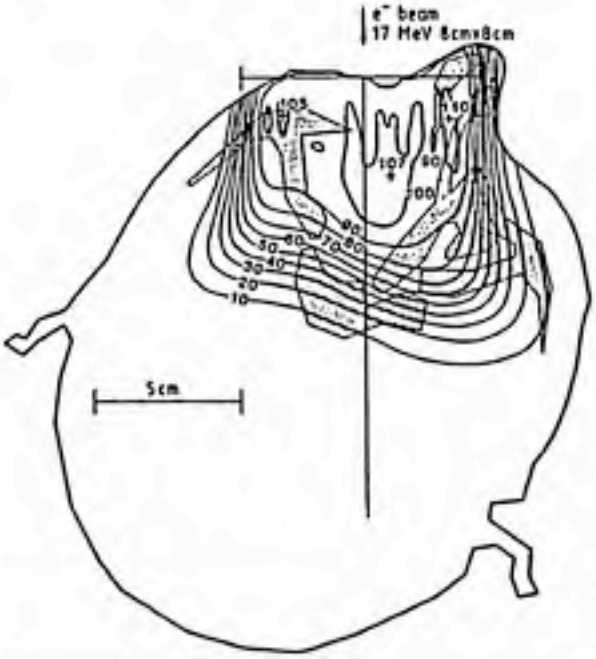

Figure 11. A single-portal patient dose distribution with gross inhomogeneities in the maxillary antrum for an 8 cm × 8 cm field using Therac 20 17 MeV electrons.

4. Summary

An algorithm has been developed for the calculation of electron beam dose distributions in the presence of inhomogeneous tissue. Dose distributions were calculated that accounted for range changes and side scatter, the latter being accommodated by the Fermi–Eyges theory of MCS (Eyges 1948). The use of measured depth-dose distributions and 'in-air' penumbra as input into the calculation have been discussed. The algorithm made certain approximations to the actual physics in order to increase computational speed, making routine patient calculations feasible. The comparison of calculations with phantom measurements in a Therac 20 17 MeV beam fairly show the accuracy that can be expected using the algorithm. Although not precise, the algorithm

marks a significant improvement in the dose distributions that can be provided to the radiotherapist for consideration in treatment planning. We expect that such information will give the radiotherapist more confidence in the distribution and better enable him to treat with electrons lesions of irregular shape or in the presence of inhomogeneities. In particular, underdosage, overdosage, and the need for tissue compensation can be quantitatively assessed using these results. The benefit to patients for such information is at present under evaluation.

The calculation requires an accurate description of patient anatomy within the treatment field. Since CT scanning seems to be the preferred method of providing such information, the correlations of linear stopping power and linear scattering power to CT number are required, and examples of these functions have been given. Processing of the effective depth and MCS sigma at each point within the treatment field is required, and recursion relations allowing efficient calculation of the latter have been presented.

Simplification of the general formulation for that of a water phantom shows the analogy of this method with that of the age–diffusion algorithm. In particular, results show the inability of these methods to predict the field size dependence of depth-dose distributions. An alternative formula for extracting rectangular-field depth-dose from square-field depth-dose is suggested. Finally, the dependence of the penumbra on air gap is explicit in the formulation, which should allow measurements of that effect to be quantified.

We believe that the theory we present provides a simple basis for electron beam dose calculations that is based on the physics of MCS. It provides a quantitative basis for explaining the influence of various parameters such as air gap, inhomogeneities, field size and SSD, on the calculation of dose. Application of the formulation to a variety of electron machines and energies can potentially provide a systematic way of characterising electron beams.

Acknowledgments

We are indebted to John Ames and Bill Simon for providing beam maintenance of the Therac 20 during the course of these measurements. Jim Ewton has provided invaluable assistance in the modification of the data acquisition system for electron beam dosimetry on the Therac 20. We thank Jack Cundiff for his support in the film and ion chamber dosimetry. This work was supported in part by Research Grant CA-06294 from the National Cancer Institute.

Résumé

Calcul de dose pour un faisceau d'électrons.

Nous avons calculé la distribution de dose d'un faisceau d'électrons dans un tissue inhomogène à partir d'un algorithme effectuant la somme des distributions de dose pour chaque faisceau étroit pris individuellement. La dépendance de la distribution de dose en fonction de l'excentration est décrite par la théorie de la cible épaisse de Fermi-Eyges pour des diffusions Coulombiennes multiples. Les résultats des mesures de la dose en profondeur dans des champs carrés sont utilisés pour les calculs. Nous tenons compte des corrections 'air' et nous utilisons les résultats des mesures 'dans l'air' dans la pénombre du faisceau. La profondeur effective, utilisée pour évaluer la dose en profondeur, et le sigma de la dispersion Gaussienne excentrée, sont calculées par des relations de récurrence à partir des données tomodensitometriques pour les materiaux sous-jacents à chaque faisceau fin pris individuellement. On montre la relation entre les données tomodensitométriques et le pouvoir d'arrêt linéaire relatif et le pouvoir diffusant linéaire relatif pour différents tissus. Les résultats des calculs sont verifiés en les comparant aux mesures effectuées dans un faisceau d'électrons de 17 MeV provenant d'un accelérateur linéaire Therac 20. Les courbes d'isodose calculées, prises individuellement, ne

différent pas de plus 2 mm des courbes mesurées dans un fantôme d'eau. Il en est de même dans des tranches de liège simulant des poumons. Les calculs au niveau d'un fantôme d'os simulé montrent des faiblesses dans le calcul. Enfin, on présente les résultats, chez un malade, pour le maxillaire. La théorie fait suggérer une méthode alternative pour le calcule de la dose en profondeur pour des champs rectangulaires.

Zusammenfassung

Dosisberechnungen für Elektronenstrahlen.

Die Berechnung der Elektronenstrahldosisverteilungen im homogenen Gewebe erfolgt mit Hilfe eines Algorithmus, der die Dosisverteilung von einzelnen Strahlen summiert. Die nicht-axiale Abhängigkeit der Dosisverteilung wird beschrieben durch die Fermi-Eyges-Theorie der Vielfach-Coulombstreuung an dicken Targets. Als Eingabe für die Berechnungen dienen die gemessenen Tiefendosiswerte quadratischer Felder. Zur Korrektur von Entladungseffekten werden Daten von Messungen 'in Luft' im Halbschatten des Strahls benutzt. Die effektive Tiefe, die man zur Auswertung der Tiefendosis braucht, und das Sigma der nicht-axialen Gauss-Verbreiterung gegen die Tiefe werden berechnet durch Rekursionsformeln von einer CT-Matrix für Material, das einzelnen Strahlen ausgesetzt ist. Die Korrelation der CT-Zahl mit dem relativen linearen Bremsvermögen und Streuvermögen für verschiedene Gewebe wird gezeigt. Die Ergebnisse der Berechnungen werden durch Vergleich mit Messungen an einem 17 MeV-Elektronenstrahl eines Therac-20-Linearbeschleunigers bestätigt. Berechnete Isodosen stimmen bis auf 2 mm mit Messungen in einem Wasserphantom überein. Eine ähnliche Übereinstimmung wird beobachtet bei Korkplatten zur Simulation der Lunge. Berechnungen bein einem Knochenersatz zeigen Schwächen des Modells. Die Theorie schlägt eine alternative Methode zur Berechnung der Tiefendosis rechtwinkliger Felder vor.

References

Almond P R 1976 in *High Energy Photons and Electrons* ed. S Kramer (New York: John Wiley) pp 131–68
Brahme A 1977 paper presented at *14th Int. Congr. of Radiology (Rio de Janeiro, Brazil)*
Constantinou C 1978 *PhD Thesis* University of London
Eyges L 1948 *Phys. Rev.* 74 1534–5
Goitein M 1978 *Med. Phys.* 5 258–64
Goitein M, Chen G T Y, Ting J Y, Schneider R J and Sisterson J M 1978 *Med. Phys.* 5 265–73
Goitein M and Sisterson J M 1978 *Radiat. Res.* 74 217–30
Harder D 1965 in *Symp. on High Energy Electrons (Montreaux)* ed. A Zuppinger and G Poretti (Berlin: Springer) p 260
Hogstrom K R, Rosen I I, Gelland E, Paciotti M A, Amols H I and Luckstead S 1980 *Med. Phys.* 7 703–9
Hubbell J H 1969 *Photon Cross Sections, Attenuation Coefficients, and Energy Absorption Coefficients From 10 keV to 100 GeV* NSRDS-NBS 29 (Washington, DC: US Government Printing Office)
ICRP 1975 *Report of the Task Group on Reference Man* ICRP Publication 23 (Oxford: Pergamon)
ICRU 1972 *Radiation Dosimetry: Electrons with Initial Energies Between 1 and 50 Mev* Report 21 (ICRU Publications, PO Box 20014, Washington, DC 30165, USA)
Kawachi I 1975 *Phys. Med. Biol.* 20 571–7
Kim Y S 1973 *Radiat. Res.* 56 21–7
Lillicrap S C, Wilson P and Boag J W 1975 *Phys. Med. Biol.* 20 30–8
Millan P E, Millan S, Hernandez A and Andreo P 1979 *Phys. Med. Biol.* 24 825–7
Mills M D, Hogstrom K R and Almond P R 1980 *Med. Phys.* 7 429
Nusslin F 1979 *Medicamundi* 24 112–8
Parker R P, Hobday P A and Cassell K J 1979 *Phys. Med. Biol.* 24 802–9
Perry D J and Holt J G 1980 *Med. Phys.* 7 207–15
Steben J, Ayyangar K and Suntharalingam N 1979 *Phys. Med. Biol.* 24 299–309
Sternick E 1978 in *Practical Aspects of Electron Beam Treatment Planning* Medical Physics Monograph No. 2, ed. C G Orton and F Bagne (New York: American Institute of Physics) pp 52–69
Williams E J 1940 *Phys. Rev.* 58 292–306
Zatz L M, von Essen C F and Kaplan H S 1961 *Radiology* 77 928–38

REFERENCE

1. Attix, F.H., "A Simple Derivation of N_{gas}, a Correction in A_{wall}, and Other Comments on the AAPM Task Group 21 Protocol", Medical Physics, Vol. 11, pp. 725-728, (1984).

2. Biggs, A.J., Boyer, A.L., Doppke, K.A., "Electron Dosimetry of Irregular Fields on the Clinac 18", International Journal of Radiation Oncology and Biological Physics, Vol. 5, pp. 433-440, (1979).

3. Hogstrom, K.R., Mills, M.D., Almond, P.R., "Electron Beam Dose Calculations", Physics in Medicine and Biology, Vol. 22, pp. 445-449, (1981).

4. ICRU Report No. 24, "Determination Of Absorbed Dose in a Patient Irradiated by Beams of X or Gamma Rays in Radiotherapy Procedures", (International Commission on Radiation Units and Measurements, Washington, D.C., 1976)

5. McParland, B.J., "Methods of Calculating the Output Factors of Rectangular Electron Fields", Medical Dosimetry, Vol. 14, pp. 17-21, (1989).

6. McParland, B.J., "A Method of Calculating the Output Factors of Arbitrary Shaped Electron Fields", Medical Physics, Vol. 16, pp. 88-93, (1989)

7. Mills, M.D., Hogstrom, K.R., Fields, R.S., "Determination of Electron Beam Output Factors for a 20-MeV Linear Accelerator", Medical Physics, Vol. 12, pp. 473-476, (1985)

8. Mills, M.D., Hogstrom, K.R., Almond, P.R., "Prediction of Electron Beam Output Factors", Medical Physics, Vol. 9, pp. 60-68, (1982).

9. Niriimand-Rad, A., "Film Dosimetry of Small Elongated Electron Beams for Treatment Planning", Medical Physics, Vol. 16, pp. 655-662, (1989)

10. Purdy, J.A., Goer, D.A., "Dual Energy X-Ray Beam Accelerators in Radiation Therapy: An Overview," Nuclear Instruments and Methods in Physics Research, Vol. 10, pp. 1090-1095, (1985).

11. Task Group 21, Radiation Therapy Committee, AAPM, "A Protocol for the Determination of Absorbed Dose from High Energy Photon and Electron Beams," Medical Physics, Vol. 10, pp. 741-771, (1983).

12. Varian Associates, Clinac 1800 Operating Procedures Manual, p. 4.29, (1984).